APPLIED COMPUTATIONAL ELECTROMAGNETICS SOCIETY JOURNAL

Special Issue on Antennas and Metasurfaces for Next-Generation Wireless System and Their Testing Techniques

Guest Editors:

Xiaoming Chen, Xi'an Jiaotong University, China
Jianxing Li, Xi'an Jiaotong University
Yingsong Li, Anhui University

October 2024
Vol. 39 No. 10
ISSN 1054-4887

The ACES Journal is abstracted in INSPEC, in Engineering Index, DTIC, Science Citation Index Expanded, the Research Alert, and to Current Contents/Engineering, Computing & Technology.

The illustrations on the front cover have been obtained from the ARC research group at the Department of Electrical Engineering, Colorado School of Mines

Published, sold and distributed by: River Publishers, Alsbjergvej 10, 9260 Gistrup, Denmark

OCTOBER 2024 REVIEWERS

Xiaoming Chen
Mohammad M. Fakharian
Jianxing Li
Yingsong Li
Rajini A. R.
Abdulkadir Shallah
Thi Lan Tran
Emine Yesim Zoral

THE APPLIED COMPUTATIONAL ELECTROMAGNETICS SOCIETY JOURNAL

Vol. 39 No. 10 October 2024

TABLE OF CONTENTS

Introduction to the Special Issue

Antennas and Metasurfaces for Next-Generation Wireless System and Their Testing Techniques

Guest Editors:

Prof. Xiaoming Chen, Xi'an Jiaotong University, China, xiaoming.chen@mail.xjtu.edu.cn

Jianxing Li, Xi'an Jiaotong University, jianxingli.china@xjtu.edu.cn

Prof. Yingsong Li, Anhui University, liyingsong@ieee.org

Welcome to the special issue of Applied Computational Electromagnetics Society Journal (ACES) The papers included here are related to Antennas and Metasurfaces for Next-Generation Wireless System and Their Testing Techniques.

Fast Broadband Scattering Computation for Finite Periodic Arrays using the Characteristic Basis Function Method and the Best Uniform Rational Approximation

Fang Li[1], Hai Rong Zhang[2], Lin Chen[2], and Xing Wang[2]

[1]Antenna and RF Specialist Department
20th Research Institute of China Electronics Technology Group Corporation, Xi'an, Shaanxi 710068, China
kleelf@163.com

[2]Department of Electrical and Computer Engineering
Xi'an, Shaanxi 710071, China
m15592666916@163.com, linchen3@stu.xidian.edu.cn, wangxing@mail.xidian.edu.cn

***Abstract* –** In this paper, a hybrid method combining the characteristic basis function method (CBFM) and the best uniform rational approximation (BURA) technique for fast wideband radar cross-section (RCS) prediction of finite periodic arrays is proposed. The traditional CBFM requires reconstructing the reduced matrix at each frequency point, which is very time-consuming when calculating the wideband RCS of the target. By introducing the BURA technique, the hybrid method is proposed to efficiently calculate the wideband RCS. The target is first divided into several easily solvable subdomains. Then, the surface integral equation is solved by the characteristic function method to obtain the equivalent surface current at the Chebyshev node. Afterwards, the surface current in a desired frequency band is represented by the Chebyshev series. To improve accuracy, the Chebyshev series is matched with the Maehly approximation. After obtaining the current coefficients in the whole bandwidth, the current density at any frequency point in the bandwidth can be calculated. Finally, the broadband electromagnetic scattering characteristics of the finite periodic arrays can be obtained.

***Index Terms* –** best uniform rational approximation, broadband, characteristic basis function method, Maehly approximation.

I. INTRODUCTION

In recent years, typical periodic structures such as frequency-selective surfaces, electromagnetic bandgap structures and metamaterial structures have been widely analyzed and applied. These structures are often electrically large and have complex electromagnetic properties that vary with frequency and other parameters. The analysis of these structures may require further refinement of the mesh. Both of them will lead to a large amount of the number of unknowns.

To address the above problems, many methods have been proposed [1][2]. One is the traditional Method of Moments (MoM) [3], which is extremely expensive in terms of computational resources when dealing with electrically large problems. The multilayer fast multipole method (MLFMA) [4][5] and the adaptive cross approximation (ACA) algorithm [6][7] have both been proposed to address this problem. These algorithms can improve the computational efficiency of MoM, but they require the use of an iterative method for solving. Therefore, there is a problem of slow convergence or even failure to converge when dealing with complex objectives. A second class of methods is to reduce the impedance matrix dimension by constructing basis functions, such as the sub-entire domain basis functions [8] and the characteristic basis function method (CBFM) [9][10]. These methods reduce the impedance matrix scale and decrease the number of unknowns for the target. The method first divides the objective into several subdomains. Then different subdomain sizes can be selected to control the dimension of the impedance matrix according to the requirements. Finally, the weighting coefficients of the characteristic basis functions can be obtained by solving the impedance matrix in low dimensions by the direct method. The stability and computational efficiency of the solution are guaranteed.

However, when utilizing CBFM to obtain the target broadband RCS the impedance matrix must be filled repetitively at each frequency point, leading to a large amount of computational time. In recent years, fast computational methods such as the impedance matrix interpolation method, the Cauchy method, the best uniform rational approximation (BURA) [11][12], model parameter estimation (MBPE) [13][14] and asymptotic waveform estimation (AWE) [15–18] have been proposed.

Submitted On: January 16, 2024
Accepted On: July 11, 2024

https://doi.org/10.13052/2024.ACES.J.391001

Among them, BURA has been widely used. It has the advantages of good convergence, easy integration with CBFM and no need to increase memory. When using BURA the process of repeated solutions of matrix equations can be bypassed, which reduces the computation time of the impedance matrix.

The remainder of this paper is organized as follows. The formulations of the Chebyshev approximation technique (CAT) application to CBFM are explicitly derived in Section II. Three examples are presented in Section III to verify the accuracy and efficiency of the hybrid CBFM-CAT algorithm and the conclusion of this work is drawn in Section IV.

II. CBFM-CAT FORMULATION

In solving the broadband electromagnetic characteristics of periodic structures, CBFM is utilized to solve the large unknown matrix during computation. However, for broadband RCS calculations, CBFM still needs to calculate the surface currents at each frequency, which leads to a large amount of computation time. By introducing the idea of CAT, the hybrid CBFM-CAT implements to achieve fast frequency sweeping as follows.

The electric field integral equation (EFIE) can be written as:

$$Z(k)I(k) = V(k), \tag{1}$$

where $Z(k)$ denotes impedance matrix, $I(k)$ denotes current coefficient vector and $V(k)$ denotes excitation vector.

CBFM divides the target into N subdomains Ω_1, $\Omega_2, \ldots \Omega_N$. According to CBFM, the matrix equation of equation (1) can be written as:

$$\begin{bmatrix} Z_{11}(k) & \cdots & Z_{1N}(k) \\ \vdots & \ddots & \vdots \\ Z_{N1}(k) & \cdots & Z_{NN}(k) \end{bmatrix} \begin{bmatrix} I_1(k) \\ \vdots \\ I_N(k) \end{bmatrix} = \begin{bmatrix} V_1(k) \\ \vdots \\ V_N(k) \end{bmatrix}. \tag{2}$$

When $\mathrm{li} = lj$, $Z_{lilj}(k)$ is the self-impedance matrix of region Ω_{li}. When$\mathrm{li} \neq lj$, $Z_{lilj}(k)$ is the mutual impedance matrix of region Ω_{li} and region Ω_{lj}.$I_{lj}(k)$ is the matrix of current coefficients of region Ω_{lj}, $V_{lj}(k)$is the excitation vector of region Ω_{lj} and $li \in [1,2,...,N], lj \in [1,2,...,N]$.

Uniform plane wave illuminates each subdomainΩ_{li}, the frequency range$f \in [f_a, f_b]$, the corresponding wave number is $k \in [k_a, k_b]$. Using the coordinate transformation, $\widetilde{k}$ is obtained by:

$$\widetilde{k} = \frac{2k - (k_a + k_b)}{k_a - k_b} \left(\widetilde{k} \in [-1,1]\right). \tag{3}$$

Let $T_q\left(\widetilde{k}\right)(q = 1,2,...n)$ be a Chebyshev polynomial of order q defined as follows:

$$T_1\left(\widetilde{k}\right) = 1, T_2\left(\widetilde{k}\right) = \widetilde{k};$$
$$T_{q+1}\left(\widetilde{k}\right) = 2kT_q\left(\widetilde{k}\right) - T_{q-1}\left(\widetilde{k}\right). \tag{4}$$

Then the q-th Chebyshev node of the Q order Chebyshev polynomial can be calculated by equation (5):

$$\widetilde{k_q} = \cos\left[\frac{(2q-1)}{2Q}\pi\right] \quad (q = 1,2,...,n). \tag{5}$$

To transform $\widetilde{k_q}$ from interval $[-1,1]$ into interval $[f_a, f_b]$, the q-*th* Chebyshev frequency sampling point in band f can be obtained by using equation (6):

$$k_q = {}^1\!/_2\left[(k_a + k_b) - \widetilde{k_q}(k_a - k_b)\right]. \tag{6}$$

Afterwards, the induced current $I_{li}(k_q)$ at the Chebyshev frequency sampling point k_q in the li-th subdomainΩ_{li} is obtained. Assume that the number of discrete units in the subdomain before expansion is N_{li} and after expansion is N_{li}^e. Then the main characteristic basis functions of the extended subdomain li can be derived from:

$$Z_{lili}^e(k_q) J_{li}^p(k_q) = V_{li}^e(k_q), \tag{7}$$

where $V_{li}^e(k_q)$ is a $N_{li}^e \times 1$ matrix, the matrix corresponding to the extended subdomain in the excitation vector from equation (2). $Z_{lili}^e(k_q)$ is the self-impedance matrix of the extended subdomain, which is an N_{li}^e-dimensional square matrix. By performing the LU decomposition of $Z_{lili}^e(k_q)$ followed by matrix inversion, the main characteristic basis functions of the extended subdomain $J_{li}^p(k_q)$ can be derived from equation (7).

According to the Foldy-Lax multipath scattering equation, the total characteristic basis function for constructing a periodic structure target should include the primary characteristic basis function (PCBF), which represents the self-interaction of the subdomains themselves. The secondary characteristic basis function (SCBF) represents the interaction between the subdomains. The primary secondary feature basis function $J_{li}^{S1}(k_q)$ can be used as an excitation source by superimposing the primary feature basis function $J_{li}^p(k_q)$ on the remaining subfields. The surface induced current is generated in the desired subregion. The primary characteristic basis function has been derived from equation (7), at which point the secondary characteristic basis function can be derived from:

$$Z_{lili}^e(k_q)\mathrm{J}_{li}^{S1}(k_q) = -\sum_{lj=1, lj\neq li}^{N} Z_{lilj}(k_q)\mathrm{J}_{lj}^{P}(k_q). \tag{8}$$

$J_{li}^{S1}(k_q)$ can be obtained by a direct inverse of the LU decomposition of $Z_{lili}^e(k_q)$ via equation (8). Similarly, the secondary characteristic basis functions of the remaining subdomain targets can be derived. If the secondary characteristic basis functions are taken only up to $J_{li}^{S1}(k_q)$, the total induced current on each subdomain target can be written as:

$$J_{li}(k_q) = a_{li}J_{li}^P(k_q) + b_{li}J_{li}^{S1}(k_q). \tag{9}$$

The dimensionality of the impedance matrix can be reduced by Galerkin method. By obtaining the unknown

coefficients a_{li} and b_{li}, the induced currents on a total of N subdomains can be obtained. Then the target surface current coefficients for each subdomain are $J_{li}(k_q) = I_{li}(k_q), (li = 1,2,...,N)$.

To improve the accuracy of the numerical solution, the Chebyshev series is replaced by a rational function named Maehly approximation. The surface current $I_n(k_s)$ in the li-th subdomainΩ_{li} can be approximated as:

$$I_{li}(k_s) \cong \sum_{q=1}^{n} c_{li,q} T_q\left(\widetilde{k}_q\right) - \frac{c_{li,1}}{2}, \tag{10}$$

where $c_{li,q} = \frac{2}{n}\sum_{q=1}^{n} I_{li,q}(k_q) T_q\left(\widetilde{k}_q\right)$.

To improve the accuracy of the numerical solution, using the Maehly approximation to obtain the current coefficient vector, $I_{li}(k_s)$ can be re-expressed as:

$$\begin{aligned} I_{li}(k_s) &\approx R_{LM,li}\left(\widetilde{k}_q\right) = \frac{P_{L,li}\left(\widetilde{k}_q\right)}{Q_{M,li}\left(\widetilde{k}_q\right)}, \\ &= \frac{a_{li,0}T_0\left(\widetilde{k}_q\right) + a_{li,1}T_1\left(\widetilde{k}_q\right) + \cdots + a_{li,L}T_L\left(\widetilde{k}_q\right)}{b_{li,0}T_0\left(\widetilde{k}_q\right) + b_{li,1}T_1\left(\widetilde{k}_q\right) + \cdots + b_{li,M}T_M\left(\widetilde{k}_q\right)}, \end{aligned} \tag{11}$$

where $a_{li,l}$ denotes the first unknown coefficient of the li-th subdomain at the Chebyshev node of the Chebyshev polynomial of order L, and $b_{li,m}$ denotes the second unknown coefficient of the li-th subdomain at the Chebyshev node of the Chebyshev polynomial of order$M$, $b_{li,0} = 1$.

Substituting equation (12) into equation (11) and using the constant equation $T_p(x)T_q(x) = {}^1\!/_2\left(T_{p+q}(x) + T_{|p-q|}(x)\right)$, the unknown coefficients $a_{li,i}\,(i = 0,1,\cdots,L)$ and $b_{li,j}\,(j = 0,1,\cdots,M)$ can be obtained as follows:

$$\begin{cases} a_{li,0} = \frac{1}{2}b_{li,0}c_{li,0} + \frac{1}{2}\sum\limits_{j=1}^{M} b_{li,j}c_{li,j} \\ a_{li,i} = c_{li,i} + \frac{1}{4}b_{li,i}c_{li,0} + \frac{1}{2}\sum\limits_{j=1}^{M} b_{l,j}\left(c_{li,i+j} + c_{li,|j-i|}\right) \\ i = 1,2,\cdots,L \end{cases} \tag{12}$$

$$\begin{bmatrix} c_{li,L+2}+c_{li,L} & c_{li,L+3}+c_{li,L-1} & \cdots \\ c_{li,L+3}+c_{li,L+1} & c_{li,L+4}+c_{li,L} & \cdots \\ \vdots & \vdots & \cdots \\ c_{li,L+M+1}+c_{li,L+M-1} & c_{li,L+M+2}+c_{li,L+M-1} & \cdots \end{bmatrix} \begin{bmatrix} c_{li,L+M+1}+c_{li,L-M+1} \\ c_{li,L+M+1}+c_{li,L-M+2} \\ \vdots \\ c_{li,L+2M}+c_{li,L} \end{bmatrix} \bullet \begin{bmatrix} b_{li,1} \\ b_{li,2} \\ \vdots \\ b_{li,M} \end{bmatrix} = -2\begin{bmatrix} c_{li,L+1} \\ c_{li,L+2} \\ \vdots \\ c_{li,L+M} \end{bmatrix} \tag{13}$$

Calculating the unknown coefficients $a_{li,i}$ and $b_{li,j}$ for the n-th subdomain Ω_n, the surface current $I_{li}(k_s)$ can be obtained by using $a_{li,i}$ and $b_{li,j}$ and substituting them into equation (11) thereby obtaining the radar scattering cross section of the periodic structure target at each frequency.

The error function E_n is defined as:

$$\begin{aligned} E_{n,li} &= R_{LM,li}\left(\widetilde{k}_q\right) - I_{li}(k_s) \\ &= \frac{1}{Q_{M,li}\left(\widetilde{k}_q\right)}\sum_{p=L+M+1}^{\infty} h_{p,li}T_{p,li}\left(\widetilde{k}_q\right) \end{aligned}. \tag{14}$$

The coefficient $h_{p,li}$ in equation (14) can be defined as:

$$\begin{aligned} &P_{M,li}\left(\widetilde{k}_q\right) - Q_{L,li}\left(\widetilde{k}_q\right) I_{li}(k_s) \\ &= \sum_{p=L+M+1}^{\infty} h_{p,li}T_{p,li}\left(\widetilde{k}_q\right) \end{aligned}. \tag{15}$$

Since $b_{li,0}$ is usually set to 1, the coefficient $h_{p,li}$ decays rapidly then the error function $E_{n,li}$ can be approximated as:

$$\begin{aligned} &P_{M,li}\left(\widetilde{k}_q\right) - Q_{L,li}\left(\widetilde{k}_q\right) I_{li}(k_s) \\ &= \sum_{p=L+M+1}^{\infty} h_{p,li}T_{p,li}\left(\widetilde{k}_q\right) \end{aligned}, \tag{16}$$

where:

$$\begin{aligned} h_{L+M+1,li} &= c_{L+M+1,li} \\ &+ {}^1\!/_2\sum_{i=1}^{M} b_{i,li}\left(c_{L+M+i+1,li} + c_{L+M-i+1,li}\right) \end{aligned}. \tag{17}$$

Hence, $R_{LM,li}\left(\widetilde{k}_q\right)$ can be taken as BURA to $I_{li}(k_s)$.

III. NUMERICAL SIMULATION RESULTS AND ANALYSIS

A. A 9x9 patch array

The first example is a 9×9 patch array consisting of square ring frequency selective cells with a center frequency of 15 GHz, as illustrated in Fig. 1. The incident angle is (θinc, φinc)=(0°, 0°) and the scattering angle is (θsca, φsca)=(60°, 0°). The working frequency band is 12 to 20 GHz. The step frequency is 100 MHz. The whole structure can be decomposed into four subdomains with a total of 3402 unknowns for the target. The unknowns for each sub-domain are 756, 756, 756 and 1134 when using CBFM, respectively. The broadband RCS of the target was calculated by using the Chebyshev approximation with the Maehly approximation (L=M=3, L=M=7, L=M=15).

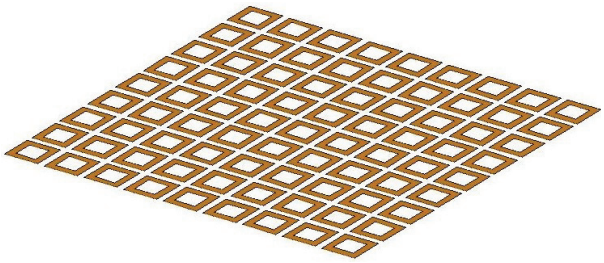

Fig. 1. Geometry of the patch array.

Figure 2 illustrates the broadband bistatic cross-section (BCS) of the patch array in the 12-20 GHz range using three different CBFM-CAT orders (L=3, 7, 15). A results comparison between the CBFM-CAT algorithm and the conventional moments method can be seen

in Fig. 2. Better results will be obtained as we increase the CAT order.

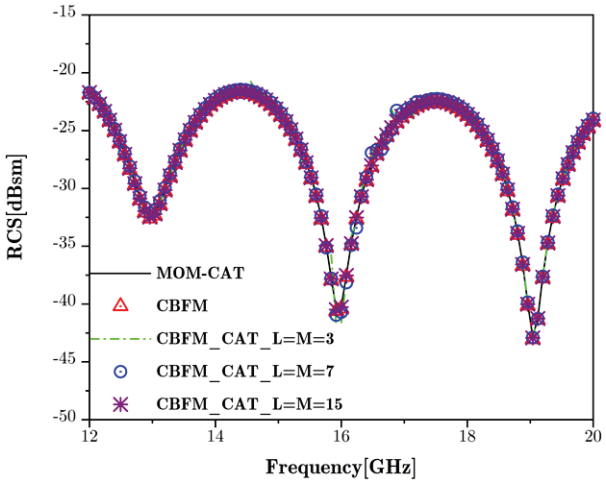

Fig. 2. Wideband BCS of the patch array computed by CBFM-CAT using three different orders.

As shown in Fig. 3, the peak memory, CPU time and the number of iterations of MoM, CBFM and CBFM-CAT with three orders are compared. According to Fig. 3, total CPU time of CBFM-CAT (L=M=15) can be reduced by 54.4% compared to conventional MoM.

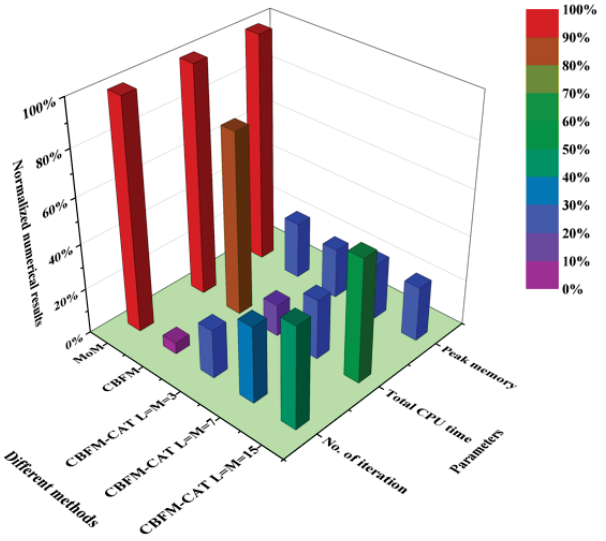

Fig. 3. Comparation of peak memory, CPU time and number of iterations for conical radome.

B. Square-ring FSS conical radome

The second example is a six-layer conical FSS radome consisting of a square-ring type frequency selector unit with a center frequency of 15 GHz, as illustrated in Fig. 4. The incident angle is (θ_{inc}, φ_{inc})=(0°, 0°) and the scattering angle is (θ_{sca}, φ_{sca})=(60°, 0°). The working frequency band is 12 to 20 GHz. The step frequency is 100 MHz. The whole structure can be decomposed into three subdomains with a total of 3234 unknowns for the target. The unknowns for each subdomain are 1386, 1134 and 714 when using CBFM, respectively. The broadband RCS of the target was calculated using the Chebyshev approximation with the Maehly approximation (L=M=3, L=M=7, L=M=15).

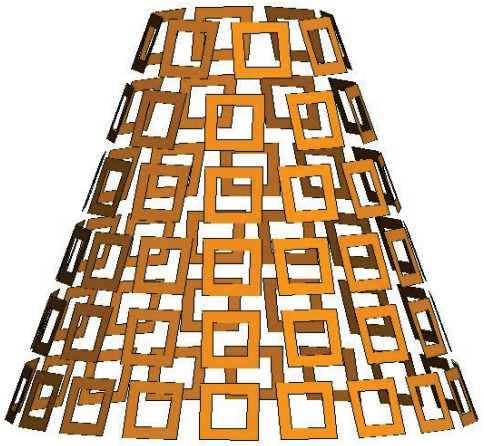

Fig. 4. Geometry of the square ring FSS conical radome.

Figure 5 illustrates the broadband BCS of the conical radome in the 12-20 GHz range using three different CBFM-CAT orders (L=3, 7, 15). Figure 5 shows that the results obtained by the CBFM-CAT algorithm are in good agreement with the traditional MoM. As we increase the order of CAT we get a better result.

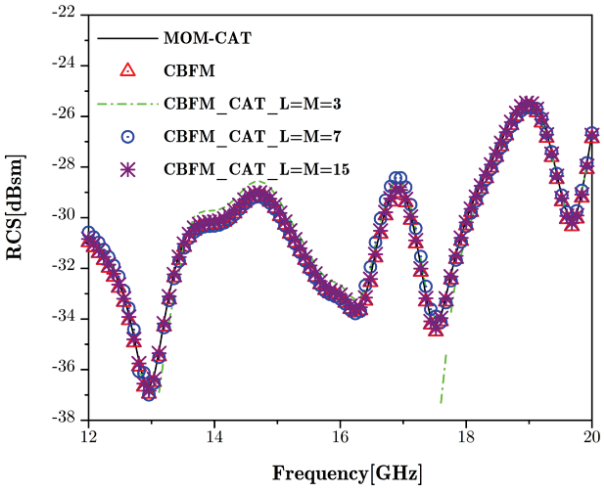

Fig. 5. Wideband BCS of conical radome computed by CBFM-CAT using three different orders.

As shown in Fig. 6, peak memory, CPU time and number of iterations of MoM, CBFM and CBFM-CAT with three orders are compared. According to Fig. 6, the computation time of CBFM-CAT (L=M=15) can be reduced by 54.7% compared to conventional MoM.

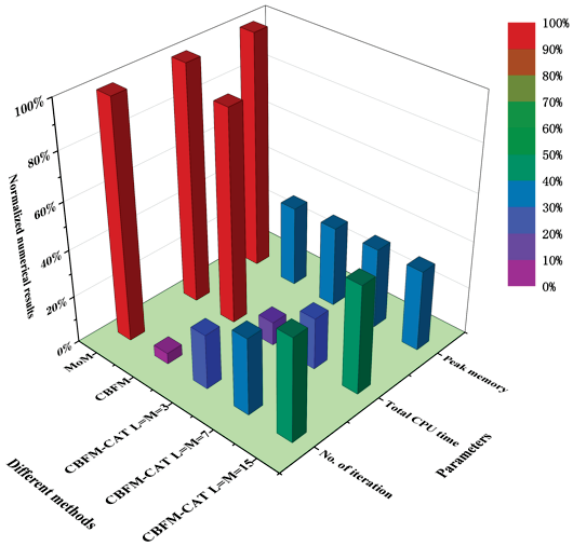

Fig. 6. Comparation of peak memory, CPU time and number of iterations for conical radome.

C. Square-ring FSS pyramid radome

The third example we consider is an FSS pyramid radome composed of a square-ring frequency selector unit with a center frequency of 15 GHz, as shown in Fig. 7. The model is divided into four subdomains. The FSS pyramid radome is discretized into 3136 elements so that the number of unknowns is 4704. The unknowns for each subdomain when using CBFM are 1176, 1176, 1176, 1176 and 1176. The incident angle is (θ_{inc}, φ_{inc})=(0°, 0°) and the scattering angle is (θ_{sca}, φ_{sca})=(60°, 0°). The working frequency band is 12 to 20 GHz. Step frequency is 100 MHz.

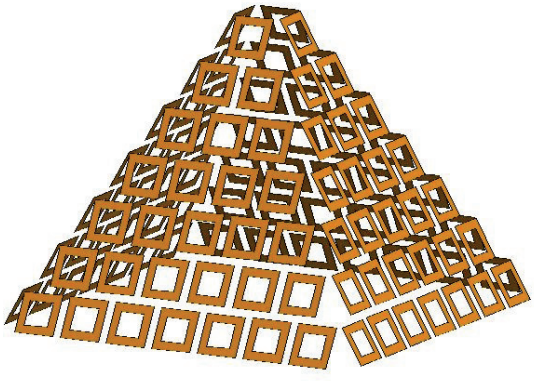

Fig. 7. Geometry of the square ring FSS pyramid radome.

The broadband RCS of the target was calculated using the Chebyshev approximation with the Maehly approximation (L=M=3, L=M=7, L=M=15). Figure 8 shows that the results obtained by the CBFM-CAT algorithm are in good agreement with traditional MoM. As the order of CAT increases, better results are obtained. The results obtained by CBF M-CAT are consistent with those obtained by MoM and CBFM.

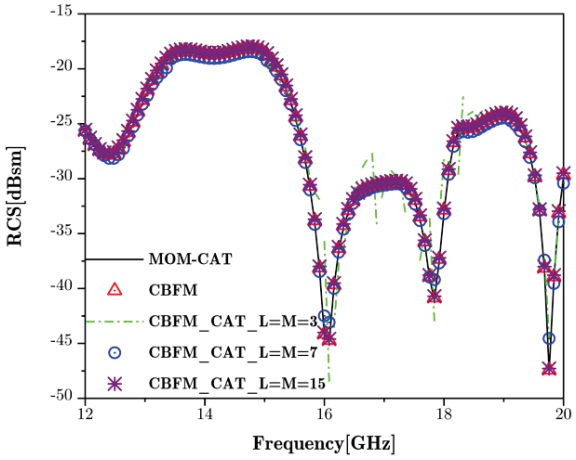

Fig. 8. Broadband BCS of the pyramid radome computed by CBFM-CAT using three different orders.

As shown in Fig. 9, peak memory, CPU time and number of iterations of MoM, CBFM and CBFM-CAT

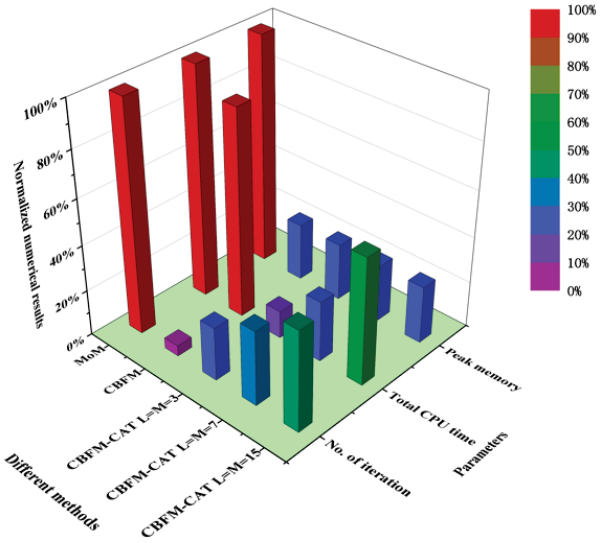

Fig. 9. Comparation of peak memory, CPU time and number of iterations for pyramid radome.

Table 1: Calculation result of three examples

Examples	MoM CPU Time (min)	CBFM (L=M=15) CPU Time (min)	MoM Memory (MB)	CBFM (L=M=15) Memory (MB)
Array patch	92.56	53.7	124.32	34.27
Conical radome	72.45	33.5	80.64	27.64
Pyramid radome	126.1	69.9	168.96	42.41

with three orders are compared. According to Fig. 9, the total CPU time of CBFM-CAT (L=M=15) can be reduced by 45.6% compared to conventional MoM.

Table 1 illustrates the total memory and CPU time required to compute the three examples by using MOM and CBFM methods. In comparison to traditional MoM, the memory requirement and CPU time of CBFM-CAT can achieve reduction for the three examples shown.

IV. CONCLUSION

In this paper, we propose a new hybrid CBFM-CAT algorithm to efficiently analyze the wideband electromagnetic bistatic scattering problem for finite periodic arrays. By applying CBFM, the dimensionality of the impedance matrix can be reduced. By introducing the idea of CAT, only the currents at the Chebyshev nodes are calculated. The surface current in a desired frequency band is represented by a Chebyshev series by combining it with the Maehly approximation. After obtaining the current coefficients over the entire broadband, we can then obtain the current density at any frequency point. Furthermore, we discuss the accuracy of the CBFM-CAT method at different orders. According to the numerical results, the proposed CBFM-CAT method is able to significantly improve efficiency with a slight loss of accuracy.

ACKNOWLEDGMENT

This work was supported in part by the National Natural Science Foundation of China (Grant 62471365, Grant 62271366, Grant 62394293, and Grant 62394290), the Fundamental Research Funds for the Central Universities (grant no. ZDRC210).

REFERENCES

[1] K. Niu, Z. J. Xiao, G. Xie, X. G. Ren, Y. S. Li, Z. X. Huang, X. L. Wu, and A. Z. Elsherbeni, "A stochastic FDTD algorithm for uncertainty quantification of electromagnetic-thermal simulation," *IEEE Trans. Microw. Theory Techn.*, vol. 72, no. 7, pp. 3935-3946, July 2024.

[2] G. Zhu, K. Niu, M. Q. Li, Y. S. Li, X. G. Ren, G. D. Xie, Z. X. Huang, X. L. Wu, and A. Z. Elsherbeni, "High-order ME-CFS-PML implementations for terminating the FDTD domain composed of arbitrary media," *IEEE Trans. Microw. Theory Techn.*, vol. 72, no. 4, pp. 2414-2426, Oct. 2023.

[3] R. F. Harrington and J. L. Harrington, *Field Computation by Moment Methods*. Oxford: Oxford University Press, 1996.

[4] J. Song, "Multilevel fast multipole algorithm for electromagnetic scattering by large complex objects," *IEEE Trans. Antennas Propag.*, vol. 45, no. 10, pp. 1488-1493, 2002.

[5] C. B. Wu, L. Guan, P. F. Gu, and R. S. Chen, "Application of parallel CM-MLFMA method to the analysis of array structures," *IEEE Trans. Antennas Propag.*, vol. 69, no. 9, pp. 6116–6121, Sep. 2021.

[6] K. Zhao, M. N. Vouvakis, and J.-F. Lee, "The adaptive cross approximation algorithm for accelerated method of moments computations of EMC problems," *IEEE Trans. Electromagn. Compat.*, vol. 47, no. 4, pp. 763-773, Nov. 2005.

[7] M. Bebendorf, "Approximation of boundary element matrices," *Numer. Math.*, vol. 86, no. 4, pp. 565-589, June 2000.

[8] X. Wang, D. H. Werner, and J. P. Turpin, "A fast analysis of scattering from large-scale finite periodic microstrip patch arrays arranged on a non-orthogonal lattice using sub-entire domain basis functions," *IEEE Trans. Antennas Propag.*, vol. 62, no. 5, pp. 2543-2552, 2014.

[9] E. Garc'1a, C. Delgado, and F. C'atedra, "Efficient iterative analysis technique of complex radome antennas based on the characteristic basis function method," *IEEE Trans. Antennas Propag.*, vol. 69, no. 9, pp. 5881-5891, Sep. 2021.

[10] C. Li, M. S. Sharawi, and R. Mittra, "Fast computation of electromagnetic scattering from dielectric objects using quadrilateral piecewise sinusoidal basis and characteristic basis function method," *IEEE Trans. Antennas Propag.*, vol. 70, no. 7, pp. 5683-5692, July 2022.

[11] J. Ling, S. X. Gong, X. Wang, B. Lu, and W. T. Wang, "A novel two-dimensional extrapolation

technique for fast and accurate radar cross section computation," *IEEE Antennas Wireless Propag. Lett.*, vol. 9, pp. 244-247, 2010.

[12] X. Wang, S. Zhang, H. Xue, S. X. Gong, and Z. L. Liu, "A Chebyshev approximation technique based on AIM-PO for wide-band analysis," *IEEE Antennas Wireless Propag. Lett.*, vol. 15, pp. 93-97, 2016.

[13] Z. Wang and S. V. Hum, "A broadband model-based parameter estimation method for analyzing multilayer periodic structures," *IEEE Trans. Antennas Propag.*, vol. 69, no. 9, pp. 5771-5780, Sep. 2021.

[14] X. Wang, D. H. Werner, and J. P. Turpin, "Application of AIM and MBPE techniques to accelerate modeling of 3-D doubly periodic structures with nonorthogonal lattices composed of bianisotropic media," *IEEE Trans. Antennas Propag.*, vol. 62, no. 8, pp. 4067-4080, Aug. 2014.

[15] C. J. Reddy, M. D. Deshpande, C. R. Cockrell, and F. B. Beck, "Fast RCS computation over a frequency band using method of moments in conjunction with asymptotic waveform evaluation technique," *IEEE Trans. Antennas Propag.*, vol. 46, no. 8, pp. 1229-1233, Aug. 1998.

[16] X. Wang, S. X. Gong, J. L. Guo, Y. Liu, and P. F. Zhang, "Fast and accurate wide-band analysis of antennas mounted on conducting platform using AIM and asymptotic waveform evaluation technique," *IEEE Trans. Antennas Propag.*, vol. 59, no. 12, pp. 4624-4633, Dec. 2011.

[17] Y. L. Jiang and J. M. Yang, "Asymptotic waveform evaluation with higher order poles," *IEEE Trans. Circuits Syst. I, Reg. Papers*, vol. 68, no. 4, pp. 1681-1692, Apr. 2021.

[18] M. A. M. Hassan and A. A. Kishk, "A combined asymptotic waveform evaluation and random auxiliary sources method for wide-band solutions of general-purpose EM problems," *IEEE Trans. Antennas Propag.*, vol. 67, no. 6, pp. 4010-4021, June 2019.

Fang Li was born in Shaanxi, China, in 1982. He received the M.Eng. Degree in electronic engineering from Xidian University, Xi'an, China, in 2008.

Currently, he is with the 20th Research Institute of China Electronics Technology Group Corporation, Xi'an 710065, China. His research interests include antenna RCS reduction, wideband antenna and metasurface.

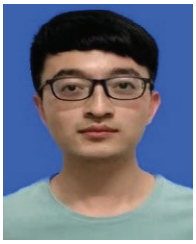

Hai Rong Zhang was born in Shaanxi, China, in 1996. He received the B.Eng. degree in electronic engineering from Xidian University, Xi'an, China, in 2019, where he is currently working toward the Ph.D. degree. His research interests include computational electromagnetic, hybrid methods and multiscale electromagnetic computing.

Lin Chen was born in Hunan, China, in 2000. He received the B.Eng. degree in electronic engineering from Xidian University, Xi'an, China, in 2022. His focus is computational electromagnetic.

Xing Wang received the Ph.D. degree from Xidian University, Xi'an, China, in 2011. His research interests include computational electromagnetic, fast algorithms for electromagnetic scattering and radiation, hybrid methods and EMC analysis.

Improved Mid-field Phased Array Calibration Method Based on Complex Interpolated Signals

Junhao Zheng[1], Zhengpeng Wang[2], Binhui Liu[3,4], Huaqiang Gao[1], and Xiaoming Chen[1]

[1]School of Information and Communications Engineering
Xi'an Jiaotong University, Xi'an 710049, China
1071218679@stu.xjtu.edu.cn, huaqiang.gao@xjtu.edu.cn, iaoming.chen@mail.xjtu.edu.cn

[2]Electronic Information Engineering
Beihang University, Beijing 100191, China
wangzp@buaa.edu.cn

[3]The 5th Electronic Research Institute
Ministry of Industry and Information Technology, Guangzhou 511370, China
liubinhui@ceprei.biz

[4]Key Laboratory of MIIT for Intelligent Products Testing and Reliability

Abstract – In this brief paper, an improved method of separate amplitude and phase interpolations is presented for the mid-field phased array calibration system. Since the amplitude is relatively continuous and the phase suffers from phase wrapping, the proposed method uses linear and phase-unwrapping natural neighbor interpolation methods to reconstruct the amplitude and phase matrices, respectively. When compared with the existing work, the proposed method is more accurate under the cost-effective over-the-air testing environment.

Index Terms – Complex signal, natural neighbor interpolation method, over-the-air test, phase wrapping, phased array calibration.

I. INTRODUCTION

Phased array systems can effectively control the excitation of array elements, meeting the requirements of specific communication systems for signal transmission and interference suppression [1]. However, the element branch will have characteristic variation causing the excitation signal loaded on the array element to deviate from expected values. Therefore, it is vital to calibrate the branches to improve the radiation performance of the phased array [2–4].

The array calibration is by default conducted with one element activated at a time (i.e. on-off mode). Since the coupling effect between array elements cannot be ignored, array calibration with all elements activated (i.e. all-on mode) would be adopted for good accuracy in this case [5, 6]. The all-on calibration methods can be classified as amplitude-only and complex measurements. In the amplitude-only measurement, the typical rotating element electric field vector (REV) method used phase variation to record the composite power of the array, and derived the relative amplitude and phase information from power changes [7]. The improved REV method in [8] characterized the array power response through a high-order Fourier series to identify the amplitude and phase errors of the elements, which was proved to have good practicability. However, the REV method for each element was time consuming, requiring a greater number of signal measurements than the complex calibration method.

For the complex calibration method, [9] used a transmission matrix to obtain the excitation coefficient under near-field measurement, which required good positioning accuracy and knowledge of the array configuration. However, [10] realized array calibration using a recursive matrix under far-field conditions, where the number of probe measurements is required to be equal to or greater than the number of elements in the array. Then, [11] enhanced testing efficiency by the matrix interpolation method and reduced the number of probe measurements. However, the phase interpolation was realized by the complex data interpolation, which could lead to phase wrapping between the adjacent points.

In this work, an improved interpolation and matrix reconstruction method is developed under the mid-field measurement (i.e., near-field w.r.t. the whole array yet far-field w.r.t. the array element). The number of probe moving positions under the all-on mode can be half the number of the array elements. Meanwhile, the branch matrix to be calibrated is obtained through the

Submitted On: December 14, 2023
Accepted On: January 9, 2024

https://doi.org/10.13052/2024.ACES.J.391002

transmission matrix. The amplitude and phase of the branches are interpolated by linear interpolation and phase-unwrapping natural neighbor interpolation methods, respectively. Note that the proposed solution in this work is essentially an improvement of the method presented in [11].

II. THEORY

This section firstly presents the on-off mode used as the standard benchmark. Then the proposed all-on mode method is introduced and compared with the method in [11].

A. On-off mode

A phased array calibration system is shown in Fig. 1. The probe moves to multiple positions to gather sufficient samples and the signal model can be expressed as follows:

$$\mathbf{S} = \mathbf{HT}, \tag{1}$$

where $\mathbf{S}$ is the S-parameter matrix measured by the probe using a vector network analyzer (VNA), $\mathbf{H}$ is the weighted excitation signal matrix, and $\mathbf{T}$ is the transmission matrix. If the numbers of weighted signals, probe positions and antenna elements are L, M and N, then $\mathbf{S}$, $\mathbf{H}$ and $\mathbf{T}$ are $L \times M$, $L \times N$ and $N \times M$ matrices, respectively. The transmission matrix $\mathbf{T}$ can be further expanded as:

$$\mathbf{T} = (\mathbf{CR}_{AUT}) \odot \mathbf{A} \odot \mathbf{R}_{pro}, \tag{2}$$

where $\mathbf{C}$ is a $N \times N$ RF branch response matrix, $\mathbf{R}_{AUT}$ is a $N \times M$ array element radiation pattern matrix indicating the pattern of the n-th array element for the m-th probe position, $\mathbf{A}$ is a $N \times M$ free-space transfer function matrix, $\mathbf{R}_{pro}$ is a $N \times M$ probe pattern matrix representing the pattern of the m-th probe position on the n-th array element and $\odot$ is the Hadamard product.

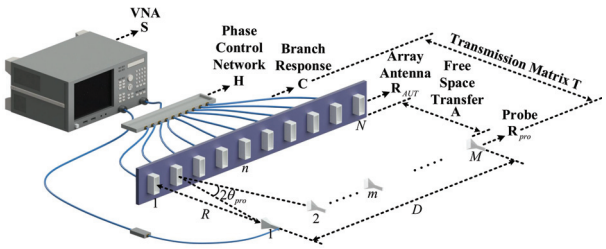

Fig. 1. Configuration of the phased array calibration.

Since the matrix $\mathbf{C}$ and $\mathbf{R}_{AUT}$ are combined to form the $N \times M$ signal branch matrix $\mathbf{P}$ to be calibrated, the matrix element of $(\mathbf{CR}_{AUT})_{nm}$ can be written as:

$$\mathbf{P}_{nm} = (\mathbf{CR}_{AUT})_{nm} = \sum_{i=1}^{N} \left(\alpha_{n,i} \cdot e^{j\phi_{n,i}}\right) r_{AUT,i,m}, \tag{3}$$

where n and m are the row and column of the element in $\mathbf{P}$, $\alpha_{n,i}$ and $\phi_{n,i}$ are the amplitude and phase of the RF branch response $\mathbf{C}$, and $r_{AUT,i,m}$ is the complex value of the array element in $\mathbf{R}_{AUT}$.

The calibration of the on-off mode applied to equations (1)-(3) can be seen as a standard benchmark to verify the effectiveness and accuracy of the proposed interpolation method under the all-on mode. The on-off mode is executed by enabling the n-th path and disabling the other $N-1$ signal branches. The probe vertically aligns to the face center of each array element forming a $N \times N$ S-parameter matrix $\mathbf{S}$. Therefore, the excitation matrix $\mathbf{H}$ turns to identity matrix $\mathbf{I}_N$, and the signal branch matrix to be calibrated can be derived as:

$$\mathbf{P}_{on-off} = \mathrm{S} \oslash \mathbf{A} \oslash \mathbf{R}_{pro}, \tag{4}$$

where $\oslash$ represents entry-wise division of two matrices. The diagonal elements of the reconstructed matrix $\mathbf{P}_{on-off}$ are the N signal branches to be calibrated for the N array elements (noted as a $1 \times N$ vector $A_{1,on-off}$), and the influence of the nonuniformity can be reduced by compensating the amplitude and phase deviation in $A_{1,on-off}$.

B. All-on mode

After getting the comparison result $A_{1,on-off}$ under the on-off mode, we then introduce the proposed method using the all-on mode and interpolation method to calibrate the phased array.

In order to reduce the time cost, the number of probe moving positions should be smaller than the number of array elements, which is $M < N$. The minimum probe number M should cover the aperture of the phased array.

The probe scanning configuration is shown in Fig. 1, where the maximum probe moving distance is D, the measurement range between the probe and array is R, and the M probe positions are evenly distributed in the range of D. Thus, the angle sampling interval can be calculated as:

$$\theta_{pro} = \tan^{-1}\left(\frac{D}{2R(M-1)}\right). \tag{5}$$

In order to better reconstruct and interpolate the small number of samples, an appropriate value of M is crucial. In this case, $2\theta_{pro}$ should be smaller than the half-power beamwidth (HPBW) θ_{3dB} of the array element. If θ_{3dB} is smaller than$2\theta_{pro}$, the power received by the probe drops significantly, which incurs great errors in the reconstruction of the signal branch matrix $\mathbf{P}$. Consequently, $\theta_{pro}\}\theta_{3dB}/16$ is selected as the angle sampling interval to guarantee that the amplitude of the receiving power is large enough to reduce the signal branch error, and the minimum number of probe positions M can be obtained as:

$$M \sim \left\lceil \frac{D}{2R\tan(\theta_{3dB}/16)} + 1 \right\rceil, \tag{6}$$

where $\lceil \bullet \rceil$ represents the rounding up operator. It is obvious that the probe position number M is proportional to

D, and inversely proportional to R and θ_{3dB}. Then we set $\mathbf{H}$ as a Hadamard matrix of order L, ignoring the first $L-N$ columns (which can be seen as virtual elements), and the $L \times N$ all-on mode excitation matrix $\mathbf{H}$ can be obtained [11]. After using the Moore-Penrose pseudoinverse matrix $\mathbf{H}^+$ of $\mathbf{H}$, the signal branch matrix $\mathbf{P}_{all-on}$ to be calibrated can be expressed as:

$$\mathbf{P}_{all-on} = \left(\mathbf{H}^{+}\mathbf{S}\right) \oslash \mathbf{A} \oslash \mathbf{R}_{pro}, \tag{7}$$

where $\mathbf{P}_{all-on}$ is a $N \times M$ matrix. Next, $\mathbf{P}_{all-on}$ should be interpolated to form a $N \times N$ matrix to calibrate the N signal branches.

The amplitude matrix $\mathbf{P}_{all-on,amp}$ of $\mathbf{P}_{all-on}$ can be interpolated by the linear interpolation method to get the $N \times N$ matrix $\mathbf{P}'_{all-on,amp}$, because the amplitude variation is relatively flat. However, since the phase matrix $\mathbf{P}_{all-on,pha}$ of $\mathbf{P}_{all-on}$ suffers from a $\pm 360°$ phase wrapping between adjacent points, the phase period should be added or subtracted to get the correct interpolation result, which can be understood as follows. If the phases of the two adjacent points are $190°$ and $-190°$, then the direct interpolation will yield $0°$, which is not correct. Thus, the latter phase $-190°$ should add $360°$ to be $170°$, and the interpolated phase can be correctly obtained as $180°$.

Then, the phase unwrapping $\mathbf{P}_{all-on,pha}$ is interpolated by the natural neighbor interpolation method, as shown in Fig. 2. The original data are marked as $x_1 - x_6$, the interpolated data is x_m. The Voronoi cell before and after interpolating x_m is calculated, where the cells of $x_1 - x_6$ before the interpolation have common areas $(S_1 - S_6)$ with the hexagon Voronoi cell of x_m, and the phase value of x_m is calculated as:

$$x_m = \frac{\sum_{n=1}^{N_0} x_n S_n}{\sum_{n=1}^{N_0} S_n}, \tag{8}$$

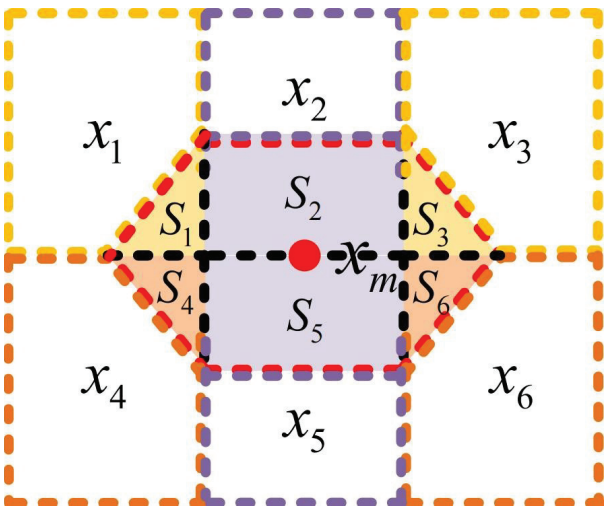

Fig. 2. Phase-unwrapping natural neighbor interpolation method.

Table 1: Performance comparison

Characteristics	Calibration Type	Dynamic Range	Mean Value
[11] Method	Amplitude/ Phase	0.92 dB14.6°	0.33 dB5.1°
Proposed Method	Amplitude/ Phase	0.85 dB10.3°	0.19 dB3.1°

where N_0 is the number of the adjacent cells of x_m. Then, the desired interpolated $N \times N$ phase matrix $\mathbf{P}'_{all-on,pha}$ is obtained.

Subsequently, the diagonal elements are extracted from $\mathbf{P}'_{all-on,amp}$ and $\mathbf{P}'_{all-on,pha}$ to form the N complex signal branches to be calibrated, noted as $1 \times N$ vector $A_{2,all-on}$. Moreover, in order to make comparison with the proposed method, the calibration method in [11] is used here, whose interpolation results are obtained as $A_{3,all-on}$. The basic mechanism of [11] also uses the interpolation method to reduce the initial sampling number, but the main difference between [11] and this work is that the reconstructed amplitude and phase matrix in [11] both used the linear interpolation method, which may lead to phase-wrapping errors for the interpolated complex results. Therefore, the proposed method can overcome the phase interpolation error and obtain more accurate signal branches. Finally, comparisons of $A_{1,on-off}$, $A_{2,all-on}$ and $A_{3,all-on}$ can reveal the effectiveness of the proposed calibration method.

III. MEASUREMENT AND ANALYSIS

The proposed method is verified in the environment of Fig. 3. A column (with $N = 14$ single vertical polarized waveguide antennas) of the planar array is selected as the AUT (antenna under test). The range D is 1.124 m, the testing frequency is 2.6 GHz, and the probe is a WR284 waveguide antenna whose H-plane HPBW is $127°$. The distance R is 1.0 m, which is the far-field range for the array element with dimension $D_{\text{dim}} = 8.03$ cm yet still in the near-field of the AUT array. The probe position M, calculated by equation (6), should be larger than 5, and $M = 7$ is chosen to probe the 14 array elements. The excitation matrix $\mathbf{H}$ is set to be a Hadamard matrix of order $L = 16$.

Then, the reconstructed 14×14 $\mathbf{P}'_{all-on,amp}$ and $\mathbf{P}'_{all-on,pha}$ are obtained by the proposed method, whose diagonal elements are extracted to form $A_{2,all-on}$. The 14×14 $\mathbf{P}_{on-off}$, used as a standard bench, is obtained by setting $\mathbf{H}$ as identity matrix $\mathbf{I}_N$ and M as 14 to form $A_{1,on-off}$. The calibrated results in [11] are acquired as a 1×14 vector $A_{3,all-on}$. The amplitudes and phases of $A_{1,on-off}$, $A_{2,all-on}$ and $A_{3,all-on}$ are plotted in Figs. 4 (a) and (b) in red, green and blue circles, respectively.

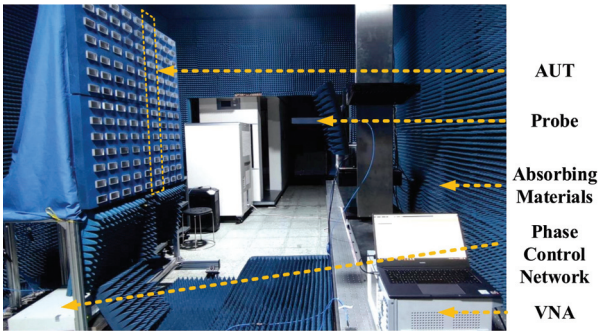

Fig. 3. Measurement environment.

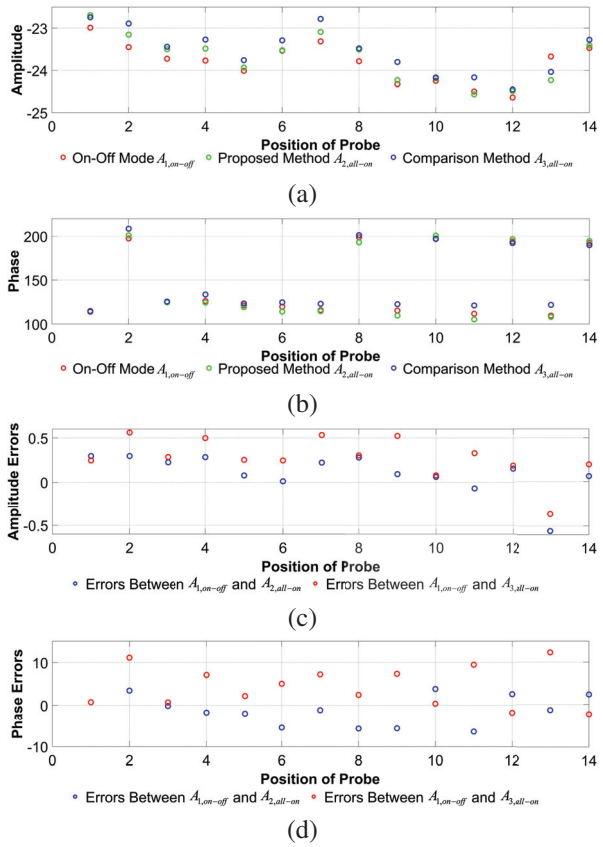

Fig. 4. Comparisons of (a) amplitude, (b) phase, (c) amplitude errors, and (d) phase errors for the extracted elementary signal branches of $A_{1,on-off}$, $A_{2,all-on}$ and $A_{3,all-on}$.

Finally, the amplitude/phase errors between $A_{1,on-off}$ and $A_{2,all-on}$, and those between $A_{1,on-off}$ and $A_{3,all-on}$, are shown in Figs. 4 (c) and (d), respectively. To better illustrate the performance comparison between the proposed method and the method of [11], the dynamic ranges and mean values of the amplitude/phase errors are listed in Table 1. It can be seen that the dynamic ranges and mean values for the errors of the proposed method is smaller than that of the method in [11]. The differences between the two methods of the amplitude/phase errors for the dynamic ranges and mean values are calculated as 0.07 dB/4.3° and 0.14 dB/2.0°, respectively, implying the superiority of the proposed method.

Thus, we can see from the results shown above that the element branches can be more accurately calibrated by the proposed interpolation method, and the separate interpolation method is more effective for complex signals with significant phase variation and phase wrapping influence.

IV. CONCLUSION

In this work, an improved interpolation method with a small number of probe positions (e.g. the half number of the array elements) is proposed for the phased array calibration. The proposed method used linear interpolation method and phase-unwrapping natural neighbor interpolation method to reconstruct the amplitude and phase matrices under the all-on mode, respectively. The proposed method has been proved to be more accurate than [11]. An error reduction of 0.07 dB/4.3° is achieved for the dynamic range, and a reduction of 0.14 dB/2.0° is achieved for the mean values.

ACKNOWLEDGMENT

This work was supported by Key Laboratory of MIIT for Intelligent Products Testing and Reliability 2023 Key Laboratory Open Project Fund (No. CEPREI2023-03) and CEPREI special fund (Grant 24Z10).

REFERENCES

[1] R. C. Hansen, *Phased Array Antennas*, 2nd ed. Hoboken, NJ: Wiley, 2009.

[2] R. L. Haupt, "Active electronically scanned array technology," in *Timed Arrays: Wideband and Time Varying Antenna Arrays*, Hoboken, NJ: Wiley, 2015.

[3] T. A. Milligan, "Phased arrays," in *Modern Antenna Design*, 2nd ed. Hoboken, NJ: Wiley, 2005.

[4] R. Mailloux, *Phased Array Antenna Handbook*, 3rd ed. Norwood, MA: Artech House, 2017.

[5] X. Chen, S. Zhang, and Q. Li, "A review of mutual coupling in MIMO systems," *IEEE Access*, vol. 6, pp. 24706-24719, 2018.

[6] H. Gao, W. Wang, Y. Wu, Y. Liu, G. F. Pedersen, and W. Fan, "Experimental comparison of on-off and all-on calibration modes for beam-steering performance of mm-wave phased array antenna-in-package," *IEEE Trans. Instrum. Means.*, vol. 70, pp. 1-9, 2021.

[7] S. Mano and T. Katagi, "A method for measuring amplitude and phase of each radiating element of a phased array antenna," *Electron. Commun. Jpn.*, vol. 65-B, no. 5, pp. 58-64, Jan. 1982.
[8] T. Takahashi, Y. Konishi, and I. Chiba, "A novel amplitude-only measurement method to determine element fields in phased arrays," *IEEE Trans. Antennas Propag.*, vol. 60, no. 7, pp. 3222-3230, July 2012.
[9] O. M. Bucci, M. D. Migliore, G. Panariello, and P. Sgambato, "Accurate diagnosis of conformal arrays from near-field data using the matrix method," *IEEE Trans. Antennas Propag.*, vol. 53, no. 3, pp. 1114-1120, Mar. 2005.
[10] R. Long, J. Ouyang, F. Yang, W. Han, and L. Zhou, "Multi-element phased array calibration method by solving linear equations," *IEEE Trans. Antennas Propag.*, vol. 65, no. 6, pp. 2931-2939, June 2017.
[11] Y. Zhang, Z. Wang, F. Zhang, X. Chen, J. Miao, and W. Fan, "Phased array calibration based on measured complex signals in a compact multiprobe setup," *IEEE Antennas Wireless Propag. Lett.*, vol. 21, no. 4, pp. 833-837, Apr. 2022.

Junhao Zheng received the B.Sc. degree in electronic information science and technology from Shandong University, Weihai, China, in 2017, the M.Sc. degree in signal and information processing from Northwestern Polytechnical University, Xi'an, China, in 2020, and the Ph.D. degree in electronic science and technology from Xi'an Jiaotong University, Xi'an, China, in 2024. His current research interests include antenna measurement in an anechoic chamber and reverberation chamber and over-the-air (OTA) testing.

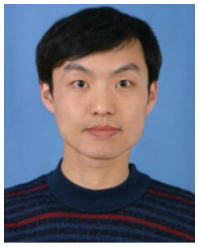

Zhengpeng Wang (Member, IEEE) was born in Shandong, China, in 1981. He received the B.Sc. degree in electronic science and technology from Shandong University, Jinan, China, in 2004, and the M.Sc. and Ph.D. degrees in electromagnetic field and microwave technology from Beihang University, Beijing, China, in 2007 and 2012, respectively. He was a Visiting Researcher with the Antenna and Applied Electromagnetic Laboratory, University of Birmingham, Birmingham, UK, from 2009 to 2010. From 2013 to 2015, he was a Research Fellow with the University of Kent, Canterbury, UK, and the University of Science and Technology Beijing, Beijing, China. He is currently an Associate Professor with Beihang University. His current research interests include over-the-air (OTA) tests, reconfigurable antennas, compact antenna test range feed antennas, and antenna measurement.

Binhui Liu received Ph.D. degree in Materials Physics and Chemistry from Sun Yat-Sen University, Guangzhou, China, in 2016. He worked as the technical director wireless communication laboratory in the Fifth Electronic Research Institute, Ministry of Industry and Information Technology, from 2016 till now. His research areas include wireless communication test technology for electronic products and vehicle communication network test technology.

Huaqiang Gao (Member, IEEE) received the B.E. degree in electronic and information engineering from Harbin University of Science and Technology, Harbin, China, in 2016, the B.A. degree in business English from Heilongjiang University, Harbin, in 2016, and the Ph.D. degree in electronic science and technology from Beijing University of Posts and Telecommunications (BUPT), Beijing, China, in 2022. Since 2019, he has been a Visiting Ph.D. Student and a Post-Doctoral Fellow with the Antennas, Propagation and Millimeter-Wave Systems Section, Aalborg University, Aalborg, Denmark. He is currently an Assistant Professor with the School of Information and Communications Engineering, Xi'an Jiaotong University, Xi'an, China. His research interests include over-the-air testing (OTA) of wireless devices, antenna measurement, and phased array calibration.

Xiaoming Chen (Senior Member, IEEE) received the B.Sc. degree in electrical engineering from Northwestern Polytechnical University, Xi'an, China, in 2006, and the M.Sc. and Ph.D. degrees in electrical engineering from the Chalmers University of Technology, Gothenburg, Sweden, in 2007 and 2012, respectively. From 2013 to 2014, he was a Post-Doctoral Researcher with the Chalmers University of Technology. From 2014 to 2017, he was with Qamcom Research and Technology AB, Gothenburg. Since 2017, he has been a Professor with

Xi'an Jiaotong University, Xi'an. His research interests include MIMO antennas, over-the-air testing, reverberation chambers, and antenna measurements. He has published more than 200 journal articles on these topics.

Prof. Chen received the IEEE Outstanding Associate Editor Awards six times from 2018 to 2023, and the International Union of Radio Science (URSI) Young Scientist Award 2017 and 2018. He was the General Chair of the IEEE International Conference on Electronic Information and Communication Technology (ICEICT) 2021. He currently serves as a Track Editor for *IEEE Antennas and Wireless Propagation Letters* and an Associate Editor for *IEEE Transactions on Antennas and Propagation*.

A Focused Metasurface Lens Antenna with Gain Enhancement

Yu Dong and Xing Chen

College of Electronic and Information Engineering
Sichuan University, Chengdu 610064, China
yudong0327@163.com, xingc@live.cn

***Abstract* –** A specialized metasurface has been developed for lens antenna applications. This innovative metasurface unit cell comprises five metallic layers and four dielectric layers. Each metallic layer consists of a pair of back-to-back split resonant rings. The proposed unit cell is highly effective with a transmission phase coverage exceeding 360° and a transmission amplitude larger than 70% at X-band (8.8-11.2 GHz). The unit cell has been thoroughly designed, fabricated and tested. To verify the present unit cell, a metasurface array with 27×27 elements is designed. An X-band horn antenna is used as the feed source. Simulation and measurement results show that the electromagnetic wave from the feed horn is focused within the operating band, resulting in a measured gain of 16.9 dB at 9 GHz and 19.2 dB at 11 GHz. Thus, a gain enhancement of 5.4 dB at 9 GHz and 5.7 dB at 11 GHz are obtained, making it a good reference for engineering applications.

***Index Terms* –** metasurface, split resonant ring, wideband.

I. INTRODUCTION

Metasurface technology has rapidly developed and been applied in recent years. Its main function is to regulate the amplitude and phase of electromagnetic waves to achieve various performances, such as digitally reconfigurable antennas [1–5], microwave phase shifters [6], RCS reduction [7], antenna isolation enhancement [8], and filtering antenna [9]. Satellite communication technology has become a fascinating research field, with the main operating frequencies being C-band (4-8 GHz), X-band (12-18 GHz), and Ku-band (27-40 GHz). The currently used satellite communication antennas are mainly parabolic, array, and high gain horn lens antennas. However, metasurface-based transmitarray (TA) antennas or reflect array antennas have shown potential advantages, such as reducing costs, improving gain, and enhancing bandwidth, compared to the commonly used satellite communication antennas [10–19]. Additionally, metasurface technology is more flexible and performs excellently in multifunctional antennas, such as polarization reconfigurable antennas [20–25].

Several relevant papers have been published on wideband-focused metasurface. [26] proposes a double-layer TA consisting of four metal vias and two patches with a 1-dB gain bandwidth of 9.6% (20.1-22.2 GHz). A similar design method is also presented in [27], with a 1-dB gain bandwidth of 9% (17.2-18.8 GHz). In [28], a TA antenna based on a hybrid frequency selective surface (FSS) is proposed, but only a narrow band (at 10 GHz) is introduced. In [29], a TA made of three metallic layers with an air gap is introduced. The proposed TA has a 1-dB gain bandwidth of 15.5%, but the air gap increases the profile of the entire antenna system. In [30], a metasurface that combines the functionalities of TA and reflectarray (RA) is presented. The electromagnetic wave focusing function depends on the polarization mode of the incoming wave, and a 1-dB gain bandwidth (9.14%) from 9.4 to 10.3 GHz is obtained.

This paper studies the wideband focusing metasurface lens antenna with gain enhancement. The metasurface unit cell comprises five metallic layers of pairs of back-to-back split resonant rings. The unit cell comprises five metallic layers and four dielectric layers. The proposed unit cell is highly effective with a transmission phase coverage exceeding 360° and a transmission amplitude above 70% at X-band (8.8-11.2 GHz). The unit cell has been designed, fabricated and tested. To verify the present unit cell, a metasurface array with 27×27 elements is designed, and a X-band horn antenna is used as a feed source. Simulation and measurement results show that the electromagnetic wave from the feed horn is focused within the operating band. When an electromagnetic wave from an X-band feed horn is directed towards it, the metasurface focuses the waves within the operating band that covers 8.8-11.2 GHz. The measured gain is 16.9 dB at 9 GHz and 19.2 dB at 11 GHz. This represents a gain enhancement of 5.4 dB at 9 GHz and 5.7 dB at 11 GHz. The metasurface provides a 1-dB gain bandwidth (5.7%) from 8.8 to 11.2 GHz.

II. DESIGN OF METASURFACE

Figure 1 depicts the proposed unit cell's fundamental structure, which comprising five metallic layers. Each layer consists of a pair of back-to-back split resonant

Submitted On: November 6, 2023
Accepted On: May 16, 2024

https://doi.org/10.13052/2024.ACES.J.391003

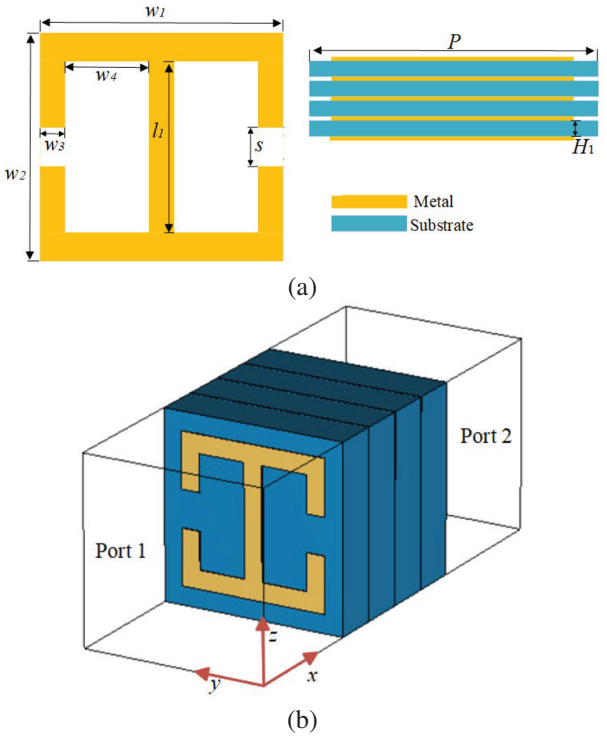

Fig. 1. (a) Geometry model and structure parameters. (b) Configuration of the unit cell.

rings. The dielectric material, Rogers RO3035, is 2.5 mm thickness and has a relative dielectric constant of 3.5. The metasurface unit cell is analyzed using periodic boundaries in the x and y directions through simulation software CST Studio Suite. The transmission phase is highly sensitive to the cutting length s of the split resonant ring. Thus, parameter s is optimized to meet the required phase variation while keeping the other parameters constant.

In general, the metasurface unit cell can be regarded as a two-port network, and its performance is characterized by transmission and reflection coefficients. In this paper, our proposed transmissive metasurface has high transmission coefficients and low reflection coefficients. Therefore, its transmission matrix is concerned, and it can be expressed as the following matrix:

$$T(x,y) = \begin{pmatrix} T_{xx} & T_{yx} \\ T_{xy} & T_{yy} \end{pmatrix}, \quad (1)$$

where T_{xx} and T_{yy} represent the co-polarization transmission coefficients of x-polarized and y-polarized incident waves, and T_{yx} and T_{xy} represent the cross-polarization transmission coefficients of x-polarized and y-polarized incident waves. Since the proposed metasurface structure is symmetric about both the x- and y-axes, cross-polarization transmission coefficients (T_{xy} and T_{yx}) can be regarded as approximately zero. Figure 2 shows the transmission coefficients of the proposed metasurface

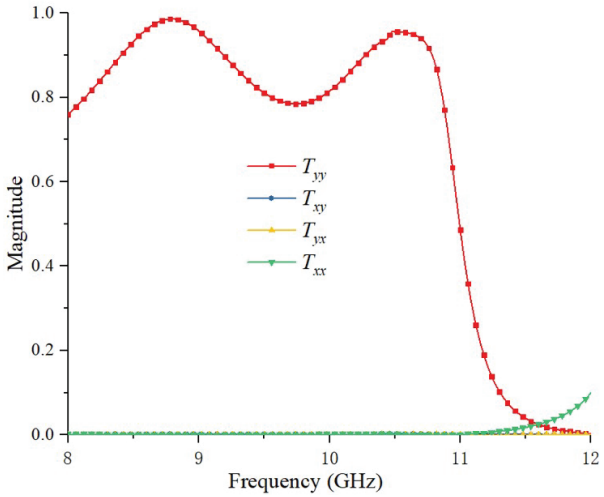

Fig. 2. Transmission coefficients of the proposed metasurface unit cell with $s = 0.1$ mm.

unit cell with $s = 0.1$ mm. We can see that the cross-polarization transmission coefficients (T_{xy} and T_{yx}) are close to zero. At the same time, the co-polarization transmission coefficient T_{xx} is also close to 0 at the concerned frequency. The co-polarization transmission coefficient T_{yy} is greater than 0.7 over a large bandwidth range (8.8-11.2 GHz). The proposed metasurface unit has a grating-like effect, which can filter out x-polarized waves to a certain extent and let y-polarized waves pass through completely.

We can explain the selective transmission function of the unit cell structure by analyzing the electric field distribution. We give the z-component electric field distribution two resonant peaks of 9 GHz and 10.5 GHz. Figure 3 (a) shows the electric field distribution when y-polarization incident on the metasurface unit cell is 9 GHz. It can be seen that there are two pairs of electric field gathering points with opposite intensity at the opening on both sides, forming two pairs of electric dipoles which transmit y-polarized incident waves and carry certain phase mutations as the basis for multi-layer phase superposition. Figure 3 (b) shows the electric field distribution generated by x-polarization incident wave of 9 GHz. No electric dipoles are generated in the figure, indicating that the metasurface structure cannot generate effective resonance for x-polarized waves. Figures 3 (c) and (d) show the electric field distribution of y-polarized and x-polarized incident waves at 10.5 GHz, respectively. Similarly, y-polarized incident waves can generate two pairs of electric dipoles on the metasurface, while x-polarized waves have no such effect. Therefore, we explain the rationality of metasurface energy transmitting y-polarized incident waves while shielding x-polarized incident waves.

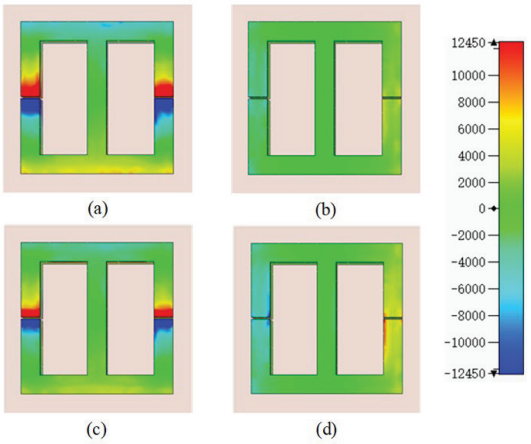

Fig. 3. Electric field distribution of the proposed metasurface unit with $s = 0.1$ mm: (a) y-polarization incident wave at 9 GHz, (b) x-polarization incident wave at 9 GHz, (c) y-polarization incident wave at 10.5 GHz, and (d) x-polarization incident wave at 10.5 GHz.

III. RESULTS AND DISCUSSION

Figure 4 shows the unit cell's simulated transmission magnitude and phase against parameter s under different frequencies. Seen from Fig. 4 (a), the transmission magnitude exceeds 0.7, covering the band 8.8-11.2 GHz when parameter s varies from 0.1 mm to 6.0 mm. The transmission phase is given in Fig. 4 (b). The minimum transmission phase range of about 300° is realized at around 8 GHz, and a transmission phase range over 360° is obtained across 8.8-11.2 GHz. It is reliable to design a metasurface lens antenna within X-band with an elaborate design. The parameters of the proposed unit cell are: $W_1 = 8$, $W_2 = 8$, $W_3 = 1$, $W_4 = 2.5$, $l_1 = 6$, $H_1 = 2.5$, and $P = 10$ (unit = mm). It is worth noting that by changing the value of the parameter s, the phase of the transmitted y-polarized wave can be changed, so free phase manipulation can be achieved.

To efficiently focus the incoming electromagnetic wave, phase difference distribution in the yoz-plane should meet the following [29–31]:

$$\Delta_{\emptyset mn} = \frac{2\pi}{\lambda_0}\left(\sqrt{((mp)^2 + (np)^2 + F^2} - F\right), \qquad (2)$$

where p and F is the periodicity and focal distance of unit cell, $m(n)$ is defined as the number of unit cells in $x(y)$-direction, λ_0 is the free space wavelength, and $\Delta_{\emptyset mn}$ is the phase difference between the unit cell located at mp, np and the unit cell at the initial center ($m = 0$, $n = 0$). The proposed metasurface is designed according to the spatial phase difference distribution in equation (2) to verify the present unit cell. The metasurface is encoded by using an eight-order phase gradient method, the eight unit cells are named No. 1, No. 2, No. 3, No. 4, No. 5, No. 6, No. 7, and No. 8, respectively. The designed metasurface contains three bits of phase information. Each unit cell is designed to have constant phase difference $\Delta = 45°$. The phase difference distribution is shown in Fig. 5, which demonstrates that a transmission phase coverage exceeding 360° is obtained within an operation wavelength. The value of s is selected to be 0.1, 0.3, 1, 2, 3, 4, 5, or 6, which formed the eight different phase difference unit cells, corresponding to the phase information in Fig. 5. The designed layout is shown in Fig. 6 (a). Figure 6 (a) shows the simulated layout configuration of the proposed metasurface lens antenna. An X-band horn is used as the feed source. It is placed a focal distance of D. The electromagnetic wave focusing distance D is set to 50 mm. The metasurface has a dimension of $L \times L = 270 \times 270$ mm^2. The phase distributions for electromagnetic wave focusing distance D of 50 mm are shown in Fig. 6 (b).

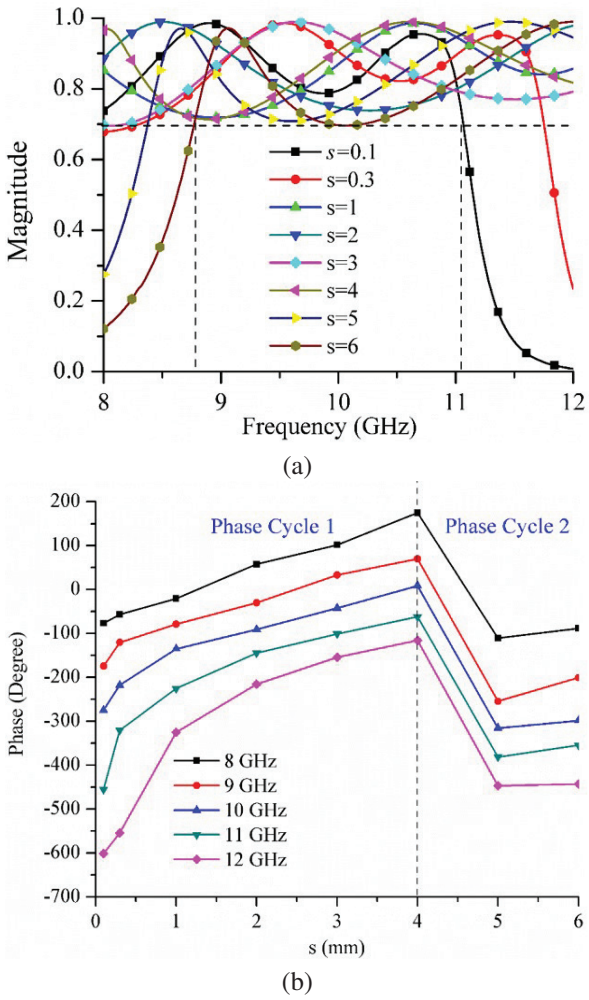

Fig. 4. (a) Transmission magnitude of unit cell. (b) Transmission phase of unit cell.

The designed metasurface is fabricated based on printed circuit board technology, seen in Fig. 7 (a). The dielectric material is Rogers RO3035, with 2.5 mm thickness and a relative dielectric constant of 3.5. Figure 7 (b) exhibits the photo of the fabricated metasurface lens antenna and its experimental installation in the anechoic chamber. A planar near field test system is used for radiation parameters measurement, which is especially suitable for high gain antenna testing [32–35]. An X-band standard horn antenna is used as the feed source, and the distance between the metasurface and the horn is $D =$ 50 mm. The reflection coefficients of the feed horn with and without metasurface are given in Fig. 8, showing that the reflection coefficients are less than -10 dB across the X-band.

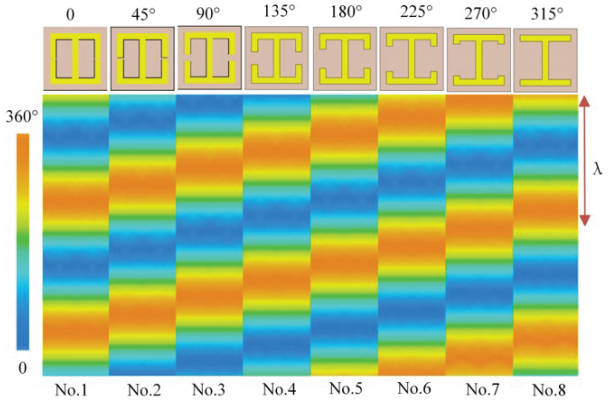

Fig. 5. Phase gradient difference of the eight unit cells.

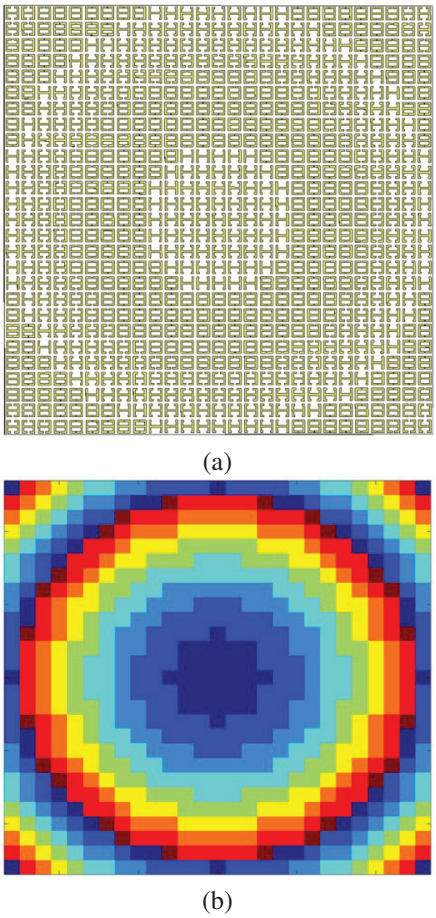

Fig. 6. (a) Layout of the metasurface. (b) Phase distributions for electromagnetic wave focusing distance D of 50 mm.

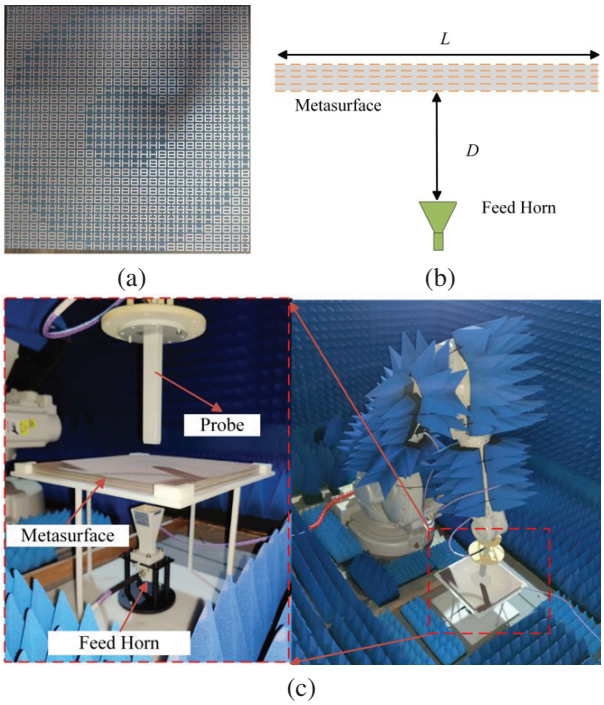

Fig. 7. (a) The fabricated metasurface photograph. (b) Experimental test and diagnostics setup.

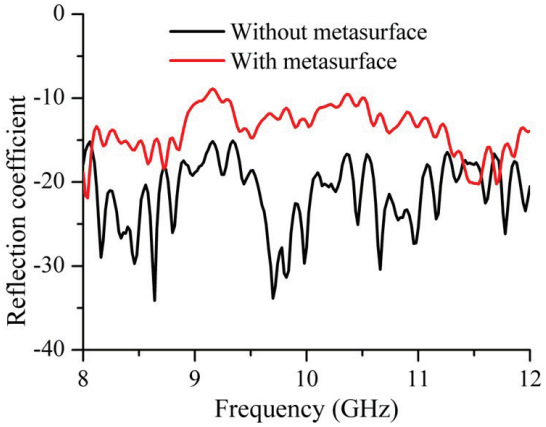

Fig. 8. Feed horn measured reflection coefficient with and without metasurface.

Figure 9 shows the simulated 3D radiation patterns at 9 GHz and 11 GHz. The designed metasurface shows a very strong electromagnetic wave focus capability. The gain patterns of the metasurface lens antenna and feed horn are depicted in Fig. 10, both in simulation and measurement. The gain of the feed horn is 11.5 dBi at 9 GHz and 13.5 dBi at 11 GHz. Meanwhile, the metasurface lens antenna displays measured gains of 16.9 dBi at 9 GHz and 19.2 dB at 11 GHz. As a result, a gain enhancement of 5.4 dB and 5.7 dB are achieved at 9 GHz and 11 GHz, respectively. Figure 10 also presents the simulated and measured 2D radiation pattern in the *xoz*-plane and *yoz*-plane at 9 GHz and 11 GHz. The tested gains are almost in line with the simulated results, with a difference of 0.45 dB less than the simulation gain at 9 GHz and 0.6 dB less than the simulation gain at 11 GHz. This discrepancy can be attributed to the fabrication tolerance of metasurface and the loss of the printed circuit board. According to [30], the aperture efficiency can be calculated by $\eta = \mathrm{G/D}_{max} = \mathrm{G}/(4\pi \times \mathrm{P} \times \mathrm{Q}/\lambda_0^2) \times 100\%$, with $\mathrm{P} = \mathrm{Q} = 270$ mm being the length and width of the lens antenna system, respectively. The measured aperture efficiency at 9 GHz (11 GHz) is about 5.9% (6.7%).

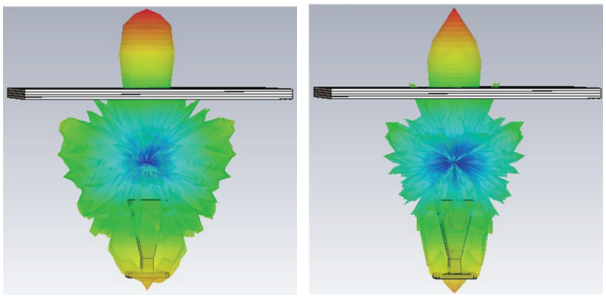

(a) (b)

Fig. 9. Simulated 3D radiation pattern: (a) 9 GHz and (b) 11 GHz.

The presented design is compared with the referenced antennas, as shown in Table 1. The designed metasurface lens antenna reflects certain advantages in terms of comprehensive performance, such as 1-dB gain bandwidth and profile. For [11, 13], the 1-dB gain bandwidth is only 3.4% and 5.4%, respectively. The proposed metasurface unit cell has the advantage of a low profile ($0.33\times\lambda_0$ mm) and a large transmission phase range (360°) with a large operating bandwidth (8.8-11.2 GHz). For the unit cell transmission and amplitude, the proposed unit cell has a relative balanced advantage of satisfying 360° phase variety and high amplitude transmission (≥0.7). Furthermore, the four-layer identical unit cell structure makes the proposed metasurface easily set to apply to other working frequencies.

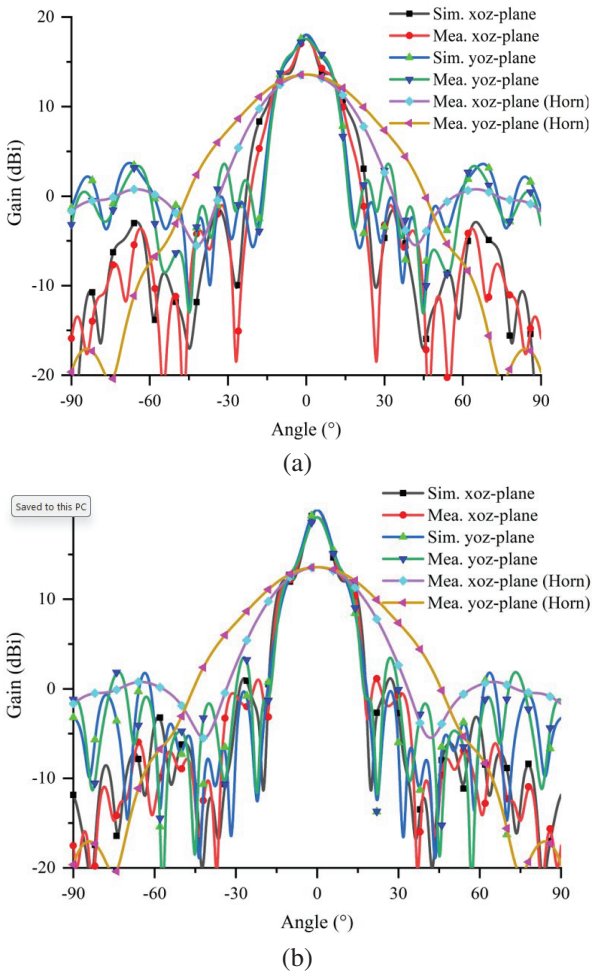

Fig. 10. Simulated and measured patterns of the proposed metasurface lens antenna: (a) 9 GHz and (b) 11 GHz.

Table 1: Comparison of the proposed TA with referenced ones

Ref.	Freq.	1 dB Gain BW	Unit Transmission Phase	Unit Transmission Amplitude	Profile
[11]	9.4-10.6	3.4%	≥215°	≥0.72	$0.2\times\lambda_0$
[12]	11-12.5	8.4%	≥360°	≥0.60	$0.68\times\lambda_0$
[13]	11.65-12.3	5.4%	≥265°	≥0.75	$0.08\times\lambda_0$
[14]	29	7.5%	≥360°	≥0.71	$1.0\times\lambda_0$
[15]	11.3	9%	≥360°	≥0.89	$0.45\times\lambda_0$
[29]	9.4-11.2	15.5%	≥360°	≥ 0.71	$0.43\times\lambda_0$
This work	8.8-11.2	5.7%	≥360°	≥ 0.70	$0.33\times\lambda_0$

IV. CONCLUSION

This paper proposes a new type of metasurface for lens antenna applications. This metasurfaces unit cell comprises five metallic layers with split resonant rings positioned back-to-back. The metasurface comprises five metallic layers on a 2.5 mm thick dielectric substrate. The unit cell provides a transmission phase coverage of over 360° with a transmission amplitude of over 70% at the X-band frequency range of 8.8-11.2 GHz. The metasurface has been designed and verified on a 2.5 mm thick dielectric substrate. When an electromagnetic wave from an X-band feed horn is directed towards it, the metasurface focuses the waves within the operating band that covers 8.8 to 11.2 GHz. The measured gain is 16.9 dB at 9 GHz and 19.2 dB at 11 GHz. This represents a gain enhancement of 5.4 dB at 9 GHz and 5.7 dB at 11 GHz. The metasurface provides a 1-dB gain bandwidth (5.7%) from 8.8 to 11.2 GHz. The proposed metasurface is a good reference for engineering applications.

REFERENCES

[1] B. Rana, I.-G. Lee, and I.-P. Hong, "A 4×4 digitally reconfigurable transmitarray: measurement of radiation patterns," *IEICE Electron. Express*, vol. 19, 20210550, 2022.

[2] Y. Zhang, Z. Han, X. Lv, K. Yan, Z. Weng, and Z. Wu, "Novel one-bit digital coding broadband transmits array antenna," *IEICE Electron. Express*, vol. 17, 20200195, 2022.

[3] S. Yu, L. Li, and N. Kou, "One-bit digital coding broadband reflectarray based on fuzzy phase control," *IEEE Antennas Wireless Propag. Lett*., vol. 16, pp. 1524-1527, 2017.

[4] C. D. Giovampaola and N. Engheta, "Digital metamaterials," *Nat. Mater.*, vol. 13, pp. 1115-1121, 2014.

[5] T. J. Cui, M. Q. Qi, X. Wan, J. Zhao, and Q. Cheng, "Coding metamaterials, digital metamaterials and programmable metamaterials," *Light Sci. Appl.*, vol. 3, e218, 2014.

[6] M. A. Al-Jocularly and N. Behdad, "Wideband planar microwave lenses using sub-wavelength spatial phase shifters," *IEEE Trans. Antennas Propag.*, vol. 59, no. 12, pp. 4542-4552, 2011.

[7] T.-B. Nguyen, N. Kinai, N. Michishita, H. Morishita, T. Miyazaki, and M. Tadokoro, "Dual-polarized metasurface using multi-layer ceramic capacitors for radar cross section reduction," *IEICE Transactions on Communications*, vol. E103.B, no. 8, pp. 852-859, 2020.

[8] G. Zhao, T. Liu, J. Jiang, L. Zhao, G.-L. Huang, and W. Lin, "Polarization selective partial reflective decoupling layers for mutual coupling reduction of two closely spaced dual-polarized antennas," *IEEE Transactions on Antennas and Propagation*, vol. 70, no. 11, pp. 11205-11210, 2022.

[9] W. Yang, S. Chen, Q. Xue, W. Che, G. Shen, and W. Feng, "Novel filtering method based on metasurface antenna and its application for wideband high-gain filtering antenna with low profile," *IEEE Trans. Antennas Propag.*, vol. 67, no. 3, pp. 1535-1544, 2019.

[10] Y. M. Pan, P. F. Hu, X. Y. Zhang, and S. Y. Zheng, "A low-profile high-gain and wideband filtering antenna with metasurface," *IEEE Trans. Antennas Propag.*, vol. 64, no. 5, pp. 2010-2016, 2016.

[11] J.-J. Liang, G.-L. Huang, J.-N. Zhao, Z.-J. Gao, and T. Yuan, "Wideband phase gradient metasurface antenna with focused beams," *IEEE Access*, vol. 7, pp. 206767-206772, 2019.

[12] X. Zhong, H.-X. Xu, L. Chen, W. Li, H. Wang, and X. Shi, "An FSS-backed broadband phase-shifting surface array with multimode operation," *IEEE Trans. Antennas Propag.*, vol. 67, no. 9, pp. 5974-5981, 2019.

[13] C. Tian, Y.-Q. Lu, G. Zhao, Y.-C. Jiao, and L.-X. Guo, "Double-layer transmitarray antenna using specially designed substrate," *IEEE Antennas Wireless Propag. Lett.*, vol. 21, no. 3, pp. 441-445, 2022.

[14] C. G. M. Ryan, M. R. Chaharmir, J. Shaker, J. R. Bray, Y. M. M. Antar, and A. Ittipiboon, "A wideband transmitarray using dual resonant double square rings," *IEEE Trans. Antennas Propag.*, vol. 58, no. 5, pp. 1486-1493, 2010.

[15] A. H. Abdelrahman, A. Z. Elsherbeni, and F. Yang, "High-gain and broadband transmitarray antenna using triple-layer spiral dipole elements," *IEEE Antennas Wireless Propag. Lett.*, vol. 13, pp. 1288-1291, 2014.

[16] Q. Luo, S. Gao, M. Sobhy, and X. Yang, "Wideband transmit array with reduced profile," *IEEE Antennas Wireless Propag. Lett.*, vol. 17, no. 3, pp. 450-453, 2018.

[17] X. Lv, Z. Han, X. Jian, Y. Zhang, and Q. Chen, "A wideband transmit array using triple-layer elements with reduced profile," *IEICE Electron. Express*, vol. 17, 20190678, 2020.

[18] C. Tian, Y.-C. Jiao, G. Zhao, and H. Wang, "A wideband transmitarray using triple-layer elements combined with cross slots and double square rings," *IEEE Antennas Wireless Propag. Lett.*, vol. 16, pp. 1561-1564, 2017.

[19] M. Faenzi, G. Minatti, and S. Maci, "Metasurface antennas: Design and performance," *IEICE Transactions on Communications*, vol. E102.B, no. 2, pp. 174-181, 2019.

[20] G.-M. Zhang, J.-S. Hong, and B.-Z. Wang, "A novel pattern reconfigurable wideband slot antenna using PIN diodes," in *International Conference*

on Microwave and Millimeter Wave Technology, 2010.

[21] R. Lian, Z. Tang, and Y. Yin, "Design of a broadband polarization-reconfigurable Fabry-Perot resonator antenna," *IEEE Antennas Wireless Propag. Lett.*, vol. 17, no. 1, pp. 122-125, 2018.

[22] S.-L. Chen, F. Wei, P.-Y. Qin, Y. Jay Guo, and X. Chen, "A multi-linear polarization reconfigurable unidirectional patch antenna," *IEEE Trans. Antennas Propag.*, vol. 65, no. 8, pp. 4299-4304, 2017.

[23] W. Lin and H. Wong, "Polarization reconfigurable aperture-fed patch antenna and array," *IEEE Access*, vol. 4, pp. 1510-1517, 2016.

[24] A. Bhattacharjee, S. Dwari, and M. K. Mandal, "Polarization-reconfigurable compact monopole antenna with wide effective bandwidth," *IEEE Antennas Wireless Propag. Lett.*, vol. 18, pp. 1041-1045, 2019.

[25] Y. J. Liu and Y. H. Ge, "Polarization-reconfigurable flat transmitarray based on square frame and crossed dipole elements," *IEICE Transactions on Communications*, vol. E100. B, pp. 1904-1910, 2017.

[26] X. Yi, T. Su, X. Li, B. Wu, and L. Yang, "A double-layer wideband transmitarray antenna using two degrees of freedom elements around 20 GHz," *IEEE Trans. Antennas Propag.*, vol. 67, no. 4, pp. 2798-2802, 2019.

[27] X.-J. Yi, T. Su, B. Wu, J.-Z. Chen, L. Yang, and X. Li, "A double-layer highly efficient and wideband transmitarray antenna," *IEEE Access*, vol. 7, pp. 23285-23290, 2019.

[28] C.-H. Lee and J.-H. Lee, "Low profile high-efficiency transmitarray antenna based on hybrid frequency selective surface," *IEICE Transactions on Communications*, vol. E104. B, no. 1, pp. 49-54, 2021.

[29] B. Rahmati and H. R. Hassani, "High-efficient wideband slot transmitarray antenna," *IEEE Trans. Antennas Propag.*, vol. 63, no. 11, pp. 5149-5155, 2015.

[30] T. Cai, G.-M. Wang, X.-L. Fu, J.-G. Liang, and Y.-Q. Zhuang, "High-efficiency metasurface with polarization dependent transmission and reflection properties for both reflectarray and transmit array," *IEEE Trans. Antennas Propag.*, vol. 66, no. 6, pp. 3219-3224, 2018.

[31] H. Hao, X. Ran, Y. Tang, S. Zheng, and W. Ruan, "A single-layer focusing metasurface based on induced magnetism," *Progress in Electromagnetics Research*, vol. 172, pp. 77-88, 2021.

[32] J. Zheng, X. Chen, and Y. Huang, "An effective antenna pattern reconstruction method for planar near-field measurement system," *IEEE Transactions on Instrumentation and Measurement*, vol. 71, Art. no. 8005012, 2022.

[33] J. Zheng, C. Pan, Z. Wang, L. Zhang, and X. Chen, "An efficient data reconstruction method for broadband planar near-field measurements based on the field distribution similarity," *IEEE Transactions on Instrumentation and Measurement*, vol. 72, Art. no. 1008514, 2023.

[34] J. Tang, X. Meng, X. Chen, R. Chen, Y. Da, S. Zhu, A. Zhang, and M. Yu, "Efficient angle calibration method for peak beam measurements in transmitarray-based compact antenna test range," *IEEE Transactions on Electromagnetic Compatibility*, vol. 65, no. 6, pp. 1941-1951, 2023.

[35] J. Tang, X. Chen, X. Meng, Z. Wang, Y. Ren, C. Pan, X. Huang, M. Li, and A. A. Kishk, "Compact antenna test range using very small F/D transmitarray based on amplitude modification and phase modulation," *IEEE Transactions on Instrumentation and Measurement*, vol. 71, Art. no. 8001614, 2022.

Yu Dong completed her masters in Electronic Communication Engineering from the University of Electronic Science and Technology of China, Chengdu, Sichuan Province, in 2009. Currently, she is pursuing a doctoral degree in electronic communication engineering at Sichuan University. Her research focuses on microwave and antenna arrays.

Xing Chen received the M.S. degree in radio physics and the Ph.D. degree in biomedical engineering from Sichuan University, Sichuan, China, in 1999 and 2004, respectively. He is currently a Professor with the College of Electronics and Information Engineering, Sichuan University. His main research interests include antenna and microwave imaging. Dr. Chen is a Senior Member of the Chinese Institute of Electronics.

A Low-profile Wideband Pattern Reconfigurable Antenna with Metasurface

GuangRui Liu[1], Cheng Ju[1], Zijie Li[1], Zhiqun Yang[2], Xiaoyun Qu[2], Na Liu[1], and Wei-hua Zong[1]

[1]College of Electronics and Information
Qingdao University, Qingdao, 266000, China
liu-guang-rui@qq.com, jucheng719@qdu.edu.cn, lizijie@qdu.edu.cn, liunana@qdu.edu.cn, weihuazong@126.com

[2]Shandong Institute of Space Electronic Technology
Yantai, 264003, China
yyangzq@163.com, selina.qu@163.com

***Abstract* –** This paper presents a pattern reconfigurable antenna with low-profile and wide bandwidth. The antenna is composed of a patch layer, a metasurface (MS) layer, and a full ground plane. The radiation patch consists of a microstrip-fed square and three parasitic patches. The MS with 4×4 units is added on the top of the patch layer to improve bandwidth as well as tune radiation pattern. Ten of the MS units are available to connect with the ground plane, each of which is loaded with a PIN diode to control the shorting state, providing 12 beam states with reconfigurable beams between ±5° to ±15° both in *xoz* and *yoz* planes. The proposed antenna has been fabricated and measured. Measurement shows that the antenna has a wide impedance bandwidth of 4.02-5.72 GHz, a beam scanning range of -16°-15° in *xoz* plane and -13°-15° in *yoz* plane, peak gain range of 4.94-6 dBi. With a planar shape of low profile and full ground plane, the antenna design is a good candidate to be applied in wireless communication systems with conductive surface.

***Index Terms* –** 5G antenna, low-profile, metasurface (MS), pattern reconfigurable antenna, wideband antenna, WLAN antenna.

I. INTRODUCTION

Pattern reconfigurable antennas have the capability to reconfigure radiation patterns to satisfy the requirements from communication systems of transmission efficiency improvement, transmission interference reduction and transmission quality enhancement. These kinds of antennas have found applications in the fields of vehicle communication, the Internet of Things, etc. [1–5].

The phased array antenna, although an effective approach for pattern reconfiguration, comes with bulk volume, high cost, and realizes beam pointing control through the integration of antenna elements, phase shifters, power splitters, and feed networks. Introducing liquid crystal [6] or liquid metal [7] to tune material's permittivity or reshape the antenna's structure can also obtain pattern reconfiguration, however these methods involve difficulties of fast tuning as well as low efficiency.

Electrically controlling an antenna beam based on PIN diodes [8–23] offer advantages of fast modulation speed and compact structure which is desired in low-cost communication terminals. In these antennas, those with full ground plane [10–21] have virtues of good directivity and high gain. They are also immune to influence when mounted on conductive surfaces, such as vehicles, aircrafts, metallic walls, human bodies, etc. Therefore, antennas with full ground plane are more appealing in practical applications. Nevertheless, planar antennas with full ground plane come usually with narrow bandwidth [10–13]. Introducing an air gap [14–21] between ground plane and radiation patch is a commonly used solution to reduce the ground plane's influence. However increased height may bring instability problems and the inconvenience of being mounted on and conformal with the antenna supporter. Metasurface (MS) has been adopted in antenna configuration to improve bandwidth and reduce coupling with low profile [24–29], whereas pattern reconfiguration is unavailable in these antennas.

This paper aims to improve the bandwidth of pattern reconfigurable antenna considering low profile. A patch antenna with full ground plane is chosen as the driven element. Antenna bandwidth is improved by adding MS on top of the antenna. Some MS units are controlled by PIN diodes to connect/disconnect with the ground plane to obtain 12 reshaped patterns.

II. ANTENNA CONFIGURATION AND OPERATION STATES

Figure 1 shows configuration of the proposed antenna. The antenna consists of three layers, a full ground plane at the bottom, radiation patches in the

Submitted On: November 28, 2023
Accepted On: May 20, 2024

https://doi.org/10.13052/2024.ACES.J.391004

middle layer, and a MS as the top layer. The radiation patches are composed of a square patch directedly fed by a step shaped microstrip line and three parasitic patches. The MS with 4×4 squares is adopted to obtain wideband impedance matching as well as pattern reconfiguration. Ten of the MS units are connected with the ground plane through via holes. Each via holes pad inside the MS unit is split with other parts of the unit by slits and loaded with a PIN diode to connect the via hole. Therefore, each unit can be controlled shorted/open with the ground plane to obtain pattern reconfiguration. Two FR4 boards each with a 1.5 mm thickness, a relative permittivity of 4.4 and a relative loss tangent value of 0.02 are used as substrates. The lumped components of each PIN diode's DC bias network are L1=L2=15 nH, L3=2.2 nH, R=200 Ω, and C=10 pF. The antenna dimensions are listed in Table 1. The PIN diodes used in this design are of Infineon BAR64-02V.

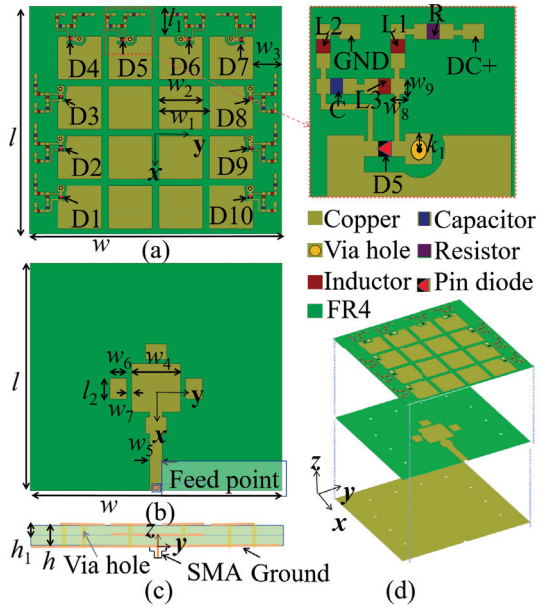

Fig. 1. Configuration of the proposed antenna: (a) top layer, (b) middle layer, (c) side view, and (d) 3D-view.

Table 1: Dimensions of the proposed antenna

Par.	Value (mm)	Par.	Value (mm)	Par.	Value (mm)
w	60	l	55	h	3
w_1	12	l_1	7.3	h_1	1.5
w_2	10.4	l_2	5	k_1	0.5
w_3	6.8	w_6	4	w_9	0.8
w_4	11.6	w_7	1.2		
w_5	3	w_8	0.83		

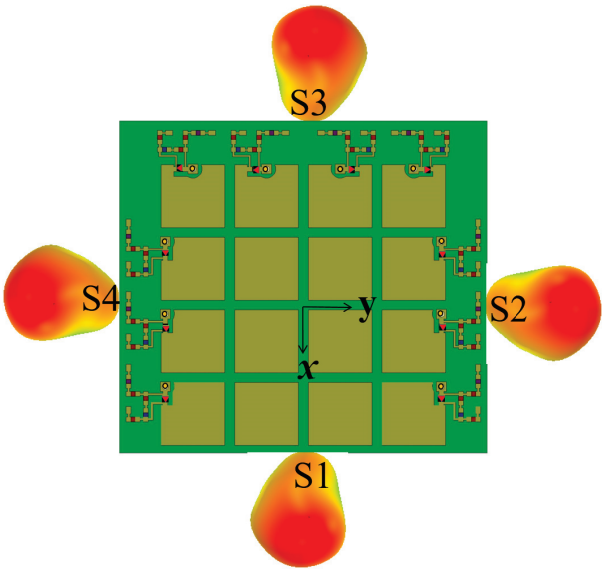

Fig. 2. Simulated 3-D radiation patterns for the proposed antenna at 5 GHz.

The proposed antenna can operate at 12 states with different beam directions listed in Table 2. In this table, the binary numbers in the second column refer to each PIN diode's working state: "1" means the PIN diode is turned on, and "0" means off. As shown in Table 2, the proposed antenna's beam can be steadily tuned from ±5° to ±15° with a step of 5°, both in *xoz* (φ=0°) and *yoz* (φ=90°) planes. Figure 2 illustrates the radiation patterns of four typical operating states.

Table 2: Operating states of the proposed antenna at 5 GHz

State	D1-D10	Beam (θ, φ)	Max Gain (dBi)
S1	0001111000	θ= +14° in *xoz* plane	7.41
S2	1111000000	θ= +15° in *yoz* plane	6.36
S3	1100000011	θ= -14° in *xoz* plane	5.66
S4	0000001111	θ= -16° in *yoz* plane	5.99
S5	0001001000	θ= +7° in *xoz* plane	7.08
S6	0101000000	θ= +9° in *yoz* plane	6.47
S7	1000000001	θ= -8° in *xoz* plane	6.13
S8	0000001010	θ= -9° in *yoz* plane	6.16
S9	0010000100	θ= +5° in *xoz* plane	6.70
S10	0110000000	θ= +5° in *yoz* plane	6.55
S11	0100000010	θ= -5° in *xoz* plane	6.42
S12	0000000110	θ= -5° in *yoz* plane	6.46

III. ANTENNA DESIGN AND ANALYSIS

A. Antenna configuration design

Simulations are performed using the EM field simulator ANSYS High Frequency Simulation Software

(HFSS). The antenna design was conducted initially from bandwidth enhancement without considering beam reconfiguration. Figure 3 shows the design evolution with three reference antennas, and Fig. 4 gives simulated S_{11} of these antennas. As shown in Fig. 3 (a), ANT-1 is a traditional square-shaped patch antenna fed with a microstrip line. As shown in Fig. 4, ANT-1 excites the first resonance at 6.37 GHz which is traditionally a quarter wavelength resonance. By adding a MS layer on the top of ANT-1's patch layer, ANT-2's first resonance drops to 4.15 GHz, and a second resonance is excited at 4.91 GHz, which results in an improved bandwidth of 3.98-5.18 GHz. Based on ANT-2, three parasite patches are added around the driven patch, and the feedline is modified to a step shape forming ANT-3. As shown in Fig. 4, ANT-3 excites three resonances (4.53, 5.26, 5.67 GHz) below 6 GHz, resulting in wider bandwidth of 3.96-5.78 GHz. Figure 5 illustrates the 3-D radiation pattern of ANT-3 at 5 GHz. As shown, ANT-3 has a bore-sight maximum radiation pattern with a peak gain of 6.56 dBi.

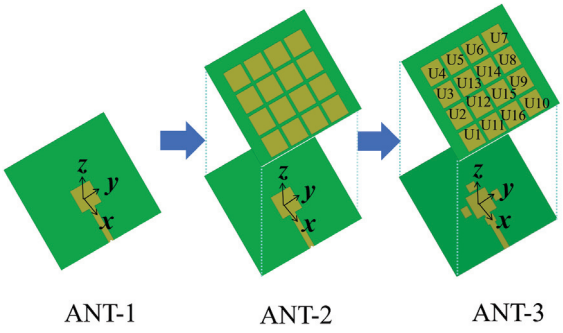

Fig. 3. Antenna configuration design evolution.

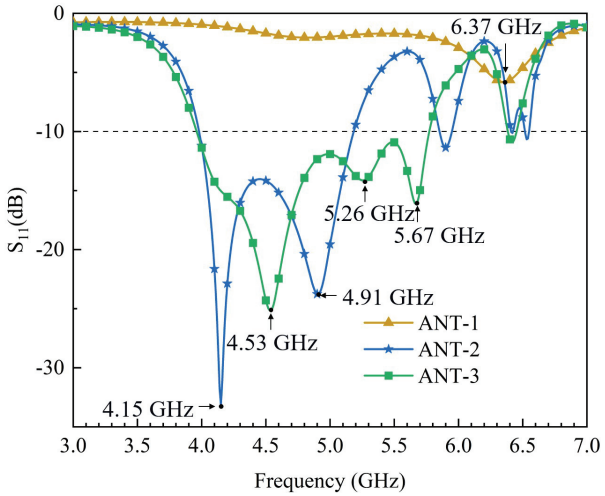

Fig. 4. Simulated S_{11} of reference antennas.

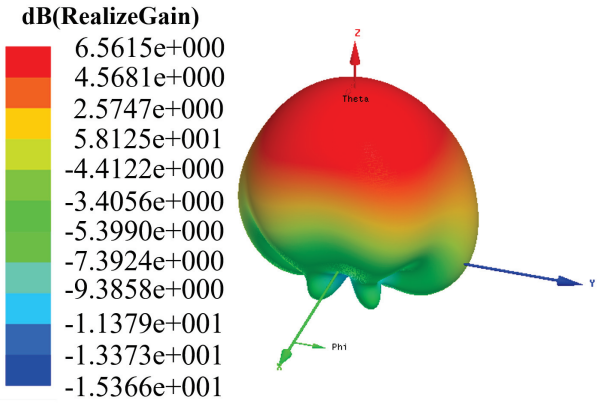

Fig. 5. Simulated 3-D radiation pattern of ANT-3 at 5 GHz.

B. Mechanism of pattern reconfiguration

Based on the configuration of ANT-3, each MS unit tried to connect with the ground plane through a via hole to obtain titled radiation beam. The shorting position was arranged at the corner of each unit to reduce the influence on antenna bandwidth. Figure 6 illustrates radiation patterns and current distributions of ANT-3 with some MS units shorted. As shown in Fig. 6 (a), when only one unit (U1) is shorted, the current distributions on U1 becomes weaker than those on other units. This means that electromagnetic fields induced by U1 is bounded in the near region with little radiating to the far region which results in a tilted radiation pattern with main beam at θ=5°, φ=120°. As shown in Fig. 6 (b), when four MS units at the left side (U1, U2, U3, and U4) are shorted, a larger tilted beam (θ=15°, φ=90°) is obtained. Similar approach is also presented in [30,31] which added shorting pins to the parasitic patches on the same layer with the driven patches. To the authors' best knowledge, it's the first time shorting pins were added on the MS patches which are in a different layer with the radiation patch to tune radiation patterns.

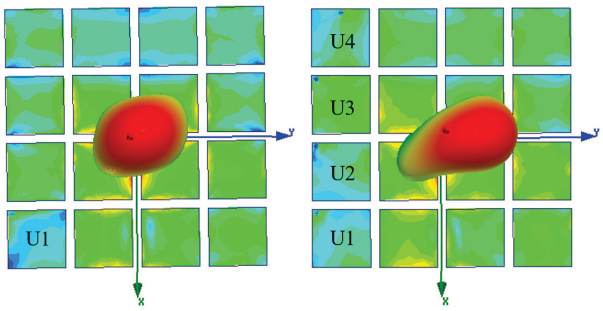

(a) U1 shorted (b) U1, U2, U3, U4 shorted

Fig. 6. Simulated current distributions and radiation patterns of ANT-3 with some MS units shorted.

Theoretically, each of the 16 units can be tuned with shorted/open with ground plane forming 2^{16} reconfigurable patterns. Nevertheless, not all the patterns are reasonable for engineering application, and the convenience of installing PIN diodes and DC bias network in the design needs also be considered. Therefore, we chose the 10 units (U1-U10) located at three edges to form 12 working states with reconfigurable patterns.

C. DC bias network and pattern reconfiguration realization

To electrically control each MS unit shorted/open with the ground plane, slits are etched around each via hole with loading a PIN diode. The DC bias network to power each PIN diode is shown in Fig. 1, which is similar with the one in [32]. The antenna's operation states are given in Table 2.

Figure 7 shows simulated S_{11} of the proposed antenna at six states (S1, S2, S5, S6, S9, S10). As shown, the proposed antenna has similar bandwidth with ANT-3 at these six states. The other six states (S3, S4, S7, S8, S11, S12) have similar S_{11} plots with the former ones which are not included in the figures. The common bandwidth for the 12 states is 3.96-5.78 GHz.

Figures 8 and 9 illustrate simulated patterns in *xoz* and *yoz* planes at 5 GHz, respectively. As shown in Fig. 8, the proposed antenna achieves titled beams in *xoz* plane at θ=14°, θ=-14°, θ=+7°, θ=-8°, θ=+5°, and θ=-5° at S1, S3, S5, S7, S9, and S11 states. Figure 9 shows that the antenna achieves titled beams in *yoz* plane at θ=15°, θ=-16°, θ=+8°, θ=-9°, θ=+5°, and θ=-5° at S2, S4, S6, S8, S10, and S12 states.

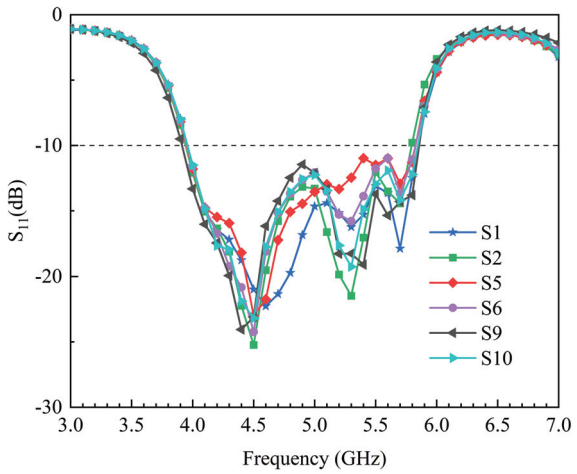

Fig. 7. Simulated S_{11} of the proposed antenna.

The positions of the PIN diodes and the shape of the slit have been optimized to reduce the influence on

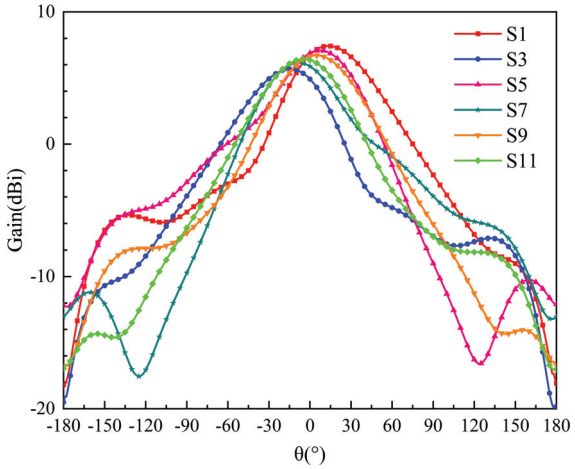

Fig. 8. Simulated radiation pattern in *xoz* plane at 5 GHz.

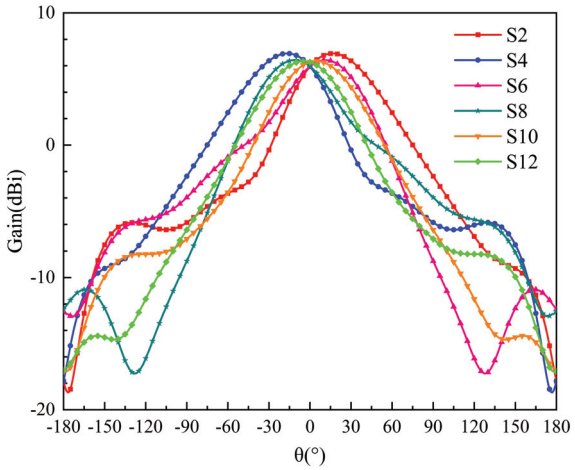

Fig. 9. Simulated radiation pattern in *yoz* plane at 5 GHz.

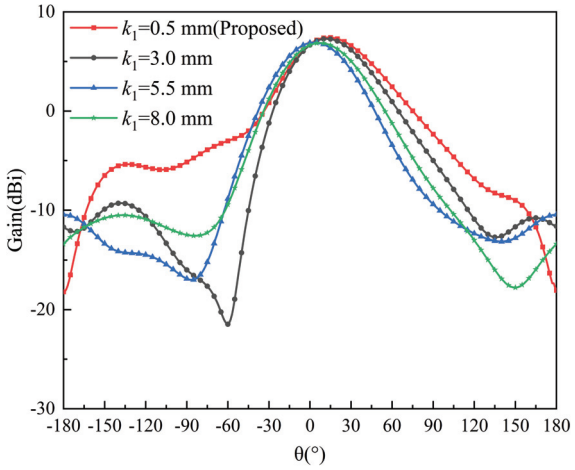

Fig. 10. Simulated radiation pattern in the *xoz* plane at State 1 varying with k_1.

antenna's pattern. Figure 10 shows simulated pattern in the *xoz* plane at state 1 varying with k_1 (the position of each via hole). As shown, smaller k_1 results in higher gain. The value of k_1 is set as 0.5 mm to provide enough area to contain a via hole.

IV. RESULTS AND DISCUSSION

The proposed antenna has been fabricated and measured. Figure 11 shows a photograph of the fabricated antenna, in which each PIN diode is powered by a button battery assembled in a battery container.

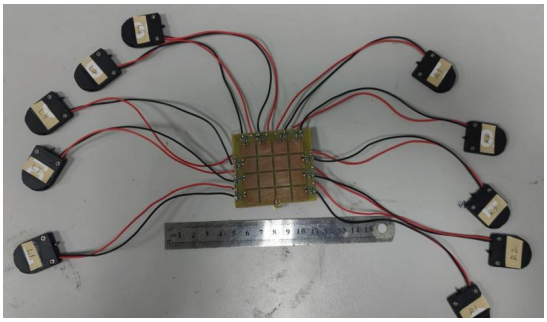

Fig. 11. Photograph of the fabricated antenna.

The proposed antenna was measured at S1, S2, S3, and S4 states. Measured S_{11} is illustrated in Fig. 12 which shows that the antenna has similar bandwidth in these four states, and a common bandwidth of 4.02-5.72 GHz. Radiation patterns of the four states at 4.8, 5, and 5.2 GHz are shown in Figs. 13–15, respectively. As shown in the figures, measurement agrees well with simulation. The proposed antenna achieves pattern reconfiguration both in *xoz* and *yoz* planes. Table 3 lists measured peak gains and beams. As shown, the antenna realizes pattern reconfigurations ranging from -16° to 15° in *xoz* plane, and -13° to 15° in *yoz* plane. Maximum gain in the working states ranges from 4.94 to 6 dBi.

Table 4 compares the performance of the antenna

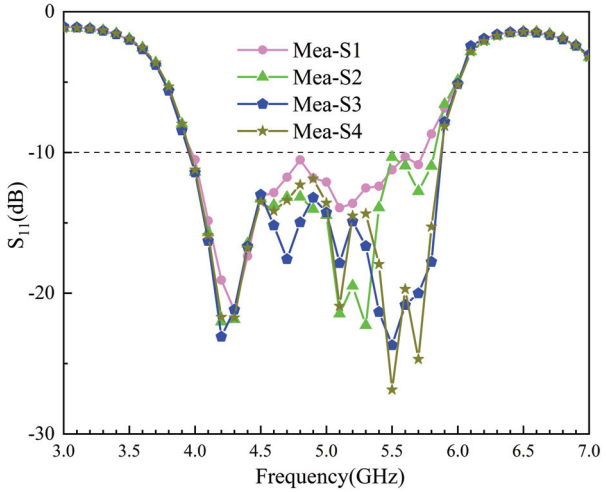

Fig. 12. Measured S_{11} of the proposed antenna.

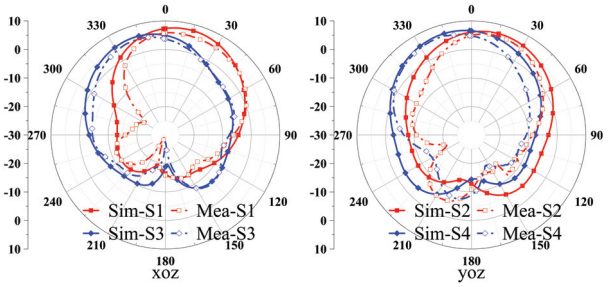

(a) (b)

Fig. 13. Measured radiation pattern at 4.8 GHz.

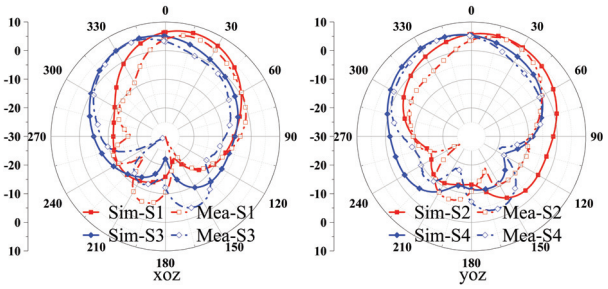

(a) (b)

Fig. 14. Measured radiation pattern at 5.0 GHz.

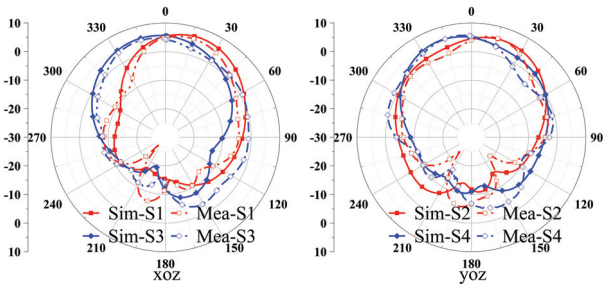

(a) (b)

Fig. 15. Measured radiation pattern at 5.2 GHz.

Table 3: Measured peak beam and peak gain

	4.8 GHz		5 GHz		5.2 GHz	
	Beam (θ,φ)	Gain (dBi)	Beam (θ,φ)	Gain (dBi)	Beam (θ,φ)	Gain (dBi)
S1	(15°,0°)	5.94	(14°,0°)	5.96	(16°,0°)	5.87
S2	(15°,90°)	5.91	(15°,90°)	5.88	(16°,90°)	5.82
S3	(-16°,0°)	4.94	(-14°,0°)	4.96	(-15°,0°)	5.01
S4	(-13°,90°)	6.00	(-16°,90°)	5.83	(-14°,90°)	5.62

Table 4: Comparison of the proposed antenna with published pattern-reconfigurable antennas

Ref.	BW (GHz)	BW (%)	Size (λ^3)	Peak Gain (dBi)	Number of PIN Diodes	Number of States	Beam Direction	Beam Range (°)
[9]	3.54-4.46	23	3×1.24×0.05	7.67	18	5	1D	±55
[10]	2.45-2.45	3.8	0.45×0.45×0.02	3.86	4	2	N/A	N/A
[11]	2.45-2.45	4.0	1.7×2×0.007	7.1	8	2	N/A	N/A
[13]	5.5-5.98	11.3	1×2×0.06	N/A	2	2	1D	±50
Pro.	4.02-5.72	34	1×0.95×0.05	4.94-6	10	12	2D	-16°-15° in *xoz* -13°-15° in *yoz*

proposed in this paper with that of the beam-reconfigurable antennas in the references. As shown, the proposed antenna has virtues of smaller size, wider bandwidth and more tunable states with reconfigurable patterns.

V. CONCLUSION

In this paper we have designed a pattern reconfigurable antenna based on a microstrip-fed patch antenna with full ground plane. A 4×4 MS is adopted to improve bandwidth as well as realize pattern reconfiguration. Ten of the MS units are loaded with PIN diodes to control the connection/disconnection with the ground plane. DC bias network is arranged outside each MS unit and near its edge to maintain wide bandwidth and obtain good radiation pattern. By controlling each PIN diode's ON/OFF state, 12 states with different titled patterns are obtained. Antenna fabrication and measurement have been conducted to validate simulations. Measurement shows that the proposed antenna covers impedance bandwidth of 4.02-5.72 GHz and pattern reconfiguration bandwidth of 4.8-5.2 GHz. The antenna works at 12 pattern reconfiguration states ranging from -16° to 15° in *xoz* and -13° to 15° in *yoz* plane. The proposed antenna has a small size $1\times0.95\times0.05\lambda^3$. With a full ground plane and low profile, the proposed antenna is a good candidate applied in metallic vehicles.

λ is the free space wavelength at the central operational frequency, Pro.=proposed.

ACKNOWLEDGMENT

This work was supported by the Natural Science Foundation of Shandong Province, China (No. ZR2020MF023).

REFERENCES

[1] Y. X. Cao, S. Yan, J. X. Li, and J. Chen, "A pillbox based dual circularly-polarized millimeter-wave multi-beam antenna for future vehicular radar applications," *IEEE Transactions on Vehicular Technology*, vol. 71, no. 7, pp. 7095-7103, July 2022.

[2] L. Y. Wang, H. Y. Shi, X. M. Chen, B. Y. Qu, J. J. Yi, A. X. Zhang, Z. Xu, and H. W. Liu, "Multibeam MS antenna enabled by orbital angular momentum demultiplexing feeding for IoT communication," *IEEE Internet of Things Journal*, vol. 10, no. 18, pp. 16169-16182, Sep. 2023.

[3] J. Z. Tang, X. S. Meng, X. M. Chen, R. H. Chen, Y. R. Da, S. T. Zhu, A. X. Zhang, and A. A. Kishk, "Efficient angle calibration method for peak beam measurements in transmitarray-based compact antenna test range," *IEEE Transactions on Electromagnetic Compatibility*, 2023.

[4] Y. P. Wang, X. M. Chen, H. L. Pei, W. E. I. Sha, Y. H. Huang, and A. A. Kishk, "MIMO performance enhancement of MIMO arrays using PCS-based near-field optimization technique," *Science China Information Sciences,* vol. 66, no. 6, pp. 1-16, June 2023.

[5] Y. S. Li, W. X. Li, and Q. B. Ye, "Miniaturization of asymmetric coplanar strip-fed staircase ultrawideband antenna with reconfigurable notch band," *Microwave and Optical Technology Letters,* vol. 55, no. 7, pp. 1467-1470, 2013.

[6] H. Kim, J. Kim, and J. Oh, "Communication a novel systematic design of high-aperture-efficiency 2D beam-scanning liquid-crystal embedded reflectarray antenna for 6G FR3 and radar applications," *IEEE Transactions on Antennas and Propagation*, vol. 70, no. 11, pp. 11194-11198, Nov. 2022.

[7] Z. S. Qu, J. R. Kelly, Z. P. Wang, S. Alkaraki, and Y. Gao, "A reconfigurable microstrip patch antenna with switchable liquid-metal ground plane," *IEEE Antennas and Wireless Propagation Letters*, vol. 22, no. 5, pp. 1045-1049, May 2023.

[8] J. X. Chen, Y. H. Ke, L. L. Yang, and W. W. Yang, "Pattern-reconfigurable dielectric resonator antenna with endfire beam-scanning feature," *IEEE Antennas and Wireless Propagation Letters*, vol. 21, no. 7, pp. 1398-1402, July 2022.

[9] C. J. You, S. H. Liu, J. X. Zhang, X. Wang, Q. Y. Li, G. Q. Yin, and Z. G. Wang "Frequency-and pattern-reconfigurable antenna array with broadband tuning and wide scanning angles," *IEEE Transactions*

on Antennas and Propagation, vol. 71, no. 6, pp. 5398-5403, June 2023.

[10] G. P. Gao, B. K. Zhang, J. H. Dong, Z. H. Dou, Z. Q. Yu, and B. Hu, "A compact dual-mode pattern-reconfigurable wearable antenna for the 2.4-GHz WBAN application," *IEEE Transactions on Antennas and Propagation*, vol. 71, no. 2, pp. 1901-1906, Feb. 2023.

[11] H. Naseri, P. PourMohammadi, N. Melouki, A. Iqbal, and T. A. Denidni, "A low-profile antenna system for generating reconfigurable OAM-carrying beams," *IEEE Antennas and Wireless Propagation Letters*, vol. 22, no. 2, pp. 402-406, Feb. 2023.

[12] S. T. Wang, L. Zhu, and H. Deng, "Design approach for pattern-reconfigurable patch antenna without extra feeding networks," *IEEE Transactions on Antennas and Propagation*, vol. 71, no. 2, pp. 1925-1930, Feb. 2023.

[13] R. Wang, B. Z. Wang, G. F. Gao, X. Ding, and Z. P. Wang, "Low-profile pattern-reconfigurable vertically polarized endfire antenna with magnetic-current radiators," *IEEE Antennas and Wireless Propagation Letters*, vol. 17, no. 5, pp. 829-832, May 2018.

[14] Z. Wang, S. X. Liu, and Y. D. Dong, "Compact wideband pattern reconfigurable antennas inspired by end-fire structure for 5G vehicular communication," *IEEE Transactions on Vehicular Technology*, vol. 71, no. 5, pp. 4655-4664, May 2022.

[15] J. F. Li, B. Wu, J. Q. Zhou, K. X. Guo, H. R. Zu, and T. Su, "Frequency and pattern reconfigurable antenna using double layer petal shaped parasitic structure," *IEEE Transactions on Circuits and Systems II: Express Briefs*, 2023.

[16] K. D. Hong, X. Zhang, L. Zhu, and T. Yuan, "A high-gain and pattern-reconfigurable patch antenna under operation of TM20 and TM21 modes," *IEEE Open Journal of Antennas and Propagation*, vol. 2, pp. 646-653, 2021.

[17] J. A. Liu, Y. F. Cao, and X. Y. Zhang, "A pattern-reconfigurable filtering patch antenna using embedded resonators and switchable elements," *IEEE Transactions on Antennas and Propagation*, vol. 70, no. 5, pp. 3828-3833, May 2022.

[18] R. K. Dutta, R. K. Jaiswal, M. Saikia, and K. V. Srivastava, "A two-stage beamforming antenna using butler matrix and reconfigurable frequency selective surface for wide angle beam tilting," *IEEE Antennas and Wireless Propagation Letters*, vol. 22, no. 10, pp. 2342-2346, Oct. 2023.

[19] Y. T. Jia, G. S. Jiang, Y. Liu, and Y. C. Zhong, "Beam scanning for dual-polarized antenna with active reflection metasurface," *IEEE Antennas and Wireless Propagation Letters*, vol. 21, no. 9, pp. 1722-1726, Sep. 2022.

[20] Z. Wang, and Y. D. Dong, "Metamaterial-based, vertically polarized, miniaturized beam-steering antenna for reconfigurable sub-6 GHz applications," *IEEE Antennas and Wireless Propagation Letters*, vol. 21, no. 11, pp. 2239-2243, Nov. 2022.

[21] S. N. Zhao, Z. Wang, and Y. D. Dong, "Pattern-reconfigurable antenna using low-profile electric and magnetic radiators," *IEEE Antennas and Wireless Propagation Letters*, vol. 22, no. 3, pp. 616-620, Mar. 2023.

[22] W. M. Abdulkawi, A. A. Sheta, W. A. Malik, S. U. Rehman, and M. S. Alkanhal, "RF MEMS switches enabled H-shaped beam reconfigurable antenna," *Applied Computational Electromagnetics Society Journal*, vol. 34, no. 09, pp. 1312–1319, Sep. 2019.

[23] Y. Zhang, D. Sun, T. Dong, and J. Yin, "Design of reconfigurable patch antenna in frequency, pattern, and switchable polarization," *Applied Computational Electromagnetics Society Journal*, vol. 35, no. 9, pp. 1037–1046, Sep. 2020.

[24] T. Shi, R. L. Chai, X. M. Chen, M. Li, T. Zhang, and M. C. Tang, "A low-profile, circularly polarized, metasurface-based antenna with enhanced bandwidth and stable high gain," *IEEE Antennas and Wireless Propagation Letters, vol.* 22, no. 2, pp. 253-257, Aug. 2022.

[25] K. E. Kedze, H. Wang, and I. Park, "A metasurface-based wide-bandwidth and high-gain circularly polarized patch antenna," *IEEE Transactions on Antennas and Propagation*, vol. 70, no. 1, pp. 732-737, Jan. 2022.

[26] H. H. Tran, C. D. Bui, N. Nguten-Trong, and T. K. Nguyen, "A wideband non-uniform metasurface-based circularly polarized reconfigurable antenna," *IEEE Access,* vol. 9, pp. 42325-42332, Mar. 2021.

[27] Y. S. Li, W. X. Li, and W. H. Yu, "A switchable UWB slot antenna using SIS-HSIR and SIS-SIR for multi-mode wireless communications applications," *Applied Computational Electromagnetics Society Journal*, vol. 27, no. 4, pp. 340-351, Apr. 2012.

[28] J. F. Jiang, Y. F. Xia, and Y. S. Li, "High isolated X-band MIMO array using novel wheel-like metamaterial decoupling structure," *Applied Computational Electromagnetics Society Journal,* vol. 34, no. 12, pp. 1829-1836, Dec. 2019.

[29] S. Y. Luo, Y. S. Li, Y. F. Xia, G. H. Yang, L. J. Sun, and L. Zhao, "Mutual coupling reduction of a dual-band antenna array using dual-frequency metamaterial structure," *Applied Computational Electromagnetics Society Journal*, vol. 34, no. 3, pp. 403-410, Mar. 2019.

[30] T. Sabapathy, M. F. Jamlos, R. B. Ahmad, M. Jusoh, and M. I. Jais, "A reconfigurable microstrip rectangular parasitic array antenna," *2013 IEEE Symposium on Wireless Technology & Applications*, Kuching, Malaysia, Sep. 2013.

[31] A. Meredov, K. Klionovski, and A. Shamim, "Screen-printed, flexible, parasitic beam-switching millimeter-wave antenna array for wearable applications," *IEEE Open Journal of Antennas and Propagation*, vol. 1, pp. 2-10, 2020.

[32] Q. Q. Liu, Z. K. Geng, R. Zhao, S. D. Li, Z. Yao, and W. H. Zong, "A wideband planar pattern reconfigurable antenna for IEEE 802.11 ac WLAN applications" *International Journal of RF and Microwave Computer-Aided Engineering*, vol. 32, no. 10, pp. 23323, July 2022.

GuangRui Liu was born in Qingdao, Shandong, Province, China, in 1997. In 2020, he received the B.S. degree in communication engineering from Changsha University of Science & Technology, Changsha, Hunan, Province, China. He is currently pursuing the M.S. degree in new-generation electronic information technology at Qingdao University, Qingdao, China. His current research interests include broadband antennas and reconfigurable antennas.

Cheng Ju received the Ph.D. degree from Beijing University of Posts and Telecommunications in 2015. He joined the School of Electronic Information at Qingdao University in 2017 as a lecturer. He is mainly engaged in researching DSP algorithms for space laser communication systems and FPGA implementation of DSP algorithms.

Zijie Li received the B.S. degree in Electromagnetic Field and Wireless Technology from the Nanjing University of Posts and Telecommunications, Nanjing, China, in 2021. He is currently pursuing the M.S. degree with the school of electronic information, Qingdao University, Qingdao, China. His current research interests include circularly polarized antennas, metamaterial-based antennas, and reconfigurable antennas.

Zhiqun Yang received the Ph.D. degree in communication and information system from Nanjing University of Technology, Nanjing, Jiangsu Province, China, in 2003. He is with Shandong Institute of Space Electronic Technology, China Aerospace Science and Technology Corporation, Yantai, China, as a Senior Engineer. His research interest is signal processing and communication.

Xiaoyun Qu was born in Yantai City, Shandong Province, China, in 1974. She received the B.S. in applied mathematics from Yantai University, in 1996, M.S. degree in electromagnetic fields and microwave technology from Nanjing Electronics research Center, Nanjing, Jiangsu Province, China, in 1990. She is with Shandong Institute of Space Electronic Technology, Yantai, China, as a Senior Engineer. Her research interest is antenna design.

Na Liu received the Ph.D. degree from Beijing University of Posts and Telecommunications in 2015. She joined the School of Electronic Information at Qingdao University in 2018 as a lecturer. She is mainly engaged in researching DSP algorithms for coherent detection systems.

Wei-hua Zong was born in Penglai City, Shandong Province, China, in 1975. She received the B.S. in applied mathematics from Yantai University, in 1997, M.S. degree in electromagnetic fields and microwave technology from Nanjing Electronics research Center, Nanjing, Jiangsu Province, China, in 2000, and the Ph.D. degree in electromagnetic fields and microwave technology from Xidian University, Xian, Shanxi Province, China, in 2004. In 2004, she joined Qingdao University, Qingdao, Shandong Province, China, as a lecture. Since 2005, she has been an Associate Professor in Qingdao University. From February to August 2010, she was a Visiting Scholar Assistant with Electrical and Computation Engineering Department, National University of Singapore. Her research interests include antenna design and electromagnetic material measurement.

A High-Gain Vivaldi Antenna Loaded with Metasurface for Broadband Applications

Kun Li[1], Zijie Li[1], Xiaorui Liu[2], Shandong Li[1], Xiaoyun Qu[3], Zhiqun Yang[3], and Wei-hua Zong[1]

[1]College of Electronics and Information
Qingdao University, Qingdao, 266000, China
likun6366@qq.com, lizijie@qdu.edu.cn, lishd@qdu.edu.cn, weihuazong@126.com

[2]Automation School, Institute of Future
Qingdao University, 266000, Shandong, China
liuxiaorui@qdu.edu.cn

[3]Shandong Institute of Space Electronic Technology
Yantai 264003, China
selina.qu@163.com, yyangzq@163.com

Abstract – In this article, a Vivaldi antenna with broad bandwidth and high gain is proposed. The proposed antenna consists of a coplanar Vivaldi antenna (CVA) configuration etched with two rhombus slots at both sides of the radiation arm to improve bandwidth and gain at the low frequencies as well as maintaining antenna miniaturization. A compact broadband metasurface is loaded in the dielectric region between the two exponentially tapered lines to improve radiation performance in a wide frequency range without increasing antenna size. The antenna has been fabricated and measured, obtaining 1.27-9.4 GHz bandwidth covering L/S/C/X and ultra-wideband (UWB) lower bands. The measured gain ranges from 3 dBi to 9.67 dBi. With a miniaturized size of $100\times100\times1$ mm^3, good directional radiation pattern and high gain in the whole working band, the proposed antenna is a good candidate for the applications in multi-band coverage systems.

Index Terms – broadband antennas, coplanar Vivaldi antennas (CVA), metasurface, multiband antennas.

I. INTRODUCTION

Multiband coverage ultra-wideband antenna not only has the broadband performance of ultra-wideband antenna, but also covers the operating frequency band of a variety of applications, so that only one broadband antenna is needed to meet the design metrics that can be achieved by combining multiple antennas, such as base station antenna system [1–4], which greatly enhances the performance of electronic information systems, reduces the complexity of system architecture, and effectively alleviates the shortage of frequency spectrum resources and space resources. Vivaldi antenna [5] are widely used in wideband antenna design due to its performance of directional radiation, linear polarization, and low profile. To further improve the antenna's bandwidth, coplanar Vivaldi antenna (CVA) [6–15], antipodal Vivaldi antenna (AVA) [16–23], and balanced antipodal Vivaldi antenna (BAVA) [24] have been proposed and applied in ground penetrating radar [6–8, 13], medical imaging [9, 10, 16–19], and mobile communication systems [11, 12].

For some applications, such as long-distance point-to-point communication and directional coverage communication, antennas are required with high radiation gain. Using multiple antenna elements to form an antenna array is an effective method to obtain high gain [11]. To reduce the antenna array's volume and cost, an antenna element with a small size and high gain is preferred. The commonly used methods to improve a Vivaldi antenna element's gain include integrating a spherical-axicon dielectric lens with the antenna [25, 26], and introducing metasurfaces in the tapered radiation aperture of the antenna [13, 14, 20, 21]. In the forementioned techniques, mounting a dielectric lens with complicated stereoscopic increases the antenna's volume and fabrication cost, and adding metasurfaces enlarges the antenna's footprint.

To obtain antenna miniaturization, much work has been done using a high dielectric constant dielectric substrate [16], etching slots in the radiation section [18], [19], and half-cutting the antenna [27]. Arlon AR1000 with a high relative permittivity of 9.8 was used as the

Submitted On: November 2, 2023
Accepted On: May 7, 2024

https://doi.org/10.13052/2024.ACES.J.391005

substrate of the antenna [16]. Meanwhile, [16, 18, 19] slotted on AVA's radiation arm to broaden antenna bandwidth at low frequency, but it was ignored that AVA itself has large cross-polarization, which affects antenna radiation performance. In [27], the CVA was half-cut along the antenna's central axis which resulted in an asymmetrical structure and caused a directional pattern distortion and the directivity deteriorated.

It is challenging to design an antenna with wideband bandwidth, small size, high radiation gain, and good linear performance. In this article, an ultra-wideband Vivaldi antenna based on the traditional CVA is presented, with two rhombus slots etched in both sides of the antenna radiation arm, and the broadband metasurface loaded in the exponential tapered radiation region. The proposed antenna obtains a wide operating bandwidth of 1.27-9.4 GHz with the measured $S11 < -10$ dB. It covers L (1.27-2 GHz), S (2-4 GHz), C (4-8 GHz), and X (8-9.4 GHz) bands as well as UWB (3.1-9.4 GHz) bands, suitable for ground penetrating radar, medical imaging, and communication systems.

II. ANTENNA CONFIGURATION

The configuration of the proposed antenna is shown in Fig. 1. The proposed antenna is obtained based on a traditional Vivaldi antenna by etching two rhombus-shaped slots on the two radiation arms to improve antenna bandwidth. A broadband metasurface structure is added in the exponentially tapered radiation region to improve antenna gain. The metasurface structure is arranged in the non-metal region with symmetric structure and can maintain miniaturization and improve performance, which is also adopted in [28–32] to reduce mutual coupling. The proposed antenna is fed with a microstrip line connected with an impedance transform line and a sector-shaped balun with a tension angle of 103°. The antenna is printed on a 1 mm thick FR4 dielectric substrate, with a dielectric constant of 4.4 and a loss tangent of 0.02. Table 1 lists the optimized geometric dimensions. The proposed antenna was simulated by HFSS 15.0.

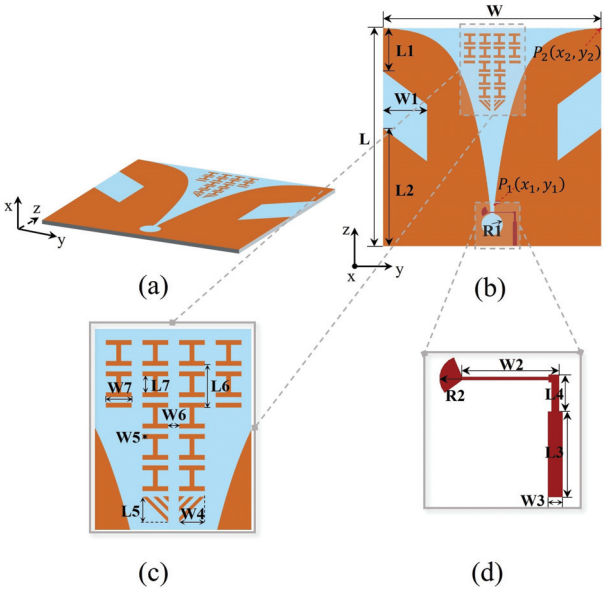

Fig. 1. Configuration of the proposed antenna: (a) 3-D view, (b) radiation structure, (c) metasurface structure, and (d) feed structure.

Table 1: Dimensions of the proposed antenna

Par.	Value (mm)	Par.	Value (mm)	Par.	Value (mm)
L	100	L3	10.85	L6	6
W	100	W3	1.85	W6	2
L1	20	L4	4.68	L7	3
W1	20	W4	5	W7	5
L2	54	L5	5	R1	5
W2	12	W5	1	R2	3

III. ANTENNA SIMULATION AND ANALYSIS

A. Antenna design

The proposed antenna was designed from a traditional CVA by etching two slots and loading metasurface. To illustrate the design process of the proposed antenna, three reference antennas (Ant I, Ant II, and Ant III) are presented in Fig. 2. The antennas' reflection coefficients and radiation patterns are given in Figs. 3 and 4, respectively.

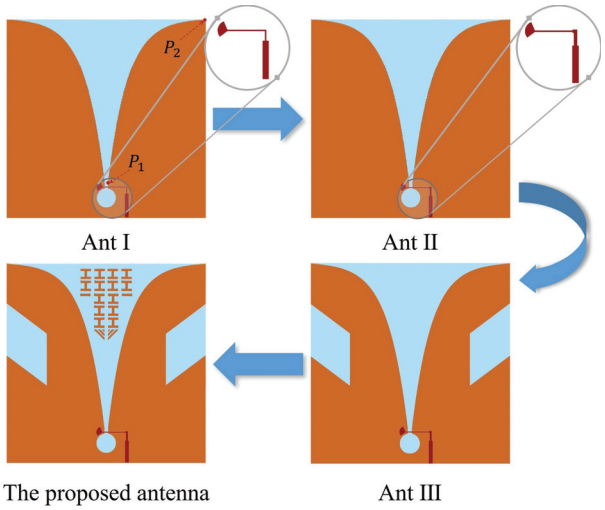

Fig. 2. Evolution of the proposed antenna.

As shown in Fig. 2 (a), Ant I is a traditional CVA fed with a step-shaped microstrip and fan-shaped balun. The step-shaped microstrip acts as an impedance transformer to obtain wideband impedance matching. The theoretical formula of the exponential tapered curve of a traditional CVA is:

$$y = Ae^{cx} + B, \tag{1}$$

where the values A and B in (1) can be calculated from the coordinates of the beginning point P_1 (x_1, y_1) and the terminal point P_2 (x_2, y_2) of the exponential tapered curve by the following equations:

$$A = \frac{y_2 - y_1}{e^{cx_2} - e^{cx_1}}, \tag{2}$$

$$B = \frac{y_1 e^{cx_2} - y_2 e^{cx_1}}{e^{cx_2} - e^{cx_1}}, \tag{3}$$

where the value of c is optimized as 0.1 which determines the curvature of the exponential tapered curve and affects the impedance bandwidth of the antenna.

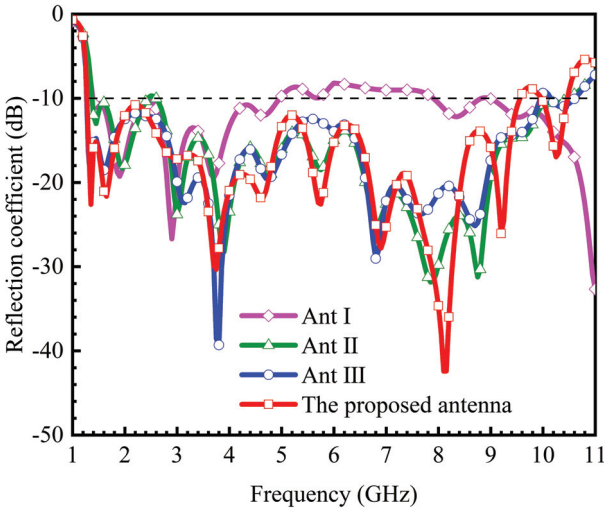

Fig. 3. Reflection coefficients of reference antennas and the proposed antenna.

The exponentially curved profile was proven to be a self-scaling configuration providing frequency-independent behavior [33]. As depicted in Fig. 3, Ant I's −10 dB bandwidth is 1.4-5 GHz. The antenna's reflection coefficients are higher than −10 dB at frequencies 5-7.9 GHz. A second-ordered impedance transformer is adopted in Ant II's feeding strip to improve the impedance matching at higher frequencies 5-10.4 GHz. However, the reflection coefficients at 2.4-2.6 GHz are slightly higher than −10 dB. A rhombus slot is etched in Ant III at the side edge of each radiation patch to reduce reflections at lower frequencies. As shown in Fig. 3, Ant III obtains low reflection coefficients both in lower

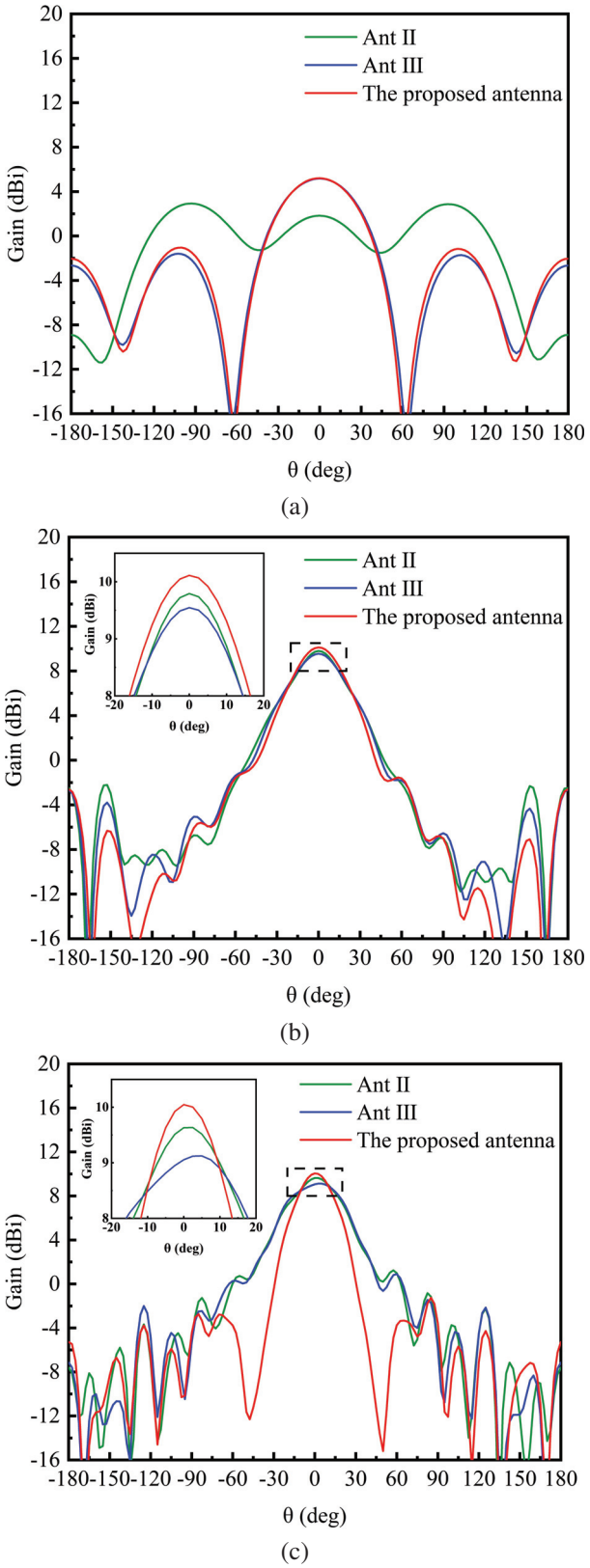

Fig. 4. The far-field radiation pattern in *yoz*-plane of reference antennas and the proposed antenna at (a) 1.4 GHz, (b) 6 GHz, and (c) 8 GHz.

and higher frequencies with bandwidth covering 1.27-9.9 GHz. Based on Ant III, a broadband metasurface is added in the opening region of the radiation part. As shown in Fig. 3, the proposed antenna's reflection coefficients remain similar to Ant III at the lower frequencies, whereas they become a bit higher at frequencies above 8 GHz. The proposed antenna has a bandwidth of 1.27-9.4 GHz, which is a bit narrower than Ant III. The adoption of a metasurface is to improve antenna radiation pattern and gain which is discussed in the following.

As shown in Fig. 4 (a), Ant II has two side lobes at $\theta=\pm 95^\circ$ with higher gain values than the main beam at $\theta=0^\circ$ at 1.4 GHz, which are caused by the electric field distributing along the edge of the bottom plate edge as shown in Fig. 5 (a). Ant III and the proposed antenna have a lower side lobe at 1.4 GHz. As shown in Fig. 4 (b), Ant III and the proposed antenna have higher peak gain at $\theta=0^\circ$ and lower back lobe at $\theta=\pm 150^\circ$ at 6 GHz. As shown in Fig. 4 (c), the proposed antenna has a higher peak gain and narrower main beam than Ant III and Ant II at 8 GHz. These results indicate that adding the two rhombus-shaped slots can improve antenna radiation patterns at lower frequencies, and adding the metasurface can improve antenna radiation patterns at higher frequencies. The broadband metasurface has been well designed and maintains a wide bandwidth covering 1.27-9.4 GHz as shown in Fig. 3.

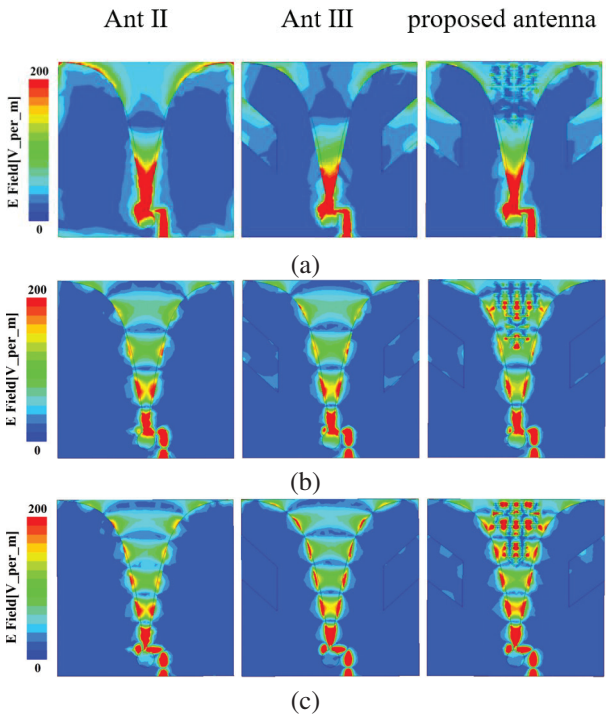

Fig. 5. The electric field distributions of Ant II, Ant III, and the proposed antenna at: (a) 1.4 GHz, (b) 6 GHz, and (c) 8 GHz.

B. Electric field distribution analysis

The electric field distributions of Ant II, Ant III, and the proposed antenna on the top layers at 1.4 GHz, 6 GHz, and 8 GHz are given in Fig. 5. As shown in Fig. 5 (a), strong electric fields distribute at the bottom edge near the feeding port for Ant II, resulting in a sidelobe higher than the main beam at 1.4 GHz (shown in Fig. 4 (a)). It can also be seen from Fig. 5 (a) that the electric fields distribution at the bottom edges of Ant III and the proposed antenna become much weaker than Ant II, which results in a lower sidelobe as shown in Fig. 4 (a). Comparing electric field distributions of Ant III and the proposed antenna at 6 GHz and 8 GHz shown in Figs. 5 (b) and (c), it can be seen that more electric fields are introduced in the area near the opening region of the two exponential curves with the adoption of the metasurface which improves radiation pattern at higher frequencies as shown in Figs. 4 (b) and (c).

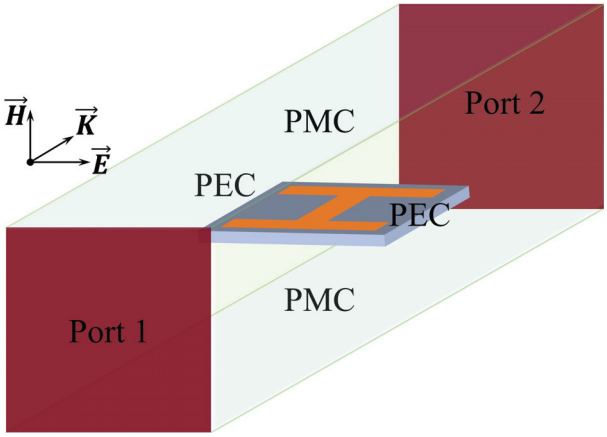

Fig. 6. Simulation setup of the unit cell.

S-parameters of the metasurface unit cell are simulated by using the model shown in Fig. 6. PEC and PMC boundary conditions are set in the model. Figure 7 shows the simulated S-parameters. As shown, S_{11} is less than -7 dB, and S_{21} is higher than -1 dB in the frequency band of 1-11 GHz, which indicates that the metasurface structure has broadband performance. The relative permittivity of the broadband metasurface has been simulated and computed by using the equivalent medium theory [34]. Figure 8 shows simulated results. As can be seen, the values of relative permittivity are around 1 at frequencies higher than 1.5 GHz, which provides good impedance matching between the antenna and the air and improves the radiation performance.

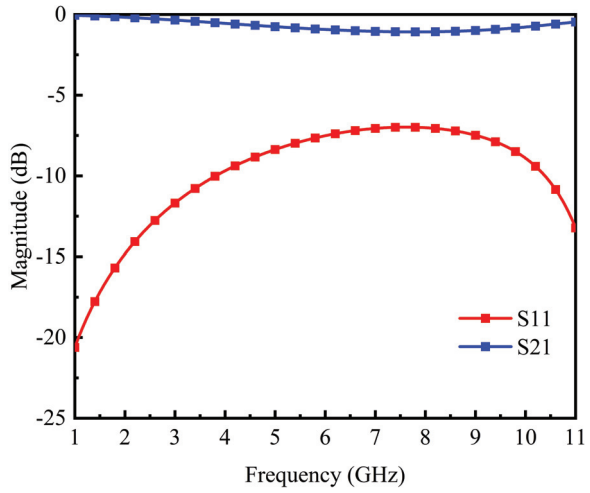

Fig. 7. Simulated S-parameters of the metasurface unit cell.

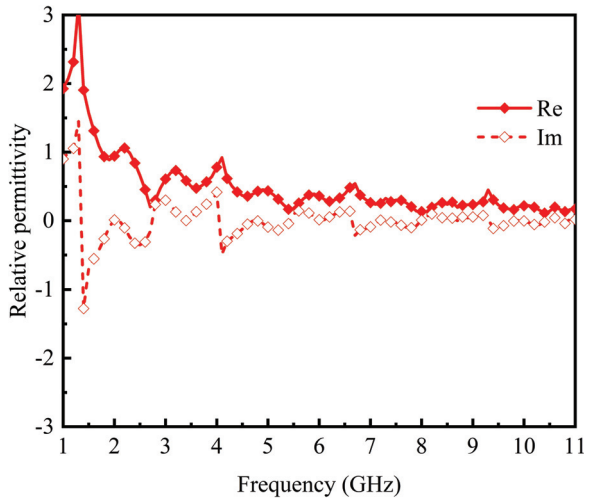

Fig. 8. Retrieved relative permittivity of the metasurface.

IV. RESULTS AND DISCUSSION

The prototype of the proposed antenna has been fabricated and measured. Figure 9 shows photographs of the fabricated antenna. Measured reflection coefficients are illustrated in Fig. 10. It can be observed that the measurement agrees well with the simulation, and the measured bandwidth with reflection coefficient lower than −10 dB is 1.27-9.4 GHz, covering L (1.27-2 GHz), S (2-4 GHz), C (4-8 GHz), X (8-9.4 GHz), and UWB lower (3.1-4.5 GHz) bands.

The simulated and measured gain plots are shown in Fig. 11. Figure 12 presents the radiation pattern in *xoz* and *yoz* planes of the antenna at 1.5 GHz, 3 GHz, 5 GHz, 7 GHz, and 9 GHz, respectively. As shown, measurement agrees well with simulation, and the antenna has good

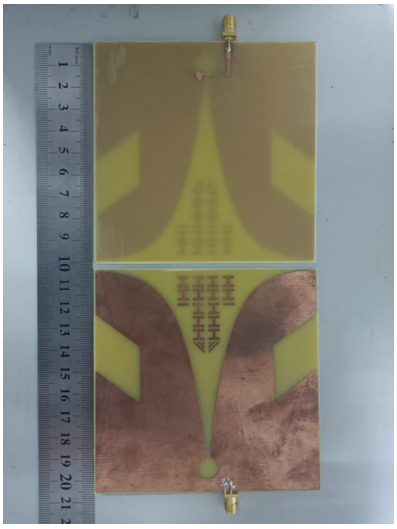

Fig. 9. Photograph of the fabricated antenna.

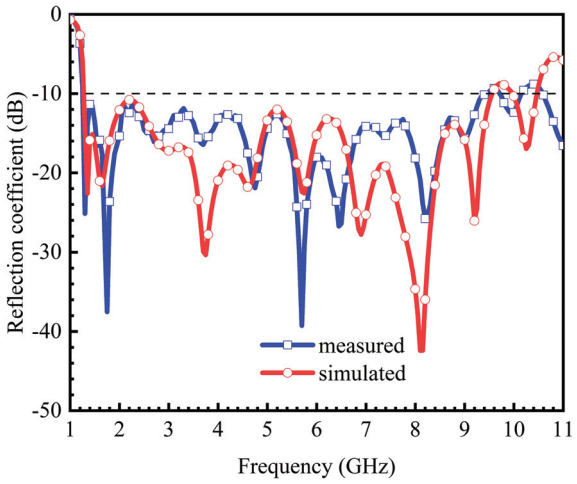

Fig. 10. Simulated and measured reflection coefficients.

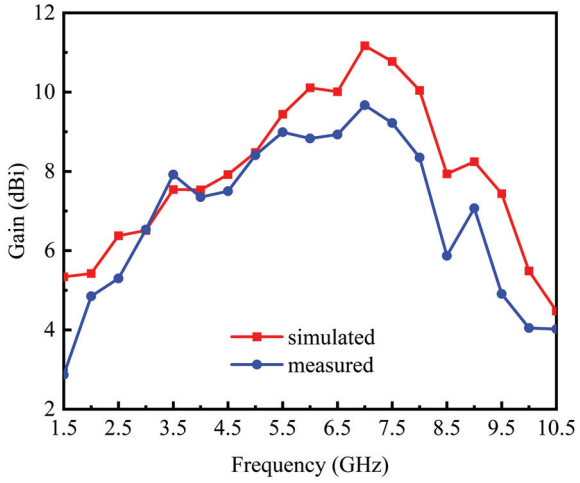

Fig. 11. Simulated and measured gain.

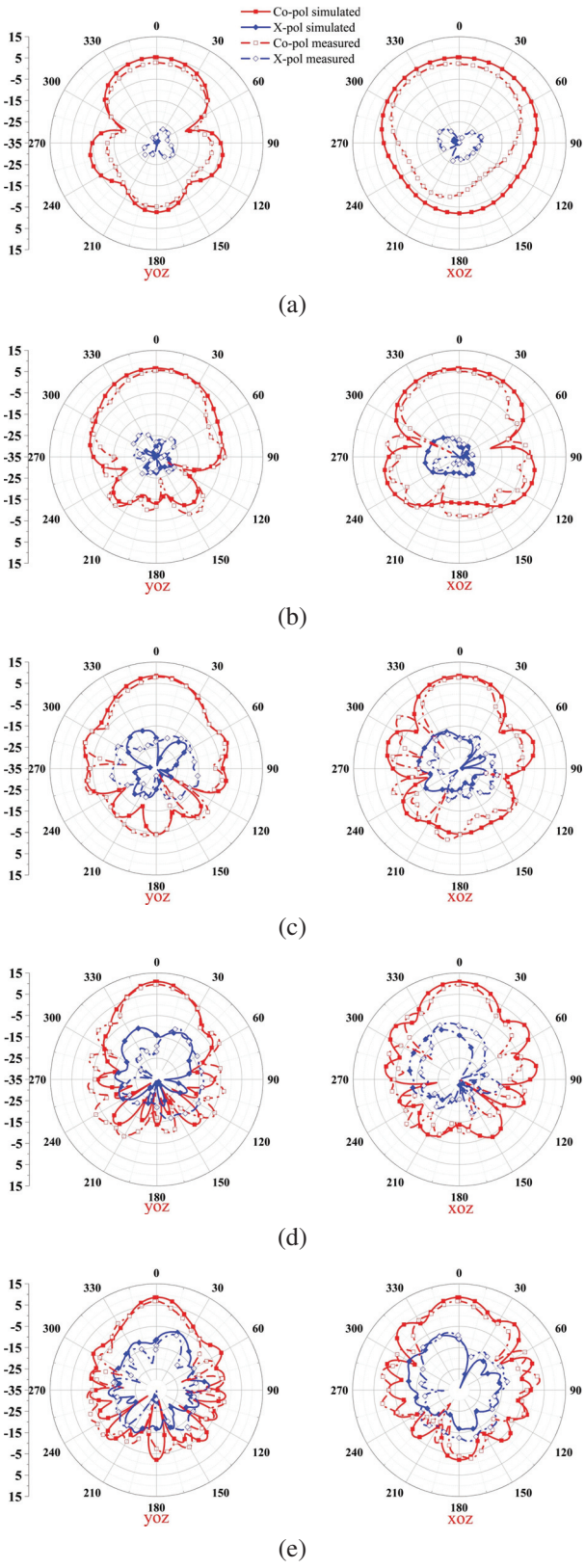

Fig. 12. Radiation pattern of *xoz* and *yoz* planes of the antenna at (a) 1.5 GHz, (b) 3 GHz, (c) 5 GHz, (d) 7 GHz, and (e) 9 GHz.

Table 2: Comparison of the proposed antenna with published literatures

Ref.	Size (λ_L^3)	BW (GHz)	RBW (%)	Gain (dBi)
[13]	0.7×0.67 ×0.0035	0.7-2.1	100	0.6-2
[15]	0.29×0.2 ×0.008	2.9-13.55	129.5	1.8-6.91
[18]	0.75×0.75 ×0.008	1.5-3.3	75	6.2-8.2
[19]	0.51×0.51 ×0.013	2.35-3.79	46.9	4-7.35
[21]	0.6×1.3 ×0.0025	1-28	186.2	4.9-14.4
Pro.	0.42×0.42 ×0.0042	1.27-9.4	152.4	3-9.67

λ_L is the free space wavelength at the lowest operational frequency.
RBW is the relative bandwidth.

directional radiation and linear polarization. The measured gain is higher than 3 dBi and peak gain reaches to 9.67 dBi in the working band. Table 2 shows comparison of the proposed antenna with published literatures. The proposed antenna has a wider bandwidth than the ones in [13, 15, 18, 19] and a smaller electrical size than the one in [21].

V. CONCLUSION

A miniaturized, high-gain, multi-band coverage ultra-wideband antenna has been proposed and fabricated in this article. The proposed antenna has an excellent impedance matching bandwidth of 1.27-9.4 GHz with reflection coefficient below −10 dB and stable directional radiation performance. The measured gain ranges from 3 dBi to 9.67 dBi. The overall size of the antenna is $0.42\lambda_L \times 0.42\lambda_L \times 0.0042\lambda_L$. The proposed antenna is a promising and economical candidate for applications such as detection radar, medical imaging, and mobile communication.

ACKNOWLEDGMENT

This work was supported by the Natural Science Foundation of Shandong Province, China (No. ZR2020MF023).

REFERENCES

[1] M. Shirazi, J. Huang, T. Li, and X. Gong, "A switchable S-/C-band antenna array with dual polarization and modularity," *IEEE Transactions on Antennas and Propagation*, vol. 68, no. 2, pp. 783-794, Feb. 2020.

[2] G. W. Yang and S. Zhang, "A dual-band shared-aperture antenna with wide-angle scanning

capability for mobile system applications," *IEEE Transactions on Vehicular Technology*, vol. 70, no. 5, pp. 4088-4097, May 2021.

[3] D. He, Y. Chen, and S. Yang, "A low-profile triple-band shared-aperture antenna array for 5G base station applications," *IEEE Transactions on Antennas and Propagation*, vol. 70, no. 4, pp. 2732-2739, Apr. 2022.

[4] Y. Li and Q. X. Chu, "Dual-band base station antenna array using the low-band antenna as parasitic decoupler," *IEEE Antennas and Wireless Propagation Letters*, vol. 21, no. 7, pp. 1308-1312, July 2022.

[5] P. J. Gibson, "The Vivaldi aerial," in *9th European Microwave Conference*, pp. 101-105, 1979.

[6] M. García-Fernández, G. Álvarez-Narciandi, Y. Álvarez López, and F. Las-Heras, "Array-based ground penetrating synthetic aperture radar on board an unmanned aerial vehicle for enhanced buried threats detection," *IEEE Transactions on Geoscience and Remote Sensing*, vol. 61, pp. 1-18, 2023.

[7] M. García Fernández, G. Álvarez Narciandi, A. Arboleya, C. Vázquez Antuña, F. L. H. Andrés, and Y. Álvarez López, "Development of an airborne-based GPR system for landmine and IED detection: antenna analysis and intercomparison," *IEEE Access*, vol. 9, pp. 127382-127396, Sep. 2021.

[8] H. H. Sun, W. Cheng, and Z. Fan, "Diameter estimation of cylindrical metal bar using wideband dual-polarized ground-penetrating radar," *IEEE Transactions on Instrumentation and Measurement*, vol. 72, pp. 1-14, 2023.

[9] P. Phasukkit, "Non-ionic deep learning-driven IR-UWB multiantenna scheme for breast tumor localization," *IEEE Access*, vol. 10, pp. 4536-4549, Jan. 2022.

[10] K. C. Santos, C. A. Fernandes, and J. R. Costa, "Validation of a compact microwave imaging system for bone fracture detection," *IEEE Access*, vol. 11, pp. 63690-63700, 2023.

[11] P. I. Bantavis, C. I. Kolitsidas, T. Empliouk, M. Le Roy, B. L. G. Jonsson, and G. A. Kyriacou, "A cost-effective wideband switched beam antenna system for a small cell base station," *IEEE Transactions on Antennas and Propagation*, vol. 66, no. 12, pp. 6851-6861, Dec. 2018.

[12] Y. Dong, J. Choi, and T. Itoh, "Vivaldi antenna with pattern diversity for 0.7 to 2.7 GHz cellular band applications," *IEEE Antennas and Wireless Propagation Letters*, vol. 17, no. 2, pp. 247-250, Feb. 2018.

[13] H. Cheng, H. Yang, Y. Li, and Y. Chen, "A compact Vivaldi antenna with artificial material lens and sidelobe suppressor for GPR applications," *IEEE Access*, vol. 8, pp. 64056-64063, Apr. 2020.

[14] M. Singh and M. S. Parihar, "Gain improvement of Vivaldi MIMO antenna with pattern diversity using bi-axial anisotropic metasurface for millimeter-wave band application," *IEEE Antennas and Wireless Propagation Letters*, vol. 22, no. 3, pp. 621-625, Mar. 2023.

[15] S. Saleh, W. Ismail, I. S. Zainal Abidin, M. H. Jamaluddin, M. H. Bataineh, and A. S. Al-Zoubi, "Novel compact UWB Vivaldi nonuniform slot antenna with enhanced bandwidth," *IEEE Transactions on Antennas and Propagation*, vol. 70, no. 8, pp. 6592-6603, Aug. 2022.

[16] M. Wang, L. Crocco, S. Costanzo, R. Scapaticci, and M. Cavagnaro, "A compact slot-loaded antipodal Vivaldi antenna for a microwave imaging system to monitor liver microwave thermal ablation," *IEEE Open Journal of Antennas and Propagation*, vol. 3, pp. 700-708, July 2022.

[17] M. Y. Ren, Z. W. Cheng, L. H. Wu, H. M. Zhang, S. X. Zhang, X. Y. Chen, D. Xing, and H. Qin, "Portable microwave-acoustic coaxial thermoacoustic probe with miniaturized Vivaldi antennas for breast tumor screening," *IEEE Transactions on Biomedical Engineering*, vol. 70, no. 1, pp. 175-181, Jan. 2023.

[18] A. M. de Oliveira, A. M. de Oliveira Neto, M. B. Perotoni, N. Nurhayati, H. Baudrand, A. de Carvalho, Jr, and J. F. Justo, "A fern antipodal Vivaldi antenna for near-field microwave imaging medical applications," *IEEE Transactions on Antennas and Propagation*, vol. 69, no. 12, pp. 8816-8829, Dec. 2021.

[19] M. Y. I. Yazid, M. H. Baharuddin, M. S. Islam, M. T. Islam, and A. F. Almutairi, "A Sierpinski arrowhead curve slot Vivaldi antenna for microwave head imaging system," *IEEE Access*, vol. 11, pp. 32335-32347, Apr. 2023.

[20] O. Yesilyurt and G. Turhan-Sayan, "Metasurface lens for ultra-wideband planar antenna," *IEEE Transactions on Antennas and Propagation*, vol. 68, no. 2, pp. 719-726, Feb. 2020.

[21] X. Shi, Y. Cao, Y. Hu, X. Luo, H. Yang, and L. H. Ye, "A high-gain antipodal Vivaldi antenna with director and metamaterial at 1-28 GHz," *IEEE Antennas and Wireless Propagation Letters*, vol. 20, no. 12, pp. 2432-2436, Dec. 2021.

[22] B. Tariq, M. Amjad, and A. Aziz, "Computational analysis for miniaturization of tapered slot antenna using elliptical conducting loaded strips," *Applied Computational Electromagnetics Society Journal*, vol. 37, no. 6, pp. 672-678, June 2022.

[23] N. Kwon, S. Ahn, and W. Lee, "Wideband printed antipodal Vivaldi antenna using straight slots for UHF DVB-T/T2 applications," *The Applied Computational Electromagnetics Society Journal*, vol. 37, no. 6, pp. 726-732, June 2022.

[24] H. T. Chou and Y. J. Lin, "An optimum design of paired balanced antipodal Vivaldi antennas with mirror-imaged symmetric architectures for ultra-broadband characteristics from microwave to millimeter-wave frequency ranges," *IEEE Access*, vol. 10, pp. 99516-99524, Sep. 2022.

[25] R. Cicchetti, V. Cicchetti, A. Faraone, and O. Testa, "A class of lightweight spherical-axicon dielectric lenses for high gain wideband antennas," *IEEE Access*, vol. 9, pp. 151873-151887, Oct. 2021.

[26] R. Cicchetti, V. Cicchetti, A. Faraone, L. Foged, and O. Testa, "A compact high-gain wideband lens Vivaldi antenna for wireless communications and through-the-wall imaging," *IEEE Transactions on Antennas and Propagation*, vol. 69, no. 6, pp. 3177-3192, June 2021.

[27] B. Wu, X. Y. Sun, H. R. Zu, H. H. Zhang, and T. Su, "Transparent ultrawideband halved coplanar Vivaldi antenna with metal mesh film," *IEEE Antennas and Wireless Propagation Letters*, vol. 21, no. 12, pp. 2532-2536, Dec. 2022.

[28] S. Y. Luo, Y. S. Li, and W. L. Shi, "A dual-frequency antenna array with mutual coupling reduction via metamaterial structures," in *2018 IEEE International Symposium on Antennas and Propagation & USNC/URSI National Radio Science Meeting*, pp. 1385-1386, 2018.

[29] K. Yu, Y. S. Li, and X. G. Liu, "Mutual coupling reduction of a MIMO antenna array using 3-D novel meta-material structures," *Applied Computational Electromagnetics Society Journal*, vol. 33, no. 7, pp. 758-763, July 2018.

[30] S. Y. Luo, Y. S. Li, Y. F. Xia, G. H. Yang, L. J. Sun, and L. Zhao, "Mutual coupling reduction of a dual-band antenna array using dual-frequency metamaterial structure," *Applied Computational Electromagnetics Society Journal*, vol. 34, no. 3, pp. 403-410, 2019.

[31] F. Liu, J. Y. Guo, L. Y. Zhao, G. L. Huang, Y. S. Li, and Y. Z. Yin, "Ceramic superstrate-based decoupling method for two closely packed antennas with cross-polarization suppression," *IEEE Transactions on Antennas and Propagation*, vol. 69, no. 3, pp. 1751-1756, Mar. 2021.

[32] J. Y. Guo, F. Liu, L. Y. Zhao, Y. Z. Yin, G. L. Huang, and Y. S. Li, "Meta-surface antenna array decoupling designs for two linear polarized antennas coupled in H-plane and E-plane," *IEEE Access*, vol. 7, pp. 100442-100452, Aug. 2019.

[33] M. Chiappe and G. L. Gragnani, "Theoretical and numerical analysis of the self-scaling properties of the exponentially tapered slot-line antenna," *Microwave and Optical Technology Letters*, vol. 45, no. 6, pp. 485-491, June 2005.

[34] D. R. Smith, D. C. Vier, T. Koschny, and C. M. Soukoulis, "Electromagnetic parameter retrieval from inhomogeneous metamaterials," *Phys. Rev. E*, vol. 71, no. 3, pp. 1-11, Mar. 2005.

Kun Li was born in Yichun, Jiangxi Province, China, in 1997. In 2020, he received the B.S. degree in communication engineering from Hunan Institute of Science and Technology, Yueyang, Hunan Province, China. He is currently pursuing the M.S. degree in new-generation electronic information technology at Qingdao University, Qingdao, China. His current research interest is in broadband high gain antenna and antenna array.

Zijie Li received the B.S. degree in Electromagnetic Field and Wireless Technology from the Nanjing University of Posts and Telecommunications, Nanjing, China, in 2021. He is currently pursuing the M.S. degree with the school of electronic information, Qingdao University, Qingdao, China. His current research interests include circularly polarized antennas, metamaterial-based antennas, and reconfigurable antennas.

Xiaorui Liu received the Ph.D. degree from Ocean University of China, Qingdao, Shandong Province, China, in 2019. From September 2017 to December 2018, he was a joint Ph.D. student at the Electromagnetic Compatibility Center of Missouri University of Technology. Since 2019, he joined Qingdao University, Qingdao, Shandong Province, China as an assistant professor. His research interests include robot-human-computer interaction, electronic information and detection technology, and embedded systems.

Shandong Li was born in Dongying, Shandong Province, China, in 1970. He received the B.S. from Shandong University, M.S. degree from Institute of Metal Research of the Chinese Academy of Sciences, and the Ph.D. degree from Nanjing University. He then pursued postdoctoral research in physical electronics at Nanjing University and Tsinghua University in Taiwan. He has been a visiting scholar at Northeastern University in the United States and Tübingen University and Münster University in Germany. He taught at China University of Petroleum (1996-2000) and Fujian Normal University (2004-2011). Now he is a Distinguished Professor and doctoral supervisor at Qingdao University. His research interests include superconducting quantum interference devices, magnetic materials, microwave materials and integrated devices, biochip technology, and new energy materials.

Xiaoyun Qu was born in Yantai City, Shandong Province, China, in 1974. She received the B.S. in applied mathematics from Yantai University, in 1996, and M.S. degree in electromagnetic fields and microwave technology from Nanjing Electronics research Center, Nanjing, Jiangsu Province, China, in 1990. She is with Shandong Institute of Space Electronic Technology, Yantai, China, as a Senior Engineer. Her research interest is antenna design.

Zhiqun Yang received the Ph.D. degree in communication and information system from Nanjing University of Technology, Nanjing, Jiangsu Province, China, in 2003. He is with Shandong Institute of Space Electronic Technology, China Aerospace Science and Technology Corporation, Yantai, China, as a Senior Engineer. His research interest is signal processing and communication.

Wei-hua Zong was born in Penglai City, Shandong Province, China, in 1975. She received the B.S. in applied mathematics from Yantai University, in 1997, M.S. degree in electromagnetic fields and microwave technology from Nanjing Electronics research Center, Nanjing, Jiangsu Province, China, in 2000, and the Ph.D. degree in electromagnetic fields and microwave technology from Xidian University, Xian, Shanxi Province, China, in 2004. In 2004, she joined Qingdao University, Qingdao, Shandong Province, China as a lecture. Since 2005, she has been an Associate Professor in Qingdao University. From February to August 2010, she was a Visiting Scholar Assistant with Electrical and Computation Engineering Department, National University of Singapore. Her research interests include antenna design and electromagnetic material measurement.

Architecture and Validation of Wideband Simultaneous Transmit and Receive Phased Array System

Jie Zhang, Hongchao Wu, and Lianqing Yu

Nanjing Research Institute of Electronic Technology
Nanjing 210039, China
zjwj2011@sina.com, babaywind@sina.com, ylqnj@163.com

Abstract **–** Because signals of different frequencies exhibit different characteristics after channel coupling, the traditional phased array system only uses phase shifter or antenna beam control to process frames plus amplitude adjustment control, which has the problem of optimizing the parameters of different frequencies to offset the mismatch. Based on the principle of broadband adaptive beamforming, each channel is configured as an adaptive filter with multiple taps to satisfy the precise relationship between interference suppression and frequency. On this basis, combined with the simultaneous application of a multi-element array system, a multi-tap weight optimization method for interference suppression is proposed. At the same time, in order to satisfy the application requirements of the existing phased array system architecture with only one set of controllable and adjustable weights, an adaptive beamforming weight optimization method for phased array system for wideband signals is analyzed and proposed on the basis of simulation analysis and research on the electromagnetic characteristics of the coupled self-interference channel. Through electromagnetic simulation evaluation and principle test verification, a set of weights corresponding to the center frequency of the wideband signal can be used to achieve interference suppression greater than 114 dB in the active transmission domain.

Index Terms **–** Phased array, self-interference suppression, simultaneous transmit and receive, wideband signal.

I. INTRODUCTION

Radio systems, including radar, communication, and various electronic warfare support measures, mainly use half-duplex (HD) mode with transmit and receive functions. In order to effectively utilize time, frequency, and spatial resources, with the development of radio hardware systems, especially adaptive signal processing, innovative full-duplex (FD) methods have been proposed to compensate for the shortcomings of HD. Although FD can bring many benefits, a serious problem in its practical implementation is that the transmitter and receiver will generate strong self-interference when operating simultaneously, which will cause serious interference to the receiver and prevent it from receiving stimulating signals from remote transmissions or returning weak signals [1].

The goal of FD technology is to simultaneously transmit and receive at the same frequency band at the same time. In this case, the radio frequency system not only receives the signal of interest, but also receives the transmitted coupling or leakage signal, which becomes the basic problem of simultaneous transmission and reception in radio systems. Therefore, the self-interference signal strength at the receiving end must be sufficiently reduced to ensure that the transmission of the radio system itself will not interfere with its normal reception of the signal of interest. Especially for phased array systems with multiple transceiver units, the self-interference component and amplitude will be significantly higher than traditional radio frequency systems [2, 3].

For the rate improvement problem of communication wireless networks, Chen et al. studied the comprehensive optimization of FD and transmit (Tx) and receive (Rx) phased arrays under the conditions of minimizing beam gain loss and maximizing rate gain [4]. In addition, for broadband interference suppression, Chen et al. used frequency domain equalization (FDE) technology to design and implement a radio frequency canceller with integrated circuit. Venkatakrishnan et al. proposed a four-level array self-interference cancellation including cross-polarization, especially in the 500 MHz range, and achieved an average 25 dB RF cancellation by using a multi-tap filter [5]. Kolodziej et al. proposed an RF canceller architecture with multiple non-uniform pre-weighted taps to improve system isolation by eliminating direct antenna coupling and multipath effects including typical interfering channels [6]. Adaniya studied the problem of wideband interference cancellation, and tested and compared the

Submitted On: November 30, 2023
Accepted On: July 22, 2024

https://doi.org/10.13052/2024.ACES.J.391006

performance and computational complexity of several methods [7].

Through a comprehensive analysis of relevant literature, we can see that, different from the conventional self-interference elimination of single-carrier frequency or narrowband signals, the elimination of wideband self-interference signals requires more degrees of freedom in multi-domain dimensions such as transmission domain and digital domain. Based on previous research work [8], this paper analyzes the transmission domain coupling coefficient characteristics of wide-width self-interference signals. A transmission domain interference suppression model, optimization method and approximate processing method for wideband signal are proposed, and the effect of multi-domain cascade self-interference elimination is evaluated by principle examination.

This paper is structured as follows. Section II introduces the array coupling self-interference cancellation model for wideband signal. The electromagnetic modeling simulation and experimental verification for wideband signal is given in sections III and IV. Section V summarizes the paper and prospects the future work.

II. ANALYSIS OF COUPLING SELF-INTERFERENCE CHARACTERISTICS OF WIDEBAND PHASED ARRAY

According to previous research work [8, 9], the self-interference channel characteristics $[\mathbf{H}(f)]_{M\times N}$ directly determine the complexity of coupled self-interference and the feasibility of suppression methods. Due to the complex three-dimensional structure of the actual array antenna, the simple near-field model is not strict and accurate to characterize the coupling interference of the array system. In order to better simulate the channel characteristics of the coupling interference between the transmitting unit and the receiving unit in the experimental array, we introduce an array electromagnetic model based on Ansoft HFSS (high-frequency structure simulator). HFSS uses the finite element method to calculate the S-parameter matrix $\mathbf{S}_f$ and the full-wave electromagnetic field of any array antenna configuration.

The p-th row and q-th column of the $\mathbf{S}_f$ matrix are represented as $\mathbf{S}_f(p,q)$, $(p,q=1,2,\ldots,P)$, which represents the coupling relationship between the p-th and q-th elements in the array. P is the total number of elements in the array. Based on the S-parameter matrix $\mathbf{S}_f$, we define the element $\mathbf{H}(m,n,f)$ the of the array in m-th row and in the n-th column of the interference channel characteristic matrix $[\mathbf{H}]_{M\times N}$, as:

$$\mathrm{H}(m,n,f)=\sum_{q_n\in T_n}\mathrm{S}_f(m,q_n)$$
$$(n=1,2,\ldots,N;\ m=1,2,\ldots,M) \quad (1)$$

where q_n is the unit number of the sub-array set for transmitting and/or receiving in the entire array, T_n is the unit set corresponding to the transmitting sub-array, N is the number of units of the transmitting sub-array, and M is the number of units of the receiving sub-array. Based on the self-interference coupling model proposed above, we first construct an electromagnetic model and a digital model for the practical array system, conduct design simulation verification through digital methods, and use it for subsequent principle experiment verification and evaluation. In this work, we take the 30(T)×10(R) array antenna as the example, and study the interference characteristics of two modes, i.e. the separate and the same aperture for transmission and reception.

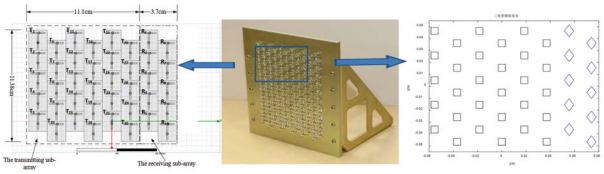

(a) (b) (c)

Fig. 1. Illustrative model and physical array antenna used for interference characteristics analysis: (a) HFSS EM model of the used array antenna (T: Transmitting element, R: Receiving element), (b) practical testing array antenna, and (c) digital model of the array antenna (T: Transmitting element, R: Receiving element).

When the separate sub-aperture transmission and reception work simultaneously, the transmission sub-array can be transmitted according to a certain beam-shaping weights, and the receiving sub-array can be simultaneously received according to a certain receiving beam-shaping weights. The arrangement of the phased array antenna in this mode is shown in Fig. 1, and the power of each transmitting component is set to 30 dBm, which can be controlled by the joint weights of amplitude and/or phase. By analyzing the self-interference coupling coefficients characteristics of the 30(T)×10(R) array antenna as shown in Fig. 1, the simulation coupling power at the receiving array elements can be obtained as shown in Fig. 2.

On the basis of the above analysis of the coupling characteristics of the phased array transmission and reception at a single frequency, in order to evaluate the feasibility of applying wideband signals in the simultaneous transmission and reception of the phased array system, we analyzed the antenna array at different frequencies. The electromagnetic coupling model of 12 GHz, 11 GHz, 10.4 GHz, 10.2 GHz, 10 GHz, 9.8 GHz, 9.6 GHz, 9 GHz, 8 GHz and other different frequencies are studied. The interference characteristics of array coupling are shown in Fig. 3.

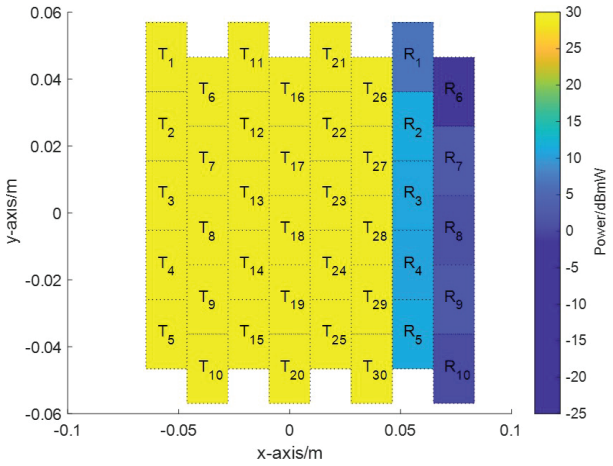

Fig. 2. Distribution characteristics of the coupling self-interference power for simultaneous transmission and reception with the separate sub-apertures array antenna.

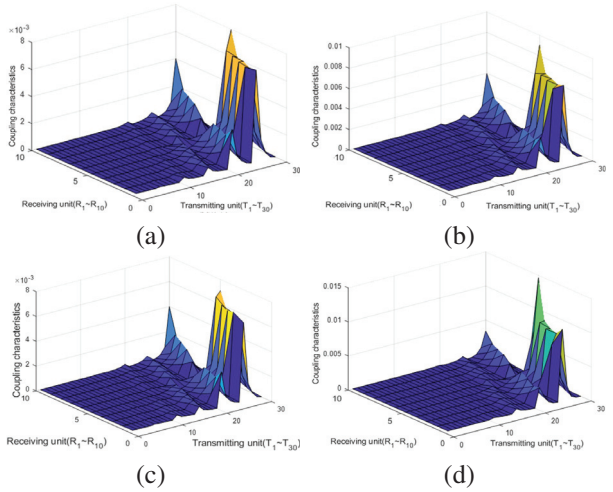

Fig. 3. Simulation results of coupling interference characteristics of array antenna at different frequencies: (a) 10 GHz, (b) 9.8 GHz, (c) 10.2 GHz, (d) 9 GHz, and (e) 8 GHz.

From the above analysis and comparison, it can be seen that the coupling interference characteristics of phased array systems at different frequencies are different. In the coupling interference suppression optimization model proposed by us, the optimization method based on single frequency coupling characteristics is not strict. To this end, we further propose the precise beam control of wideband signals by configuring each channel as an adaptive filter with multiple taps. The cancellation performance is analyzed by simulating a set of weight coefficients corresponding to a single frequency coupling feature on a certain bandwidth basis, as shown in Fig. 4. In the phased array system architecture, the approximate

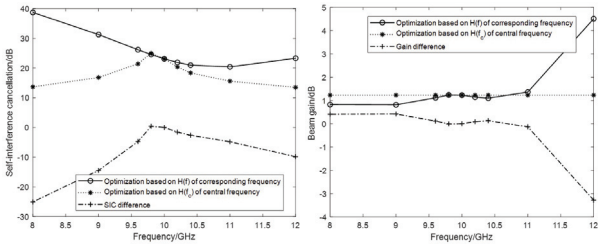

Fig. 4. Variation of (a) self-interference cancellation performance and (b) beam gain performance for different frequencies based on the central frequency coupling characteristics.

optimal suppression of wideband coupled interference signals is realized.

III. PHASED ARRAY SELF-INTERFERENCE COUPLING MODEL OF WIDEBAND SIGNAL

As described above, the self-interference suppression method of the phased array system forms a null zero point at the position of the receiving/transmitting unit by adjusting the transmitting/receiving beamforming weights. In the case of conventional single-point frequency signal applications, each transmitting/receiving unit of the array antenna has only two adjustable quantities of amplitude and phase, and single-point frequency or narrowband signals can use the above methods. However, for broadband signals, signals with different frequency components have different responses to fixed phase shifts or delays, and beamforming of the array will have certain difficulties. For this reason, a wideband signal beamforming optimization model and method is proposed, that is, a multi-tap adaptive filter is used on each channel to solve the problem of broadband signal application. This method has the same principles of transmission and reception. Figure 5 shows an example of broadband signal transmission.

For the coupling interference suppression at a receiving unit position, take the coupling interference suppression of the m-th receiving unit with N transmitters as an example, and the following method is adopted.

For broadband signal applications, each transmitter corresponds to an adaptive filter, and its weight $\mathbf{w}_n = [w_{n,1}, w_{n,2}, \ldots, w_{n,J}]$ acts on the reference input $x(k)$, $(n = 1, 2, \ldots, N)$ represents N transmitters, and J is the number of filter taps. Under the phased array antenna system, the reference input is the same for all transmitters, and the weight of each transmitter adopts different values through optimization and shaping. In any system that uses a transmit filter, the transmit signal from the n-th transmitter is:

$$t_n(k) = \mathbf{w}_n \otimes x(k), \tag{2}$$

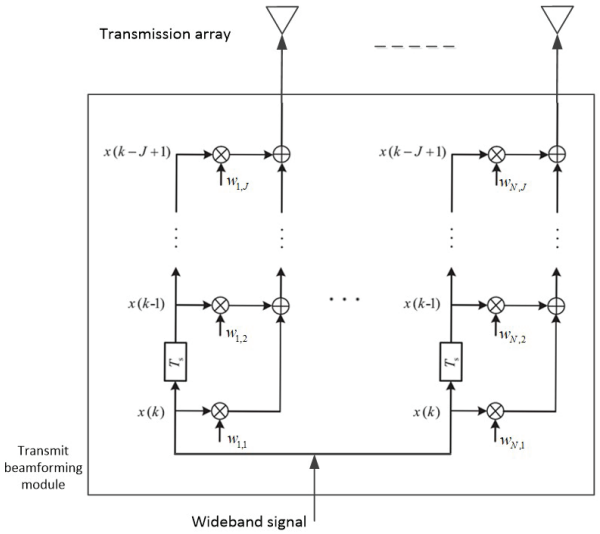

Fig. 5. Schematic diagram of broadband signal beamforming principle of phased array antenna.

where $\otimes$ means convolution. The transmitted signal reaches the receiving unit through coupling transmission, during which it may go through the propagation process of different paths such as reflection, diffraction, and scattering. The entire sets of gain and delay caused by these effects are set as the transfer function vector $[\mathbf{h}_{m,n}]_{C\times 1}$ from the transmitter to the receiver. Among them, the subscripts n and m represent the channel characteristics from the n-th transmitting unit to the m-th receiving unit, and C represents the order of the coupling interference channel. In a system with N transmitting units, the signal $y_m(k)$ at the m-th receiving unit is expressed as:

$$y_m(k) = \sum_{n=1}^{N} \mathbf{h}_{m,n} \otimes \mathbf{w}_n \otimes x(k). \tag{3}$$

Considering the K-bit input signal, the above relation is expressed as a vector:

$$\mathbf{y}_m = \sum_{n=1}^{N} \mathbf{h}_{m,n} \otimes \mathbf{w}_n \otimes \mathbf{x}. \tag{4}$$

The above-mentioned convolution relationship is expressed by matrix multiplication as:

$$\mathbf{y}_m = \mathbf{A}_m \mathbf{W}_m, \tag{5}$$

where $\mathbf{W}m$ is the vector of all weight values of N transmitters to the m-th receiving unit, $\mathbf{A}_m$ is derived from $x=[x(1),x(2),\ldots,x(K)]^T$, and $h_{m,n}$. The two matrices are expressed as:

$$\mathbf{W}_m = \underbrace{\left[w_{1,1} \ \ldots \ w_{1,J} \ \cdots \ w_{N,1} \ \cdots w_{N,J} \right]^T}_{(NJ\times 1)}, \tag{6}$$

$$\mathbf{A}_m = \underbrace{\left[\text{Hankel}\left(\text{Hankel}(\mathbf{x})\mathbf{h}_{m,1}\right) : \cdots \ : \text{Hankel}\left(\text{Hankel}(\mathbf{x})\mathbf{h}_{m,N}\right)\right]}_{((K+C+J-2)\times NJ)}, \tag{7}$$

where Hankel$(\mathbf{x})$ represents the Hankel matrix composed of vector $\mathbf{x}$:

$$\text{Hankel}(\mathbf{x}) = \begin{bmatrix} x[1] & & \cdots & 0 & 0 \\ x[2] & x[1] & & 0 & 0 \\ \vdots & \vdots & & \vdots & \vdots \\ x[C] & x[C-1] & \cdots & x[2] & x[1] \\ \vdots & \vdots & & \vdots & \vdots \\ x[K] & x[K-1] & \cdots & x[K-C+2] & x[K-C+1] \\ \vdots & \vdots & & \vdots & \vdots \\ 0 & 0 & & x[K] & x[K-1] \\ 0 & 0 & \cdots & 0 & x[K] \end{bmatrix}_{(K+C-1)\times C} \tag{8}$$

Based on the matrix product representation of the received signal, the received signal power is:

$$p_{y_m} = \frac{1}{K} \mathbf{W}_m^H \mathbf{A}_m^H \mathbf{A}_m \mathbf{W}_m. \tag{9}$$

In order to ensure that the output power remains constant while the transmit array weights are optimized, without loss of generality, the constraint condition of the weights is set to $\mathbf{W}_m^H \mathbf{W}_m = 1$, then the optimization model is:

$$\arg\min_{\mathbf{W}_m} \left(p_{y_m} = \frac{1}{K} \mathbf{W}_m^H \mathbf{A}_m^H \mathbf{A}_m \mathbf{W}_m \right). \quad \text{s.t.} \ \left\{ \mathbf{W}_m^H \mathbf{W}_m = 1 \right. \tag{10}$$

Inspired by the concept of Rayleigh quotient, the optimal weight vector $\mathbf{W}_{m,opt}$ is the eigenvector corresponding to the smallest eigenvalue of $\mathbf{W}_m^H \mathbf{W}_m$. Set $\mathbf{B}_m = \mathbf{A}_m^H \mathbf{A}_m$, according to the concept of Rayleigh quotient, $\mathbf{min}\, R(\mathbf{B}_m, \mathbf{W}_m) = \lambda_{\mathbf{min}}(\mathrm{B}_m)$, where $\lambda_{\min}(\mathbf{B}_m)$ is the minimum eigenvalue of $\mathbf{B}_m$, and the optimal weight vector $\mathbf{W}_{m,opt}$ is the eigenvector corresponding to the minimum eigenvalue of $\mathbf{B}_m$.

IV. PRINCIPLE EXPERIMENT AND TEST EVALUATION

On the basis of the previous work [8, 9], in order to evaluate the performance of the wideband self-interference suppression method, we use an experimental array antenna consisting of 30 transmitting units and 10 receiving units. Passive spatial attenuation in transmission domain and RF domain is combined with active adaptive beamforming, and adaptive recognition filter cancellation method is adopted in digital domain. The test signal is a wideband linear FM wave signal. The transmitted signal of the array antenna is recorded as the reference signal to suppress interference, and the

received signal of the receiving unit is recorded as the interference signal to be cancelled. The architecture and schematic diagram of the experimental system are shown in Fig. 6.

In our staged proof-of-principle experiment, for wideband signals with an instantaneous bandwidth of 50 MHz, the corresponding comprehensive interference suppression is about 29.4 dB, 40.9 dB and 114.5 dB after passive spatial transmission interference suppression, active beamforming optimization interference suppression and digital domain adaptive identification interference cancellation, as shown in Fig. 7.

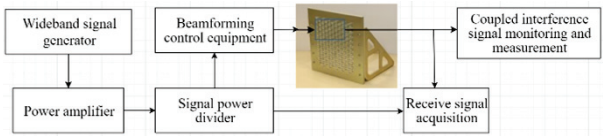

(a)

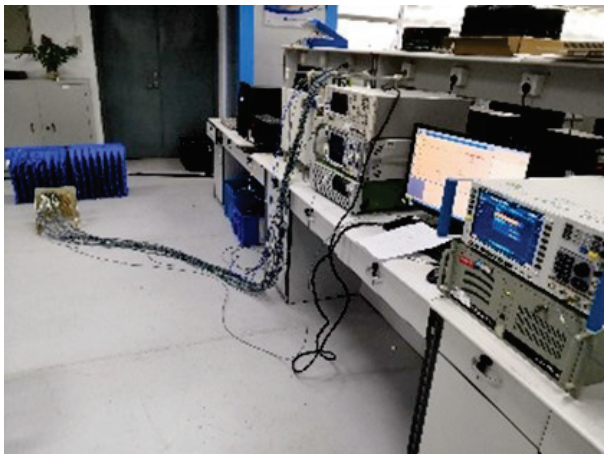

(b)

Fig. 6. (a) Block diagram of the principle experiment architecture and (b) schematic diagram of interference cancellation principle experiment scene.

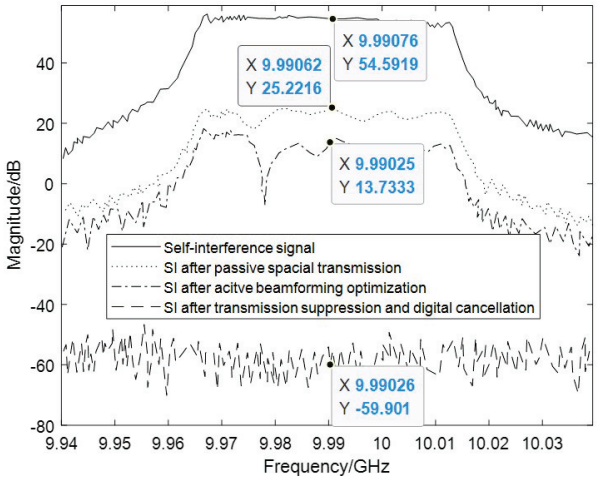

Fig. 7. Experimental results of wideband signal coupling self-interference multi-domain joint cancellation principle.

V. CONCLUSION

On the basis of electromagnetic modeling and digital modeling analysis of the coupling interference characteristics between phased array antenna elements when wideband signals are applied, this paper proposes a self-interference cancellation model and approximation method for wideband signals simultaneously. The cancellation method and its process are processed according to the transmission and coupling characteristics of the RF interference signal, and can be applied to the self-interference cancellation requirements of different frequency bands and different functions.

REFERENCES

[1] J. P. Doane, "Simultaneous transmit and receive with digital phased arrays," in *Proceedings of IEEE International Symposium on Phased Array Systems and Technology*, pp. 1-6, 2016.

[2] R. Chen, F. Li, J. Tang, X. Liu, J. Li, and X. Chen, "A diagnosis method for radio frequency channels of wireless devices without cable connections," *IEEE Transactions on Antennas and Propagation*, Dec. 2023.

[3] Y. Wang, H. Pei, W. Sha, Y. Huang, and A. Kishk, "MIMO performance enhancement of MIMO arrays using PCS-based near-field optimization technique," *Science China: Information Sciences*, vol. 66, no. 6, June 2023.

[4] T. Chen, M. Baraani Dastjerdi, J. Zhou, H. Krishnaswamy, and G. Zussman, "Wideband full-duplex wireless via frequency-domain equalization: Design and experimentation," in *Proc. ACM MobiCom'19*, 2019.

[5] S. B. Venkatakrishnan, E. A. Alwan, and J. L. Volakis, "Wideband RF self-interference cancellation circuit for phased array simultaneous transmit and receive systems," *IEEE Access*, vol. 6, pp. 3425-3432, 2018.

[6] K. E. Kolodziej, J. G. McMichael, and B. T. Perry, "Multitap RF canceller for in-band full-duplex wireless communications," *IEEE Transactions on Wireless Communications*, vol. 15, no. 6, pp. 4321-4334, 2016.

[7] H. L. Adaniya, "Wideband active antenna cancellation," Master's thesis, Massachusetts Institute of Technology, 2008.

[8] J. Zhang and H. Wu, "Simultaneous transmit and receive phased array system architecture

and prototype comprehensive verification," *Applied Computational Electromagnetics Society (ACES) Journal*, vol. 37, no. 12, pp. 1257-1264, May 2023.

[9] J. Zhang and J. Zheng, "Prototype verification of self-interference suppression for constant-amplitude full-duplex phased array with finite phase shift," *Electronics*, vol. 11, no. 3, p. 295, 2022.

Jie Zhang received his Ph.D. degree from the School of Information Science and Engineering of Southeast University in 2006. He joined Nanjing Research Institute of Electronics Technology in 2006. His research interests include radar system technology, simultaneous transmitting and receiving, and radar waveform design.

Hongchao Wu received the B.E. and Ph.D. degrees in communication engineering from Southeast University, Nanjing, China, in 1999 and 2006, respectively. He joined Nanjing Research Institute of Electronic Technology in 2006. His research interests include solid-state active phased array antenna and digital array antenna.

Lianqing Yu is Senior engineer, mainly engaged in radar system design and information processing. In the past two years, he has mainly engaged in the design and research of Integrated Sensing and Communications (ISAC). He has also used centimeter wave 5G base stations for the first time in China to achieve detection and stable tracking of unmanned aerial vehicles, and has published more than 10 papers.

One-to-Multiple RF Power Transmission System Based on High-Gain Phased Array with Beam Control

Xue Bai, Yanjiao Hou, Leijun Xu, Jianfeng Chen, and Yiyang Kong

School of Electrical and Information Engineering
Jiangsu University, Zhenjiang 212013, China
baixue@ujs.edu.cn, 2212007003@stmail.ujs.edu.cn, xlking@ujs.edu.cn, 1000005767@ujs.edu.cn,
2212207077@stmail.ujs.edu.cn

***Abstract* –** This paper proposes a one-to-multiple RF wireless power transmission (WPT) system that uses multi-mode phased array technology to control beamforming. The proposed system uses array partition mode and time division mode to achieve multi-target WPT. A novel quasi-Yagi antenna with enhanced gain is designed, consisting of a pair of dipoles, three directors, and a single split-ring resonator (SSRR), which is then used to form a 1×8 array for power transmission. The antenna has a bandwidth of 0.35 GHz with a frequency range of 2.25-2.6 GHz and a gain of 9.38 dBi. The total gain of the 1×8 array antenna is 17.23 dBi. An 8-way power divider is designed and implemented to feed the power amplifier (PA) of each array element, with isolation greater than 20 dB and return loss less than −17 dB. A digital phase and attenuation control circuit is also designed to achieve beam control. Measurement results show that at a distance of 3 meters, the maximum received power for single-target and multi-target schemes is 7.5 dBm and −2.6 dBm at each node, respectively. The system's flexible beam control mode and high gain transmission characteristics can be used in scenarios such as wirelessly powering Internet of Things (IoT) multi-sensor networks.

***Index Terms* –** Antenna array, multi-target, phased array, quasi-Yagi antenna, single split ring resonator (SSRR), wireless power transmission (WPT).

I. INTRODUCTION

With the development of 5G mobile communication technology, we have entered a new era of the Internet of Everything, which consists of various low-power wireless devices. It is estimated that 75 billion Internet of Things (IoT) devices will be connected to the Internet by 2025 [1, 2], and most of them are wireless sensors. In the scenario of multi-sensor applications, wireless power transmission (WPT) has become an increasingly attractive way to provide power [3], especially for sensor detection systems in dust-free workshops, underwater quality detection sensor systems, and drone swarm systems where battery replacement is difficult [4–7]. To achieve WPT, energy can be transmitted by electromagnetic induction and RF. For the induction method, high power transmission can be achieved within several kW, but the effective working range is short and therefore the device to be charged has less mobility [8, 9]. In contrast, the working range of RF-based charging is quite long, but the low directivity of an omnidirectional system can result in significant energy losses [10]. A directional WPT system can be implemented using array and beamforming to overcome this problem. The emitted beam can then be focused and directed to the target, increasing the effective transmitted energy of the WPT system [11, 12]. Many studies have been conducted to improve the performance of RF array based WPTs. In literature [13], a retro-directional antenna array for WPT with a simple structure was proposed, but it has poor flexibility in beam steering. Compared to the work in [13], literature [14] uses a phased mode for beam steering, which provides more flexibility in steering and can work under the optimal beam shape for a given array arrangement, and a modular triangular array was used to suppress the presence of multiple main lobes. However, the work in [14] has only single-mode control and low antenna gain, which limits the application of this structure. In [15], a WPT system using a Fresnel lens was proposed, which has a focused beam and thus increased system gain, and the phase correction can be done by diffraction. However, a set of lenses has to be placed on top of the antennas, which takes up a considerable amount of space. Literature [16] uses air as a dielectric material to improve the gain of the antenna, an independent antenna without additional equipment. However, none of the above literature is applicable to the scenario where multiple targets need to be charged. Literature [17] proposed a MIMO WPT system that can power multiple targets, but it is carried out in the way of magnetic coupling resonance and the applicable distance is short, in the range of 5 cm.

Submitted On: October 8, 2023
Accepted On: August 20, 2024

https://doi.org/10.13052/2024.ACES.J.391007

In this paper, a multi-mode RF WPT system with time-division multiplexed array partitioning capability is proposed to support a flexible power scheme for both single-target and multi-target WPT applications. A new high-gain quasi-Yagi antenna is designed to form an antenna array. The system uses phase and magnitude control to perform beam steering, enabling one-to-one and one-to-many wireless charging nodes over relatively long distances.

II. THE POWER TRANSMISSION SCHEME

In order to deliver RF energy to multiple targets at relatively long distances, phased array control is essential as it provides the means to realize beam steering. By adjusting the phase and magnitude of the excitation at each port of the array elements, the main lobe with the focused energy can be directed to the targets [18].

A. Principle of phased array beamforming

Phased array and beamforming theory for antenna array shape is an essential part of the research. There are various forms of antenna array, which can be divided into linear array, rectangular array, triangular grid, hexagonal array and circular array. Linear arrays can be easily extended to other array layouts because of their simplicity. In energy transfer, the lobe width in the normal direction of a linear array is large and can scan a certain range of longitudinal areas. Therefore, the layout form of a linear array is adopted in this design.

Consider an array of identical radiating elements, numbered N, equally spaced along the x-axis by d, as shown in Fig. 1. Further, a triangular constant is defined between these elements in Fig. 2, with the distance between the elements denoted by d. The aiming line is the direction perpendicular to the array, the beam points in a direction angularly separated from the aiming line by θ, and the beam is angularly separated from the horizontal line of the antenna array by φ.

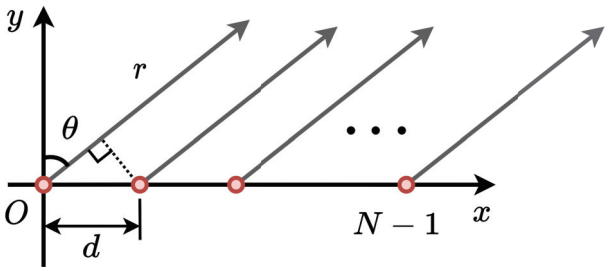

Fig. 1. Schematic diagram of linear array radiation.

Figure 2 shows that the sum of θ and φ is 90°. Thus we can calculate L according to d and θ, because $L = d\sin(\theta)$. L represents the variable distance of the wave propagation. The delay required for beam steering is equal to the time taken for the wavefront to traverse the distance L. If L is considered as a fraction of the wavelength, the phase delay can be replaced by this delay. The $\Delta\Phi$ equation can be defined as the formula for θ. According to Fig. 2, the following equations can be derived:

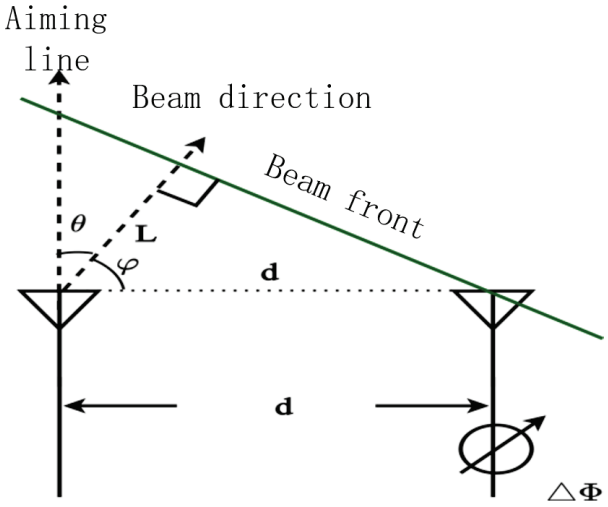

Fig. 2. Diagram of phase analysis between adjacent components.

$$\cos\varphi = \frac{L}{d}, \tag{1}$$

$$\Delta t = \frac{L}{c} = \frac{2\pi L}{\lambda} = \frac{2\pi \mathrm{d}\sin\theta}{\lambda}\ ,\ c = 3\times 10^8\ m/s, \tag{2}$$

$$\Delta\Phi = d\sin\theta = \frac{2\pi d\sin\theta}{\lambda}, \tag{3}$$

where λ is the wavelength of the received signal. Then the sum of the radiation field strength of the N array elements in the far region of the θ direction can be expressed as:

$$E(\theta) = \sum_{k=0}^{N-1} E_{\mathrm{k}} e^{jk\triangle\Phi} = E\sum_{k=0}^{N-1} e^{jk\triangle\Phi}, \tag{4}$$

where E_{k} is the radiation field strength of each element in the far field area, when E_{k} is the same element is equal to E, and the latter equation is established.

According to the summing formula and Euler formula, the above equation can be written as:

$$E(\theta) = E\frac{e^{jN\triangle\Phi}-1}{e^{j\triangle\Phi}-1} = E\frac{\sin(N\triangle\Phi/2)}{\sin(\triangle\Phi/2)}e^{j\frac{N-1}{2}\triangle\Phi}. \tag{5}$$

After taking the absolute value of the normalized isotropic element array $F_{\mathrm{a}}(\theta)$, the array factor is expressed as:

$$F_{\mathrm{a}}(\theta) = \frac{|E(\theta)|}{|E_{\max}(\theta)|} = \frac{\sin[\pi N(d/\lambda)\sin\theta]}{N\sin[\pi(d/\lambda)\sin\theta]}. \tag{6}$$

When each array is not nondirectional and the field strength map is $F_{\mathrm{e}}(\theta)$, the field strength map of the array

becomes equation (7), that is, the product theorem of the direction diagram of the array antenna:

$$F(\theta) = F_a(\theta)F_e(\theta). \quad (7)$$

$F_e(\theta)$ means that the unit factor is determined by the form and direction of the array element. It represents the radiation direction map of the array antenna and has nothing to do with the composition form of the antenna array. The array factor depends on the array arrangement, cell spacing, feed amplitude and phase, independent of the form and orientation of the array. Therefore, the array factor and the unit factor can independently determine the radiation performance of the antenna array, without interfering with each other. Because the antenna radiation surface size remains unchanged, the radiation performance of the array antenna is only related to the feed amplitude and phase.

B. Scheme

Depending on the number of targets to be powered, different transfer modes can be used. First, the subarray partitioning for the power transmission mode is discussed. Figure 3 (a) shows that an array of N antenna elements is divided into x parts, where x is the number of targets, and each subarray powers only its corresponding targets. In order to maintain beam steering capability and ensure a given receive power, the number of antenna arrays, N, should be greater than the number of targets, x. Based on the above strategy, one must increase the number of antennas of the WPT as the number of targets to be charged increases. This results in an increase in the size of the individual transmitters, which is unfavorable for the application. One way to alleviate this problem is to split the large array into several relatively small arrays, as shown in Fig. 3 (c). For example, in a large room with many sensors that need to be powered, place a transmitter array on each wall to power nearby sensors.

The other transmission mode that can solve the one-to-many WPT problem is time-division multiplexing using the entire antenna array. By exploiting the beam steering capability of the phased array, this mode can cyclically charge multiple targets within a time interval T, as shown in Fig. 3 (b). This strategy is recommended to minimize the size of the WPT array. However, a longer cycle time is required when multiple targets are present simultaneously. This results in a slower charge rate for each target. If the number of targets to be charged is too large, the charging time of each target will be slow and will not be able to keep up with its power consumption. From this point of view, the time-shared transmission mode cannot power too many targets at the same time. Therefore, in an extreme case, the multiple arrays approach is also applicable to the time-division strategy to overcome the above problem. As shown in Fig. 3 (d), the fixed charging interval for each charging node is T,

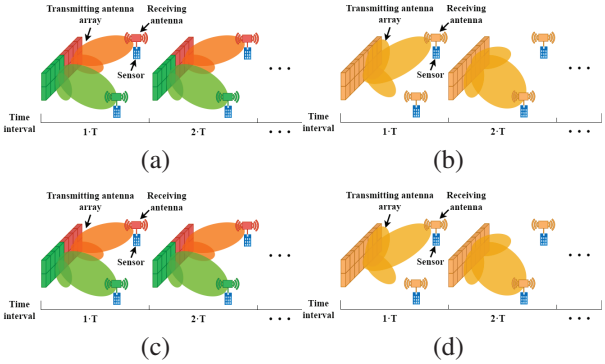

Fig. 3. (a, b) Diagram of two targets power transmission at array-partition and time-division transmission mode, (c,d) diagram of multiple targets power transmission at array-partition and time-division transmission mode, and (e) functional block diagram of the system.

and then each array charges the surrounding devices in turn.

To take full advantage of the benefits and minimize the drawbacks, it is advisable to combine the two transmission modes rationally. In the case of charging multiple targets, the power transmission of the whole array and the subarrays can be carried out in a hybrid of time-division and array-partitioning. The allocation of each mode depends on the relationship between the received energy, the appropriate number of targets, the distance between the target and the antenna, and the number of array antennas.

In order to verify the feasibility of the transmission method, a 1×8 energy transmission array has been built in this paper, with transmission energy at a frequency of 2.4 GHz. Two modes are used to test the energy transmission of multiple targets.

III. DESIGN OF THE SYSTEM

The functional block diagram of the proposed single-to-multiple RF WPT system is shown in Fig. 3 (e). A 2.4 GHz signal is generated by the RF signal source and then transmitted to each circuit through the power divider. After the computer sets the waveform, each channel's command is sent to the microcontroller unit (MCU). The MCU then controls the phase shift and attenuation of each channel. A two-stage RF power amplifier (PA) amplifies the RF signal after phase shifting. Each signal is amplified to 1 W and transmitted to free space via the antenna.

For verification purposes, we chose a 1 W RF PA to drive the antenna array, and the modular design makes it easy to replace different functional modules. The output power can be improved by simply replacing the PA with a higher PA.

A. Antenna design

The Friis formula for power transmission is:

$$P_r = P_t \frac{G_t G_r \lambda^2}{(4\pi R)^2}, \tag{8}$$

where Pt is the power of the transmitting antenna, Gt is the gain of the transmitting antenna, Gr is the gain of the receiving antenna, Pr is the received power, λ is the operating wavelength and R is the distance between the transmitting and receiving antennas.

The gain of the antenna is positively correlated with the received power. The formula shows that the gain of the antenna is also essential to improve the efficiency of the energy transfer. Theoretically, the antenna that forms the array is omnidirectional, which makes the beam of the entire array more concentrated and more powerful. Therefore, in order to improve the efficiency as much as possible and to satisfy the omnidirectional wave lobe of a single antenna, the high-gain quasi-Yagi antenna is selected as the transmitting antenna of this system. It is a terminal array antenna that has evolved from the dipole antenna but has a higher gain than the dipole antenna [19, 20].

Based on this, a high-gain 2.4 GHz directional quasi-Yagi antenna suitable for this system is designed. Each part of the planarized quasi-Yagi antenna is replaced by a microstrip structure. A substrate dielectric layer separates two layers of metal conductors. The upper metal conductor layer is used as an electromagnetic radiator and the lower metal conductor layer is used as ground. The more directors the quasi-Yagi antenna has, the higher its gain. In this system, considering the overall size and the fact that the gain changes little when the number of directors is more than four, four directors are selected.

The gain of the microstrip quasi-Yagi antenna is improved by the single split-ring resonator (SSRR), which acts as a special function of the pilot in front of the upper transmitting direction of the quasi-Yagi antenna. SSRR is a magnetic resonator consisting of a single open ring. Studies have found that it can be used to construct antennas and other microwave devices to obtain advantages such as high gain and good directivity [21].

The geometric structure of the improved antenna is shown in Fig. 4 (a). The high gain quasi-Yagi antenna based on SSRR can effectively reduce the return loss and improve the gain under the premise of ensuring the antenna size and bandwidth. Table 1 shows the parameters of the improved antenna with SSRR.

Replacing the fourth director with the SSRR results in a slight increase in gain. The antenna with SSRR reduces the size and increases the gain compared to the antenna with five feeders.

Table 1: Size parameters of the antenna (mm)

L_{sub}	W_{sub}	h	W_1
190	98	1.6	3.166
W_2	L_1	L_2	L_3
4.6	47.258	32.6	57
G_1	G_2	G_3	G_4
17.442	19.455	21.645	17.25
S_1	S_2	S_3	S_4
3	5	7	2.2
D_1	D_2	D_3	D_4
25.3	37.528	37.068	36.16
D_5	D_6	D_7	L_4
12.8	2.9	8	22.8

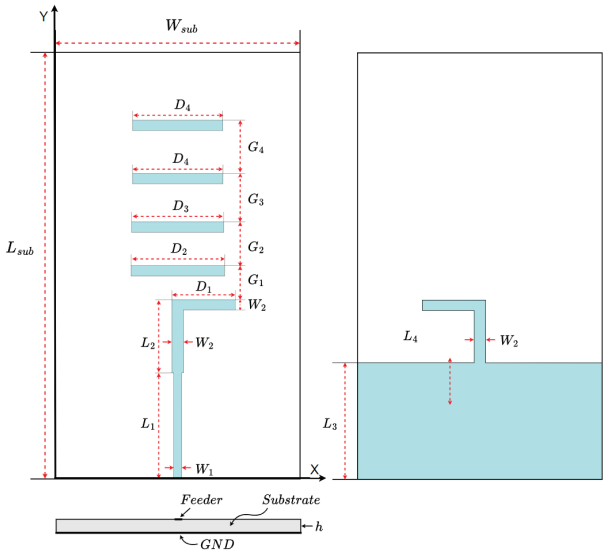

(a)

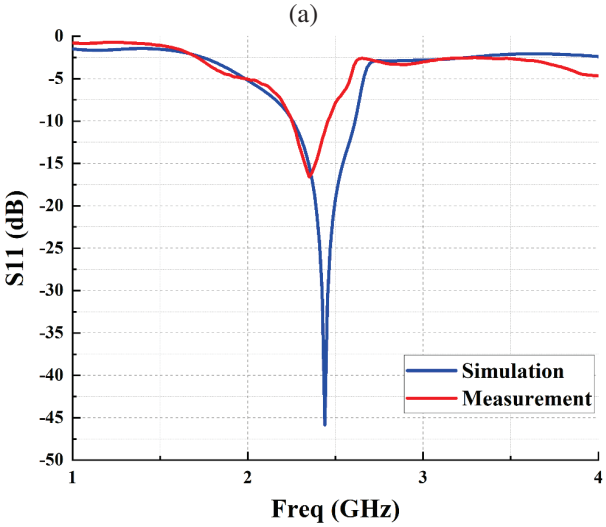

(b)

Fig. 4. *Continued.*

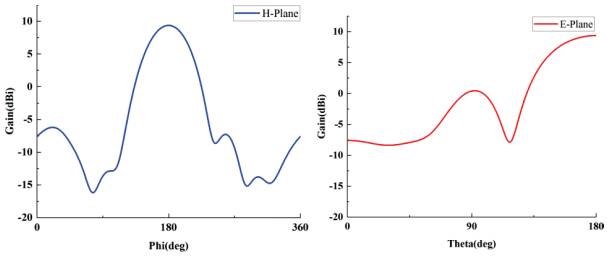

(c)

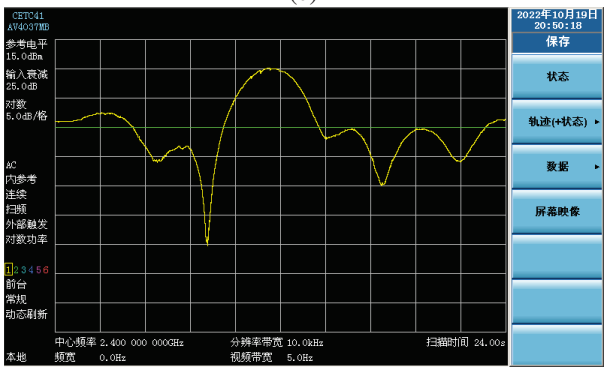

(d)

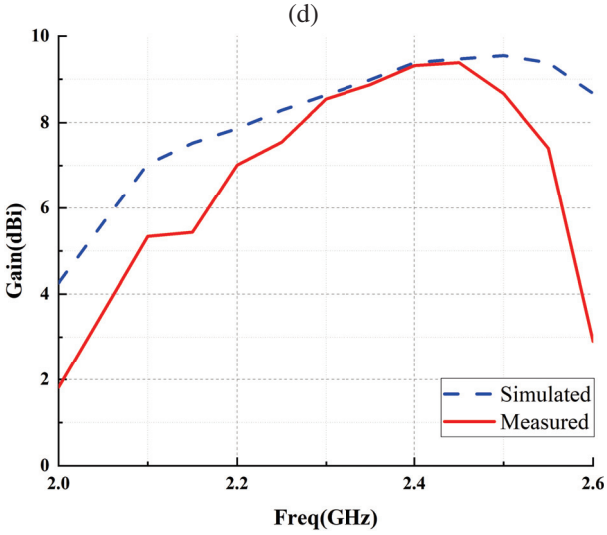

(e)

Fig. 4. (a) Improved quasi-Yagi antenna with SSRR, (b) simulated and measured S11 of antenna, (c) simulated radiation patterns of antenna at 2.4 GHz, (d) measured radiation patterns of antenna at 2.4 GHz, and (e) the simulated and measured gain of the antenna.

The designed antenna is measured using the AV3656B vector network analyzer. The simulated and measured return loss results are shown in Fig. 4 (b). The results show that the measured return loss has little change, and the resonant frequency is 2.39 GHz. Compared to the simulation results, the resonant frequency is shifted to a lower frequency. The measured bandwidth is 0.35 GHz. The shifted center frequency could be caused by the drifted dielectric constant and thickness of the core material of the PCB during the manufacturing process.

In addition, as shown in Fig. 4 (c), at 2.4 GHz, the radiation pattern radiates only to one end to reduce power loss, with a half-power beamwidth of 67°. The measured image is shown in Fig. 4 (d) and there is not much deviation from the simulated image. Therefore, this antenna can focus and transmit electromagnetic signals. The simulated and measured gain of the antenna is shown in Fig. 4 (e). The gain of the designed antenna is 9.38 dBi at 2.4 GHz.

B. Wilkinson power divider design

To feed the proposed antenna array, a 1×8 Wilkinson power divider with an equal power distribution ratio is designed and optimized using the Advanced Design System (ADS) software. Figure 5 (a) shows the prototype of the power divider based on FR4 substrate.

It can be seen that the proposed power divider starts with a 1×2 substructure, which can be constructed with a three-port network (T-branch). A transmission line width with a characteristic impedance Z0=50 ohms and a quarter wavelength line with 70.7 ohms at a center frequency of 2.4 GHz can be calculated using the LineCalc tool from ADS. After obtaining the above initial value, the required 1×8 Wilkinson power divider is obtained by cascading the 1×2 power dividers in ADS.

The measured results of the Wilkinson power divider are shown in Figs. 5 (b,c). Ideally, the Sn1 (n is the number of outputs) of a 1×8 Wilkinson power divider is 9 dB. The results of the proposed power divider are around 9.2 dB at the operating frequency, which meets the requirements of our design. In addition, S11 is less than −15 dB, the interport isolation is greater than 20 dB, and the phase difference of the output ports is less than 1.189°.

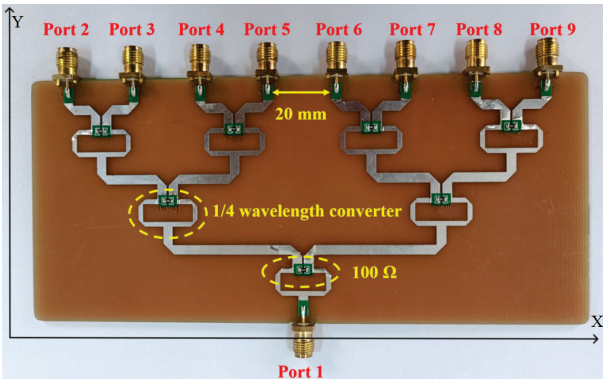

(a)

Fig. 5. *Continued.*

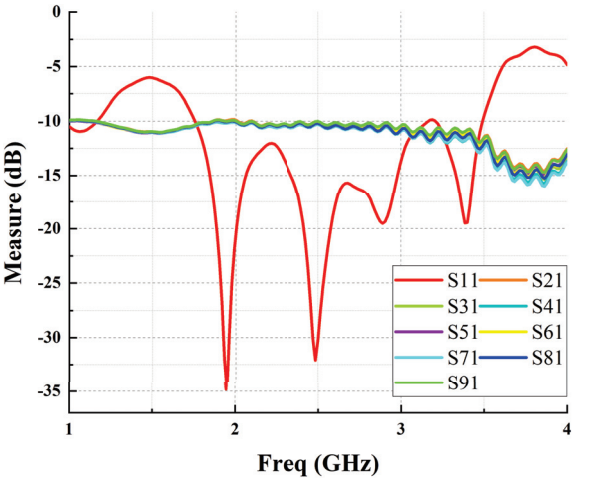

(b)

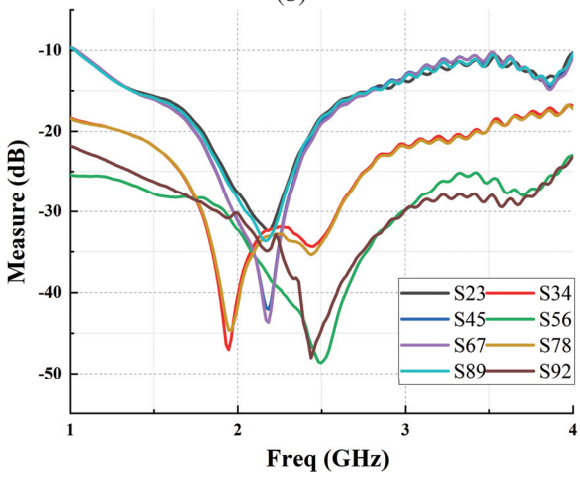

(c)

Fig. 5. (a) Physical diagram of 1×8 Wilkinson power divider, (b) measured output port insertion loss and S11, and (c) measured isolation of each port.

C. Phase shift and amplifier circuit design

The selected PE44820 is the digital phase shifter that can achieve control accuracy of 1.4° within 360° at 8-bit resolution. The RMSE of phase and amplitude is 1.0° and 0.1 dB, respectively, the frequency range is 1.1-3.0 GHz, and the input third-order intercept is +60 dBm with high linearity. In addition, the integrated digital control interface supports serial and parallel programming of the phase setting, which facilitates cascade design and meets the design requirements of the system.

The matching design using ADS matched all RF signal lines to 2.4 GHz and impedance matching to 50 Ω to minimize losses in the front and rear paths. Then, to realize the SPI bus control timing of the phase shifter and attenuator, the serial communication control is used to reduce the I/O port, the circuit port is designed in a cascade mode; where the phase shifter is the hardware SPI control, and the attenuator is the software SPI control.

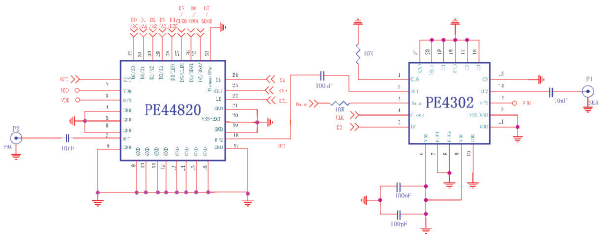

(a)

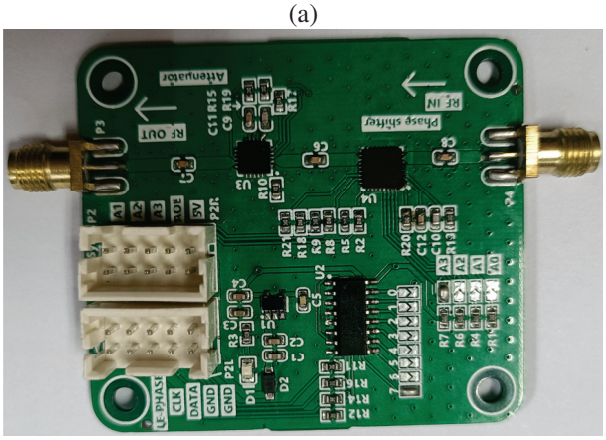

(b)

Fig. 6. (a) Circuit schematic and (b) photo of phase shift attenuation module.

To realize the software addressing of the attenuator, the 74HC238 decoder is extended. The schematic and physical diagram is shown in Fig. 6.

The S_{11} parameters of the phase shift attenuation module were measured by the AV3656B vector network analyzer, as shown in Fig. 7, with −15 dB at 2.4 GHz, and the bandwidth was 1.1∼4.4 GHz.

With a step of 45°and a step of 0.5 dB, respectively, the vector network test results are obtained as

Fig. 7. S_{11} parameters of phase shift attenuation module.

shown in Fig. 8. The relative phase error of the module is 1.2 3.8°, the relative amplitude decay error is within 0.0056-0.0109 dB, which is within an acceptable range, and the main lobe of the beam has a certain width to accommodate this error value.

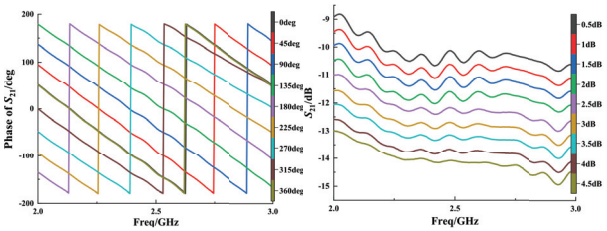

(a) (b)

Fig. 8. (a) Phase shift and (b) attenuation of the module.

In order to output the power of 1 W to the antenna end, a two-stage RF PA structure is adopted. A preamplifier SBB5089 with high linear gain and a RF PA SKY65135 with higher gain of 33 dB are designed as shown in Fig. 9. After the signal is amplified by a two-stage PA, a power of 30 dBm is radiated through the antenna.

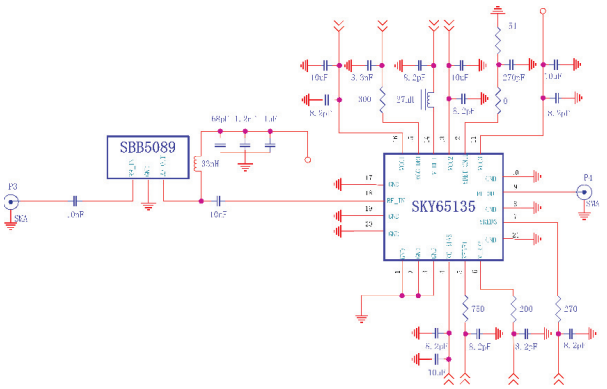

Fig. 9. Schematic of RF power amplifier modules.

IV. EXPERIMENT AND DISCUSSION

To verify the beam steering capability, we set up an experimental platform for data acquisition as shown in Fig. 10 (a). The experimental platform includes an RF source, transmit array, receive antenna, spectrum analyzer, MCU and computer interface. Note that the transmit array and receive antenna are mounted separately on a rotator and slider. This makes it easy to measure the radiation performance under different angles and operating modes.

Figure 10 (b) shows the simulated and measured radiation patterns of the time-division multiplexed transmission mode, where the power is cycled at 1-minute intervals to targets located at 0°, 10°, 20°, 30°, and 40° at a distance of 3 meters. Although the measured side lobe is larger than the simulated one, the main lobe is essentially the same as the corresponding angle of the simulation.

As described in Section II, for the multi-target loading scenario, we can use the full array single beam by the time division mode or use the array partition mode. The array partition mode has real-time performance, and the subarray division of a one-dimensional array is simple. This system adopts the technique of evenly divid-

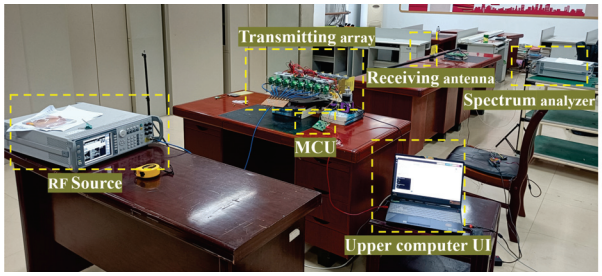

(a)

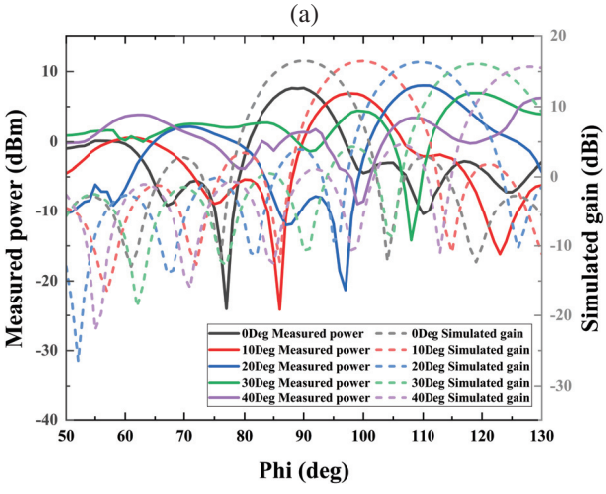

(b)

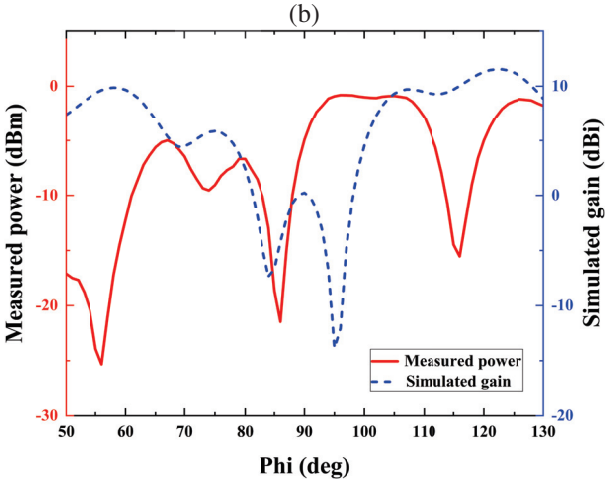

(c)

Fig. 10. *Continued.*

Table 2: Comparison with other reported WPT systems

Refs.	Antenna Types	Operating Frequency	Single Antenna Gain	RF Output Power (Distance)	Output Power	Number of Arrays	Phase-Controlled Mode
[22]	Patch antenna	2.45 GHz	6.64dBi	4 m	N/A	6×24	Retrodirective array antenna (RDA)
[23]	Patch antenna	2.4 GHz	21dBi (Array gain)	2 m	N/A	4×4	Phased array control
[24]	Patch antenna	5.8 GHz	–	10 m	−2.5 dBm	8×8× (4×4)	Single direction transmission
[25]	Patch antennas	2.45 GHz	5.9dBi	1 m	10 dBm	16×1	Retrodirective array antenna (RDA)
This work	Quasi-Yagi antenna	2.4 GHz	9.38dBi	3 m	7.5 dBm	1×8	Phased array control

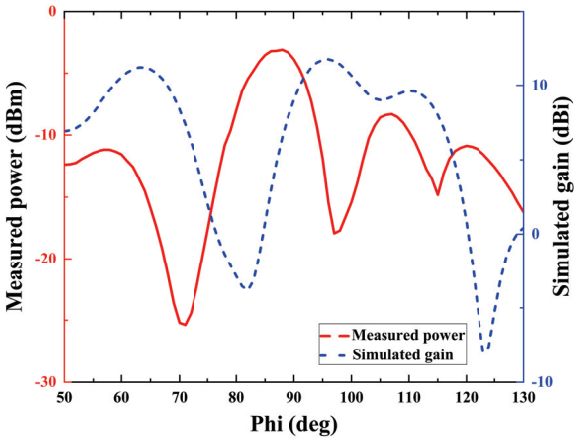

(d)

Fig. 10. (a) Experimental platform for data acquisition, (b) simulated and measured radiation patterns of time-division transmission mode, and (c,d) simulated and measured multi-beam radiation pattern of array-partition mode at two targets in direction of 60° and 130°, respectively, and three targets in direction of 60°, 90 and 110°, respectively.

ing the array according to the number of receivers. For even-numbered targets, the transmit antenna array can be evenly divided into even-numbered parts. For odd-numbered targets, the transmit antenna array separates more antennas for distant targets based on the even division.

Figure 10 (c) shows the received power and simulated radiation patterns of the antenna array after placing two targets at a distance of 3 meters at 60° and 130°, respectively. Figure 10 (d) shows the received power and simulated radiation patterns of the antenna array after beamforming at three target nodes at a distance of 3 meters at 60°, 90° and 110°. There are some differences between the test results and the simulation results, mainly because the channel amplitude and phase consistency of the system design is different from the simulation situation. The energy reflection caused by the test environment will also cause some deviation in the results. However, considering the practical charging situation, our system can still meet the charging demand at the required angle.

The performance comparison between this system and the WPT system proposed in the current relevant literature is shown in Table 2.

V. CONCLUSION

In this paper, a single-to-multiple WPT system based on phased array is designed. A novel quasi-Yagi antenna with SSRR is proposed for power transmission to increase the gain and reduce the size, with a gain of 9.38 dBi and a bandwidth of 0.35 GHz. A 1×8 Wilkinson power divider is then designed to construct an antenna array. Two transmission modes of the phased array are constructed so that the whole antenna array can transmit power by array division or time division, with a transmission power of 7.5 dBm at a distance of 3 meters. Experiments have verified that this transmission system can transmit power to multiple targets and achieve the effect of one-to-multiple wireless energy charging. Based on this design, the high-gain multi-mode phase-controlled WPT system can be applied to the power supply occasions of low-power electronic devices such as multi-sensor nodes in the IoT and has broad application prospects.

ACKNOWLEDGMENT

A Project Funded by the Priority Academic Program Development of Jiangsu Higher Education Institutions.

REFERENCES

[1] X. Bai, T. Ali, and L. Xu, "An antenna capable of harvesting radio frequency, vibration, and light energy based on piezoelectric and solar film materials," *Int. J. RF Microw. Comput.-Aided Eng*., vol. 32, no. 2, Feb. 2022.

[2] M. Z. Chaari and R. Al-Rahimi, "Energized IoT devices through RF wireless power transfer," in *2021 International Symposium on Electrical and Electronics Engineering (ISEE),* Ho Chi Minh, Vietnam, pp. 199-203, Apr. 2021.

[3] C. Shao, H. Roh, and W. Lee, "Next-generation RF-powered networks for Internet of Things: Architecture and research perspectives," *J. Netw. Comput. Appl*., vol. 123, pp. 23-31, Dec. 2018.

[4] W. A. Indra, S. G. Herawan Industrial, N. S. Zamzam, S. B. M. N. Fakulti, N. B. H. Fakulti, and F. Zuska, "Development of a guided drone powered by radio frequency energy harvesting," in *2021 IEEE International Conference in Power Engineering Application (ICPEA),* Malaysia, pp. 127-131, Mar. 2021.

[5] D. R. Kesari Mary, E. Ko, D. J. Yoon, S.-Y. Shin, and S.-H. Park, "Energy optimization techniques in underwater Internet of Things: Issues, state-of-the-art, and future directions," *Water*, vol. 14, no. 20, Art. no. 20, Jan. 2022.

[6] X. Zhu, K. Jin, Q. Hui, W. Gong, and D. Mao, "Long-range wireless microwave power transmission: A review of recent progress," *IEEE J. Emerg. Sel. Top. Power Electron.*, vol. 9, no. 4, pp. 4932-4946, 2021.

[7] Y. Luo and L. Pu, "Practical issues of RF energy harvest and data transmission in renewable radio energy powered IoT," *IEEE Trans. Sustain. Comput*., vol. 6, no. 4, pp. 667-678, Oct. 2021.

[8] N. Shinohara, "Trends in wireless power transfer: WPT technology for energy harvesting, mllimeter-wave/THz rectennas, MIMO-WPT, and advances in near-field WPT applications," *IEEE Microw. Mag.*, vol. 22, no. 1, pp. 46-59, 2021.

[9] Z. Popovic, "Near- and far-field wireless power transfer," in *2017 13th International Conference on Advanced Technologies, Systems and Services in Telecommunications (TELSIKS),* Nis, pp. 3-6, Oct. 2017.

[10] J. Huang, Y. Zhou, Z. Ning, and H. Gharavi, "Wireless power transfer and energy harvesting: Current status and future prospects," *IEEE Wirel. Commun.*, vol. 26, no. 4, 2019.

[11] Q. Hui, K. Jin, and X. Zhu, "Directional radiation technique for maximum receiving power in microwave power transmission system," *IEEE Trans. Ind. Electron.*, vol. 67, no. 8, pp. 6376-6386, Aug. 2020.

[12] J. H. Park, D. I. Kim, and K. W. Choi, "Analysis and experiment on multi-antenna-to-multi-antenna RF wireless power transfer," *IEEE Access*, vol. 9, pp. 2018-2031, 2021.

[13] P. D. Hilario Re, S. K. Podilchak, S. A. Rotenberg, G. Goussetis, and J. Lee, "Circularly polarized retrodirective antenna array for wireless power transmission," *IEEE Trans. Antennas Propag.*, vol. 68, no. 4, pp. 2743-2752, Apr. 2020.

[14] K. Arai, K. Wang, M. Toshiya, M. Higaki, and K. Onizuka, "A tile-based 8×8 triangular grid array beamformer for 5.7 GHz microwave power transmission," pp. 101-104, 2021.

[15] K. H. Jeong and N. Ghalichechian, "3D-printed 4-zone Ka-band Fresnel lens: Design, fabrication, and measurement," *IET Microw. Antennas Propag.*, vol. 14, no. 1, pp. 28-35, Jan. 2020.

[16] L. Zhu, J. Zhang, W. Han, L. Xu, and X. Bai, "A novel RF energy harvesting cube based on air dielectric antenna arrays," *Int. J. RF Microw. Comput.-Aided Eng.*, vol. 29, no. 1, p. e21636, Jan. 2019.

[17] T. Gao, X. Wang, L. Jiang, J. Hou, and Y. Yang, "Research on power distribution in multiple-input multiple-output magnetic coupling resonance wireless power transfer system," *Electr. Eng.*, vol. 103, no. 6, pp. 3217-3224, Dec. 2021.

[18] W. Zhou, M. Stead, S. Weiss, O. Okusaga, and Z. R. Huang, "Developing an integrated photonic system with a simple beamforming architecture for phased-array antennas," *Appl. Opt.,* vol. 56, no. 3, p. B5, Jan. 2017.

[19] W.-Y. Zhou, Z.-L. Mei, and M. Lu, "A compact quasi-Yagi antenna with high gain by employing the bent arms and split-ring resonators," *Int. J. Antennas Propag.*, vol. 2021, pp. 1-9, Feb. 2021.

[20] L. A. Feng, Z. Y. Heng, and W. Z. Jun, "Design of a broadband microstrip quasi-Yagi antenna with split-ring resonators," in *2021 IEEE 6th International Conference on Computer and Communication Systems (ICCCS),* Chengdu, China, pp. 819-822, Apr. 2021.

[21] A. Naghar, O. Aghzout, A. V. Alejos, D. A. Outerelo, and F. Falcone, "Improvement of notch performances for UWB monopole antennas using CSRR and SSRR," in *2016 5th International Conference on Multimedia Computing and Systems (ICMCS),* Marrakech, Morocco, pp. 456-458, Sep. 2016.

[22] C. An and H.-G. Ryu, "Power efficiency and antenna array dimension of middle range wireless power transmission," in *2020 International Workshop on Antenna Technology (iWAT),* Bucharest, Romania, pp. 1-4, Feb. 2020.
[23] K. Lee, J. Kim, and C. Cha, "Microwave-based wireless power transfer using beam scanning for wireless sensors," in *IEEE EUROCON 2019 18th International Conference on Smart Technologies*, Novi Sad, Serbia, pp. 1-5, July 2019.
[24] X. Yi, X. Chen, L. Zhou, S. Hao, B. Zhang, and X. Duan, "A microwave power transmission experiment based on the near-field focused transmitter," *IEEE Antennas Wirel. Propag. Lett.*, vol. 18, no. 6, pp. 1105-1108, June 2019.
[25] S.-T. Khang, D.-J. Lee, I.-J. Hwang, T.-D. Yeo, and J.-W. Yu, "Microwave power transfer with optimal number of rectenna arrays for midrange applications," *IEEE Antennas Wirel. Propag. Lett.*, vol. 17, no. 1, pp. 155-159, Jan. 2018.

Xue Bai was born in 1975. She received her Ph.D. degree in the field of Agricultural Information Technology from Jiangsu University in 2011. She is now an Associate professor in School of Electrical and Information Engineering, Jiangsu university, China. Her current research area is agricultural IoT and self-power technology for sensors.

Yanjiao Hou comes from Hulunbuir, Inner Mongolia, majoring in electrical engineering and graduated from Jiangsu University. She is currently working in the hardware field.

Leijun Xu was born in 1976. He received his Ph.D. degree in the field of RF & millimeter-wave integrated circuit from Southeast University in 2010. He is now a professor in School of Electrical and Information Engineering, Jiangsu university, China. His current research area is RF & THz integrated circuit for agricultural application.

Jianfeng Chen was born in 1987. Obtained a doctoral degree in Electromagnetic Field and Microwave Technology from Southeast University in 2021. He is currently a lecturer at the School of Electrical and Information Engineering, Jiangsu University, China. His current research field is electromagnetic fields and electromagnetic waves.

Yiyang Kong was born in 1998. He is currently a graduate student majoring in Agricultural Electrification and Automation at Jiangsu University. His research field is agricultural IoT and self-power technology for sensors.

Dual-band Circularly-polarized Millimeter-wave Substrate Integrated Waveguide Slot Antenna Array with a Small Frequency Ratio

Jianxing Li, Xiaoyan Yu, Sifan Wu, Sen Yan, and Kai-Da Xu

School of Information and Communications Engineering
Xi'an Jiaotong University, Xi'an 710049, China
jianxingli.china@xjtu.edu.cn, yuxiaoyan11@qq.com, sen.yan@xjtu.edu.cn, wu-sifan@stu.xjtu.edu.cn, kaidaxu@ieee.org

***Abstract* –** In this paper, a 4×4 dual-band circularly-polarized (CP) substrate integrated waveguide (SIW) slot antenna array with a small frequency ratio (FR) is investigated in the Ka-band. The proposed antenna array achieves the small FR by radiating two high-order modes, i.e. TM_{130} and TM_{230}, with close resonant frequencies. To realize CP performance, a sequential rotated feeding (SRF) network is used to design a 2×2 subarray. A 4×4 CP antenna array is further developed to enhance the directivity. Measured results show the antenna array achieves impedance bandwidth ($|S_{11}| <$ -10 dB) of 27.35-27.96 GHz at the lower band and 29.62-30.58 GHz at the higher band with an FR of only 1.1. The measured 3-dB axial-ratio (AR) bandwidths are obtained as 27.66-27.78 GHz and 30.34-30.45 GHz with right-handed circularly-polarized (RHCP) peak gains of 16.9 and 16.8 dBi, respectively. The proposed antenna array is a potential candidate for millimeter-wave communication systems.

***Index Terms* –** Circularly-polarized (CP) antenna, dual-band, slot antenna, small frequency ratio (FR), substrate integrated waveguide (SIW).

I. INTRODUCTION

With the rapid development of modern wireless communications, 5G wireless communication has emerged as a widely adopted technology. The millimeter-wave (mmWave) technology has the potential to meet the channel resources required by 5G communication systems, due to its characteristics of wide bandwidth, short wavelength, and low delay. Moreover, circularly-polarized (CP) antennas are preferred for the merits of reducing polarization mismatch and multipath effect. Therefore, many mmWave CP antennas are reported in recent years, including magneto-electric (ME) dipole antennas [1, 2], patch antennas [3–5], and substrate integrated waveguide (SIW) antennas [6, 7].

However, the aforementioned antennas operate at single band. To enhance the channel capacity and reduce the volume of the antenna, several dual-band CP antennas in mmWave band are proposed [8–12]. In [9], the SIW cavity backed antenna achieves dual-band CP performance at 28 GHz and 38 GHz by using two pairs of patches. In [10], two pairs of ME-dipoles are used to generate CP waves at 20 GHz and 30 GHz. In [11], a stacked dielectric resonator antenna also achieves dual-band CP radiation at 20 GHz and 30 GHz.

Nevertheless, these antennas have a frequency ratio (FR) larger than 1.36. In many situations, small FR antennas are desired. However, in the literature, most of the dual-band CP antennas with small FR operate at microwave band and use microstrip structures [13–15]. With the increase of the working frequency of the antenna, the loss caused by dielectrics also increase. To reduce losses in higher band, SIW technology is extensively used in antenna designs. In [16], a dual-band SIW CP antenna using triangular slots achieves a small FR of 1.26. The SIW CP antenna with circular slots in [17] achieves an FR of 1.27. Although many dual-band SIW CP antennas in mmWave band have been proposed, it is still challenging to realize a SIW CP antenna with a small FR.

In this paper, a dual-band CP SIW slot antenna array with a small FR is proposed in the Ka-band. Two high order mode, i.e. TM_{130} and TM_{230}, with close resonant frequencies are radiated by properly curving slots on the surface of the SIW cavity. Hence, the antenna achieves dual-band performance and small FR. A sequential rotated feeding (SRF) network is employed to design a 2×2 subarray to achieve CP performance. Finally, a 4×4 CP antenna array is further designed, fabricated, and evaluated, which has a measured FR of 1.1. The measured results demonstrate its suitability for 5G communication systems.

II. ANTENNA ELEMENT DESIGN AND ANALYSIS

A. Antenna configuration

The configuration of the proposed SIW antenna element is displayed in Fig. 1. The antenna element consists of three metal layers and two 0.254 mm Rogers 5880

Submitted On: July 28, 2023
Accepted On: November 4, 2024

https://doi.org/10.13052/2024.ACES.J.391008

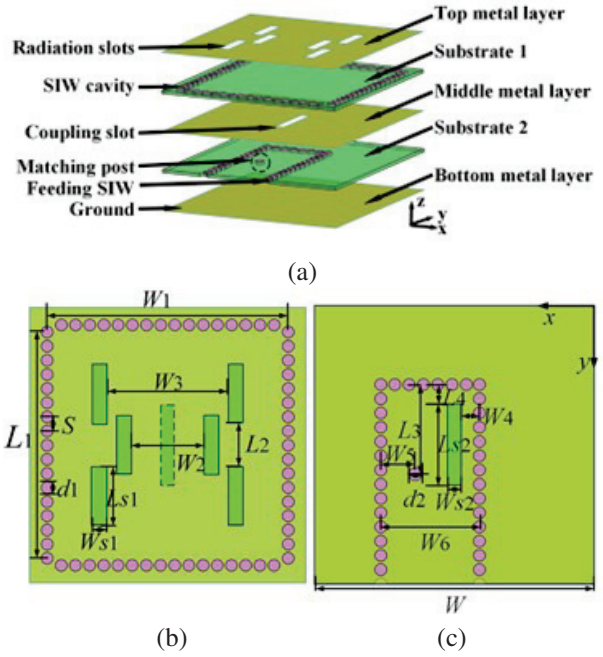

Fig. 1. Configuration of the antenna element: (a) 3-D perspective, (b) overhead view of Substrate 1, and (c) overhead view of Substrate 2

substrates (ε_r =2.2, tanδ =0.0009). The SIW resonant cavity is designed in Substrate 1 and the feeding SIW is designed in Substrate 2. To radiate high-order modes, six radiating slots are etched on the top metal layer. A slot is used to transfer electromagnetic energy. The bottom metal layer serves as the ground plane. A matching post is introduced in Substrate 2 to adjust impedance matching.

The resonant frequency of TM$_{mnp}$ in the SIW cavity can be calculated as follows [18]:

$$f = \frac{c}{2\sqrt{\varepsilon_r \mu_r}} \sqrt{\left(\frac{m}{a_e}\right)^2 + \left(\frac{n}{b_e}\right)^2 + \left(\frac{p}{d}\right)^2} \quad (1)$$

$$a_e = W_1 - 1.08\frac{{d_1}^2}{S} + 0.1\frac{{d_1}^2}{W_1} \quad (2)$$

$$b_e = L_1 - 1.08\frac{{d_1}^2}{S} + 0.1\frac{{d_1}^2}{L_1} \quad (3)$$

where relative permittivity and permeability of the substrate are represented by ε_r and μ_r, respectively. The equivalent SIW cavity's length, width, and height are denoted by a_e, b_e, and d. The variables m, n, and p represent the number of variations in the standing wave pattern along the x, y, and z axis, respectively. Furthermore, d_1 refers to the diameter of vias while S represents the spacing between adjacent vias, respectively. To get the specific parameters of the antenna, the dual-band antenna is firstly decided to operate in millimeter-wave band. Secondly, high-order modes TM$_{130}$ mode and TM$_{230}$ mode are decided to realize the dual-band antenna. After calculation and optimization, the detailed physical sizes of the antenna element are tabulated in Table 1. Given the physical parameters, some resonant frequencies are calculated according to equations (1-3) and shown in Table 2.

Table 1: Dimensions of the antenna element (unit: mm)

W	W_1	L_1	W_2	L_2	W_3
15	13.1	13.1	4	2.4	6.6
L_3	W_4	L_4	W_5	W_6	Ws_1
4.9	1	1.1	1.9	5.3	0.8
Ls_1	Ws_2	Ls_2	d_1	d_2	S
3.2	0.7	4.4	0.6	0.7	0.8

Table 2: Resonant frequencies of high-order modes (unit: GHz)

n \ m	1	2	3
1	12.29	19.43	27.47
2	19.43	24.57	31.32
3	27.47	31.32	36.86

B. Dual-band radiation mechanism

High-order modes are decided to realize dual-band antenna. To achieve dual-band radiation with a small FR, TM$_{130}$ and TM$_{230}$ modes with resonant frequencies of 27.47 GHz and 31.32 GHz, respectively, are employed according to Table 2, implying a FR of 1.14. All simulated results are performed by using CST Microwave Studio 2018. The E-field distributions of TM$_{130}$ mode at 27.47 GHz and TM$_{230}$ mode at 31.32 GHz in the SIW cavity without coupling slot excitation are shown in Fig. 2. The E-field distributions of TM$_{130}$ mode at 27.34 GHz and TM$_{230}$ mode at 30.12 GHz in Substrate 1 with coupling slot excitation is displayed in Fig. 3. Note that the resonant frequencies are slightly reduced owing to

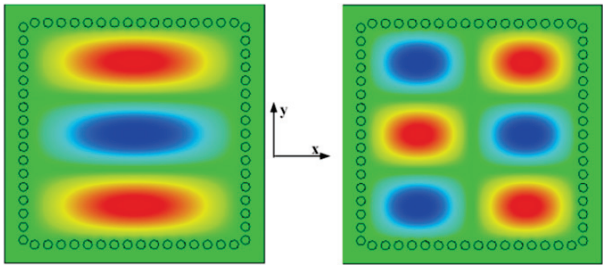

Fig. 2. E-Field distributions in the SIW resonant cavity without coupling slot excitation: (a) TM$_{130}$ mode and (b) TM$_{230}$ mode.

the existence of the coupling slot. In Fig. 3 (a), it can be clearly seen that the phases of the *E*-field on both sides of the coupling slot are reversed, which means that the TM_{130} mode is converted into a quasi-TM_{230} mode upon excitation. Hence, the same radiating structure can be utilized to radiate TM_{130} and TM_{230} modes simultaneously. Therefore, six slots, as radiating structures, are curved in each subregion where the standing wave reaches its peak. The slots are arranged alternatively on either side of the centerline to ensure that they emit electromagnetic energy with identical phase. Finally, TM_{130} and TM_{230} modes are radiated, thereby achieving a dual-band performance.

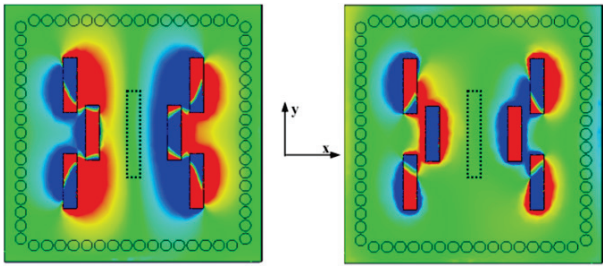

(a) (b)

Fig. 3. E-Field distributions in the SIW resonant cavity with coupling slot excitation: (a) TM_{130} mode and (b) TM_{230} mode.

C. Antenna element performance

A dual-band antenna element is achieved after optimizing the antenna parameters. As illustrated in Fig. 4, the simulated impedance bandwidths ($|S_{11}| <$ -10 dB) of the antenna element are 27.27 to 27.40 GHz and 30.07 to 30.16 GHz. The simulated peak gains are 11.1 dBi at 27.34 GHz and 10.4 dBi at 30.12 GHz, and the cross-polarization is less than -55 dB in both bands, as shown in Fig. 5.

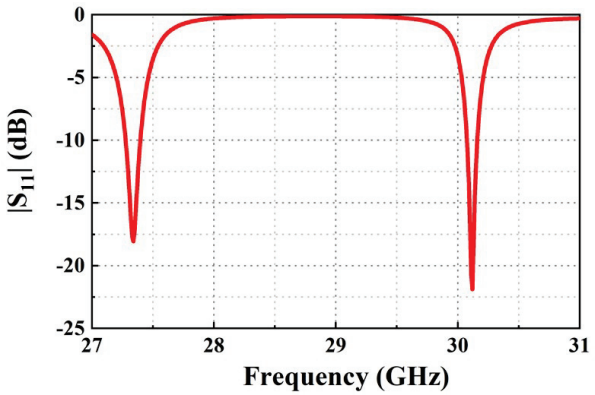

Fig. 4. Simulated $|S_{11}|$ of the antenna element.

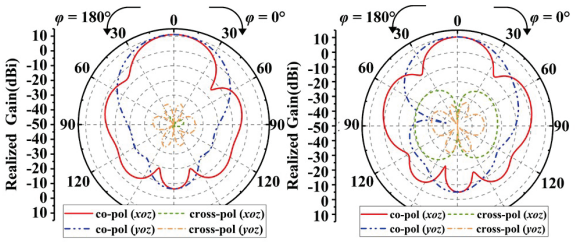

(a) (b)

Fig. 5. Simulated radiation patterns of the antenna element at (a) 27.34 GHz and (b) 30.12 GHz.

III. ANTENNA ARRAY DESIGN

A. 2×2 CP antenna subarray

A 2×2 CP subarray is first designed based on the antenna element, which can be found in Fig. 6. To achieve CP performance, an SRF network is utilized to design the antenna subarray. The antenna elements are placed sequentially on the four ports of the SRF network. In Fig. 6 (b), a 1-to-4 power divider using SRF network is designed on Substrate 2. To ensure equal power distribution among the four output ports, the lengths of the paths taken by the electromagnetic wave are carefully adjusted. A matching post is introduced in each way of the feeding network to achieve good power division and phase shift performance. Hence, the adjacent ports of the SRF network have the phase difference of 90°. Therefore, the adjacent antenna elements are not only spatially orthogonal, but also the feed phase. CP performance is achieved by the antenna subarray.

The simulated reflection coefficient and axial-ratio (AR) of the subarray are shown in Fig. 7. Since Figs. 4 and 7 are produced by different models, these two figures are separated. The subarray achieves -10 dB impedance bandwidths at the range of 27.27-27.61 GHz and 30.14-

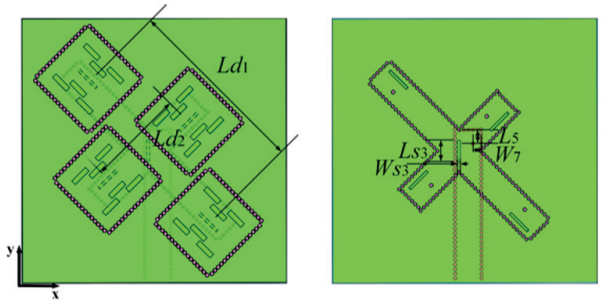

(a) (b)

Fig. 6. Geometry of the 2 × 2 CP antenna subarray: (a) top view of the antenna subarray and (b) feeding network. The parameters of the antenna subarray are: $Ld_1 = 30.9$ mm, $Ld_2 = 16.1$ mm, $L_5 = 2.4$ mm, $Ls_3 = 3.7$ mm, $Ws_3 = 0.5$ mm, and $W_7 = 1.4$ mm.

30.38 GHz. Due to the employment of the SRF network, right-handed circularly-polarized (RHCP) radiation is achieved with bandwidths of 27.44-27.52 GHz at the lower band and 30.28-30.34 GHz at the higher band with FR of 1.1. Figure 8 displays the simulated radiation patterns of the antenna subarray, which exhibit significant directivity enhancements. The peak gains simulated by the subarray are 12.2 dBi at 27.48 GHz and 12.0 dBi at 30.31 GHz.

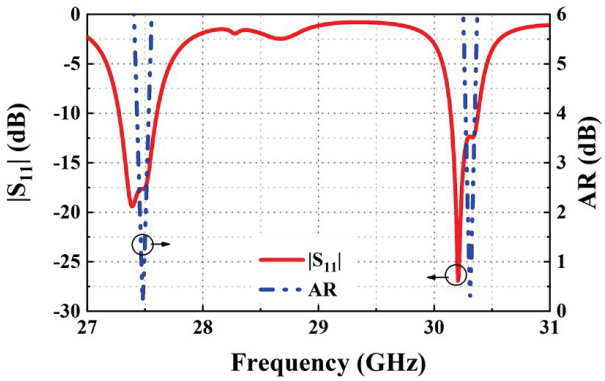

Fig. 7. Simulated reflection coefficient and AR of the antenna subarray.

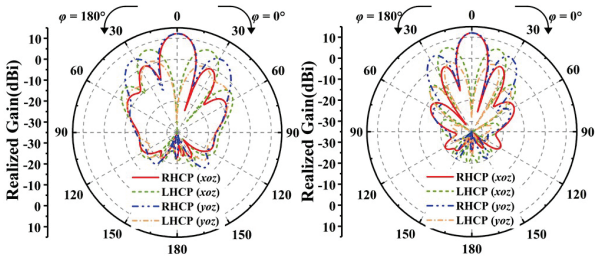

Fig. 8. Simulated radiation patterns of the antenna subarray at (a) 27.48 GHz and (b) 30.31 GHz.

B. 4×4 CP antenna array

To improve the directivity even further, a 4×4 CP antenna array is developed. The overall configuration of the antenna array can be seen in Fig. 9, while the detailed geometries of the three substrates are provided in Fig. 10. which contains a grounded co-planar waveguide (GCPW) to SIW transition and a 1-4 power divider. The GCPW-SIW serves as the feeding port for the antenna array. The electromagnetic energy is input from the feeding port. An SIW feeding network is designed in Substrate 3 and coupled to Substrate 2 through the power divider. An SRF has been incorporated into Substrate 2 to facilitate coupling of electromagnetic energy to the antenna elements located in Substrate 1.

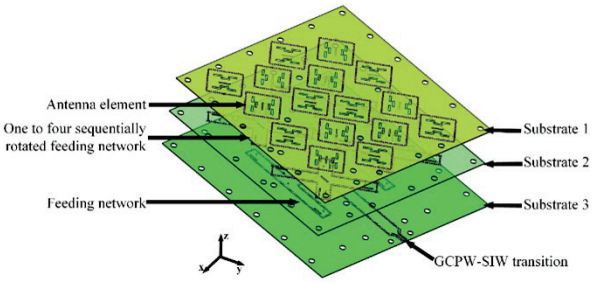

Fig. 9. Configurations of the 4×4 CP antenna array.

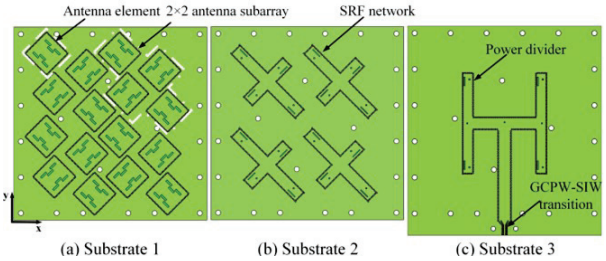

Fig. 10. Detailed geometries of the three substrates.

IV. RESULTS AND DISCUSSIONS

The 4×4 CP antenna array is fabricated as shown in Fig. 11 (a), and the anechoic chamber for testing the far-field radiation pattern is presented in Fig. 11 (b). The $|S_{11}|$ of the antenna is measured using an Agilent vector analyzer E8363B. Comparison between the simulated and measured $|S_{11}|$ and AR results can be seen in Fig. 12. The measurement results are consistent with the simulation results. At the lower band, the simulated and measured impedance bandwidths are 27.43-27.83 GHz and 27.35-27.96 GHz, while both simulated and measured 3-dB AR bandwidths are within the range of 27.63-27.72 GHz and 27.66-27.78 GHz, respectively. At the higher band, the simulated and measured impedance bandwidths are 30.28-30.52 GHz and 29.62-30.58 GHz. For AR bandwidths, they lie within a range of 30.37-30.44 GHz and 30.34-30.45 GHz, respectively. The mea-

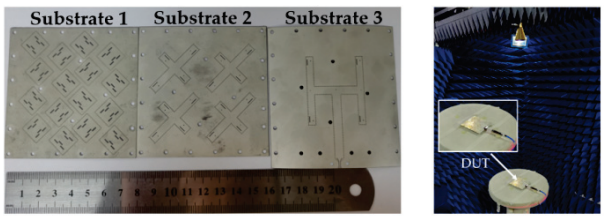

Fig. 11. Photographs of the fabricated antenna array: (a) antenna array prototype and (b) measurement setup.

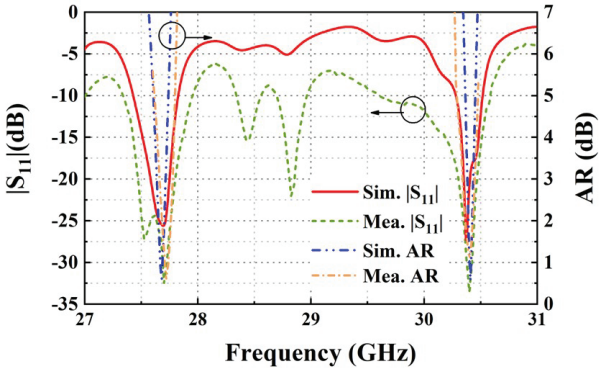

Fig. 12. Simulated and measured $|S_{11}|$ and AR.

sured results indicate that a small FR of 1.1 is achieved. The measured bandwidths are slight wider than the simulations, which is most likely due to the air gap between the different substrates.

Figures 13 and 14 depict the normalized radiation patterns of the proposed antenna array at frequencies of 27.68 GHz and 30.41 GHz, respectively. The simulated and measured radiation patterns and gain are in good agreement for both bands. The measured 3-dB AR beamwidths at 27.68 GHz are approximately 11° in the *xoz*-plane and 9° in the *yoz*-plane, respectively. Similarly, the measured 3-dB AR beamwidths are approximately 9° in the *xoz*-plane and 7° in the *yoz*-plane, respectively, at 30.41 GHz. The cross-polarization levels of the main beams remain below -28 dB for both operating bands The simulated and measured peak gains of the antenna array are 18.8 dBi and 16.9 dBi at the lower band, as well as 18.5 dBi and 16.8 dBi at the higher band, respectively. Sidelobe levels remain under -9 dB for both bands. The discrepancies between simulated results versus measurement may be attributed to fabrication inaccuracies or assembly errors during antenna construction process.

Table 3 compares the performance between the proposed antenna and some previous dual-band CP antennas. The proposed antenna array has advantages of a small FR 1.1, while keeping high gain, dual-band and CP performances.

In this paper, a dual-band CP SIW slot antenna array based on high-order modes is proposed. The antenna element achieves dual-band performance and a small FR by radiating TM_{130} and TM_{230} modes simultaneously. To achieve CP performance, an SRF network is used to firstly design a 2×2 CP antenna subarray. Furthermore, a 4×4 CP antenna array is further constructed to enhance the directivity. Measurement results show that the antenna array achieves RHCP performance in both bands. The proposed antenna could find applications in modern mmWave communication systems.

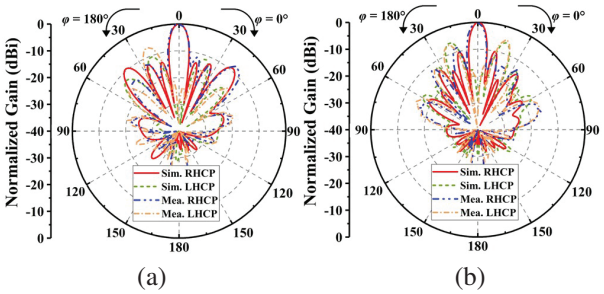

(a) (b)

Fig. 13. Simulated and measured normalized radiation patterns at 27.68 GHz (a) $\varphi = 0°$ and (b) $\varphi = 90°$.

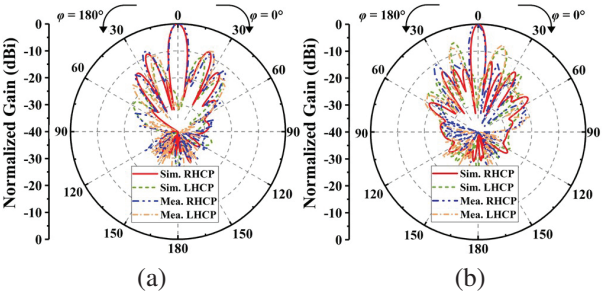

(a) (b)

Fig. 14. Simulated and measured normalized radiation patterns at 30.41 GHz (a) $\varphi = 0°$ and (b) $\varphi = 90°$.

Table 3: Comparison with previous dual-band CP antennas

Reference	Technique	FR	Imp. BW (−10dB)%
[13]	Microstrip	1.12	3.3/2.6
[19]	Microstrip	1.42	3.6/3.3
[20]	Patch	1.1	3.0/2.7
[21]	Patch	1.55	0.5/1.3
Proposed	**SIW**	**1.1**	**2.2/3.2**

ACKNOWLEDGMENT

This work was supported in part by the National Key R&D Program of China under Grant 2021YFA0717500, in part by the "Siyuan Scholar" Fellowship of XJTU, and in part by the Shaanxi Province Innovation Capability Support Program under Grant 2023KJXX-130.

REFERENCES

[1] Y. Z. Tian, O. Y. Jun, P. F. Hu, and Y. M. Pan, "Millimeter-wave wideband circularly polarized endfire planar magneto-electric dipole antenna based on substrate integrated waveguide," *IEEE Antennas Wirel. Propag. Lett.*, vol. 21, no. 1, pp. 49-53, 2022.

[2] B. T. Feng, J. X. Lai, K. Chung, T. Y. Chen, Y. Y. Liu, and C. Y. D. Sim, "A compact wideband

circularly polarized magneto-electric dipole antenna array for 5G millimeter-wave application," *IEEE Trans Antennas Propag.*, vol. 68, no. 9, pp. 6838-6843, 2020.

[3] S. B. T. Naganathan, S. Dhandapani, and T. Packirisamy, "Analysis of super-solar integrated patch antenna for sub-6 GHz and beyond 6 GHz millimeter wave 5G applications," *Applied Computational Electromagnetics Society (ACES) Journal*, vol. 37, no. 10, pp. 1039-1050, 2022.

[4] C. M. Zhu, G. H. Xu, D. W. Ding, J. Wu, W. Wang, Z. X. Huang, and X. L. Wu, "Low-profile wideband millimeter-wave circularly polarized antenna with hexagonal parasitic patches," *IEEE Antennas Wirel. Propag. Lett*., vol. 20, no. 9, pp. 1651-1655, 2021.

[5] H. F. Xu, J. Y. Zhou, K. Zhou, Q. Wu, Z. Q. Yu, and W. H, "Planar wideband circularly polarized cavity-backed stacked patch antenna array for millimeter-wave applications," *IEEE Trans Antennas Propag.*, vol. 66, no. 10, pp. 5170-5179, 2018.

[6] Y. M. Hussein, M. K. A. Rahim, N. A. Murad, H. O. Hanoosh, and N. B. M. Nadzir, "Substrate integrated waveguide antenna at millimeter wave for 5G application," *Applied Computational Electromagnetics Society (ACES) Journal*, vol. 37, no. 4, pp. 478-484, 2022.

[7] L. Zhang, K. Wu, S. W. Wong, Y. J. He, P. Chu, W. T. Li, K. X. Wang, and S. Gao, "Wideband high-efficiency circularly polarized SIW-fed S-dipole array for millimeter-wave applications," *IEEE Trans Antennas Propag*., vol. 68, no. 3, pp. 2422-2427, 2020.

[8] S. S. Marasht, M. S. Sharawi, and A. Zhu, "Dual-band circularly polarized antenna array for 5G millimeter-wave applications," *IEEE Open Journal Antennas Propag*., vol. 3, pp. 314-323, 2022.

[9] C. M. Zhu, G. H. Xu, A. D. Ren, W. Wang, Z. X. Huang, and X. L. Wu, "A compact dual-band dual-circularly polarized SIW cavity-backed antenna array for millimeter-wave applications," *IEEE Antennas Wirel. Propag. Lett*., vol. 21, no. 8, pp. 1572-1576, 2022.

[10] S. Liu, W. Wu, and D.-G. Fang, "Dual-band dual-circularly polarized antenna array with printed ridge gap waveguide," *IEEE Trans Antennas Propag.,* vol. 69, no. 8, pp. 5118-5123, 2021.

[11] H. Xu, Z. J. Chen, H. W. Liu, L. Chang, T. T. Huang, S. Ye, L. Zhang, and C. Du, "Single-fed dual-circularly polarized stacked dielectric resonator antenna for K/Ka-band UAV satellite communications," *IEEE Trans Vehicular Tech*., vol. 71, no. 4, pp. 4449-4453, 2022.

[12] X. Y. Yu, S. F. Wu, J. X. Li, K. D. Xu, S. Yan, and J. Chen, "Dual-band circularly-polarized SIW antenna array using high-order modes in Ka-band," in *International Conference on Electronic Information and Communication Technology (ICEICT),* 2022.

[13] Y. H. Xu, L. Zhu, N. W. Liu, and M. Li, "A dual-band dual-circularly-polarized slot antenna with stable in-band gain and reduced frequency ratio under triple resonance," *IEEE Trans Antennas Propag*., vol. 70, no. 11, pp. 10199-10206, 2022.

[14] Y. H. Xu, L. Zhu, and N. W. Liu, "Design approach for a dual-band circularly polarized slot antenna with flexible frequency ratio and similar in-band gain," *IEEE Antennas Wirel. Propag. Lett*., vol. 21, no. 5, pp. 1037-1041, 2022.

[15] Q. S. Wu, X. Zhang, L. Zhu, J. Wang, G. Zhang, and C. B. Guo, "A single-layer dual-band dual-sense circularly polarized patch antenna array with small frequency ratio," *IEEE Trans Antennas Propag*., vol. 70, no. 4, pp. 2668-2675, 2022.

[16] T. Zhang, W. Hong, Y. Zhang, and K. Wu, "Design and analysis of SIW cavity backed dual-band antennas with a dual-mode triangular-ring slot," *IEEE Trans Antennas Propag*., vol. 62, no. 10, pp. 5007-5016, 2014.

[17] H. K. Chen, Y. Shao, Y. J. Zhang, C. H. Zhang, and Z. Z. Zhang, "Low-profile millimeter-wave SIW cavity-backed dual-band circularly polarized antenna," *IEEE Trans Antennas Propag*., vol. 65, no. 12, pp. 7310-7315, 2017.

[18] F. Xua and K. Wu, "Guided-wave and leakage characteristics of substrate integrated waveguide," *IEEE Trans Antennas Propag*., vol. 53, no. 1, pp. 66-73, 2005.

[19] J. D. Zhang, L. Zhu, N. W. Liu, and W. Wu, "Dual-band and dual-circularly polarized single-layer microstrip array based on multiresonant modes," *IEEE Trans Antennas Propag*., vol. 65, no. 3, pp. 1428-1433, 2017.

[20] Z. Wang, R. She, and J. Han, "Dual-band dual-sense circularly polarized stacked patch antenna with a small frequency ratio for UHF RFID reader applications," *IEEE Access*, vol. 5, pp. 15260-115270, 2017.

[21] B. C. Park and J. H. Lee, "Dual-band omnidirectional circularly polarized antenna using zeroth- and first-order modes," *IEEE Antennas Wirel. Propag. Lett*., vol. 11, pp. 407-410, 2012.

Jianxing Li received the B.S. degree in information and communications engineering, and the M.S. and Ph.D. degrees in electromagnetic field and microwave techniques from Xi'an Jiaotong University, Xi'an, China, in 2008, 2011, and 2016, respectively. He is currently a full Professor with Xi'an Jiaotong University. His research interests include microwave and mmWave circuits and antennas, wireless power transfer, and multifunctional mmWave antennas.

Xiaoyan Yu received the bachelor's degree in information and telecommunication engineering from Xi'an Jiaotong University, Xi'an, China, in 2021. She is currently pursuing the master's degree in electronics science and technology, from Xi'an Jiaotong University, Xi'an. Her current research interests include SIW antenna array and mm-Wave circularly-polarized antenna array.

Sifan Wu received the B.S. degree in information engineering and business administration from Xi'an Jiaotong University, Xi'an, China, in 2020, where he is currently pursuing the Ph.D. degree in electronics science and technology. His current research interests include 3-D-printed millimeter-wave filters and antenna arrays. Mr. Wu received the Best Student Paper at the 2021 National Conference on Antennas and the Best Student Paper Award at the 2022 IEEE International Conference on Electronic Information and Communication Technology (ICEICT).

Sen Yan received the bachelor's and master's degrees in information and telecommunication engineering from Xi'an Jiaotong University, Xi'an, China, in 2007 and 2010, respectively, and the Ph.D. degree in electrical engineering from Katholieke Universiteit Leuven (KU Leuven), Leuven, Belgium, in 2015. He has authored and coauthored more than 150 international journal and conference contributions. His research interests include microwave metamaterials and metasurfaces, wearable devices and textile antennas, antenna diversity, and microwave biosensors.

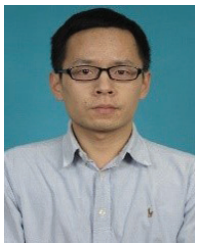

Kai-Da Xu received the B.E. and Ph.D. degrees in electromagnetic field and microwave technology from the University of Electronic Science and Technology of China (UESTC), Chengdu, China, in 2009 and 2015, respectively. He has authored and coauthored over 160 articles in peer-reviewed journals and over 50 papers in conference proceedings. His current research interests include RF/microwave, millimeter-wave/THz devices, and antenna arrays.

Wideband Cup Dielectric Resonator Antenna With Stable Omnidirectional Patterns

Shuxin Zheng[1], Nan Yang[2], Xiaoming Chen[1], Zhen-Yuan Zhang[3], Bingyi Qian[1], and Ahmed A. Kishk[4]

[1]School of Information and Communications Engineering
Xi'an Jiaotong University, Xi'an 710049, China
zheng21761@stu.xjtu.edu.cn, xiaoming.chen@mail.xjtu.edu.cn, Qianbingyi@stu.xjtu.edu.cn

[2]School of Electronics and Information Technology (School of Microelectronics) and Guangdong Provincial Key Laboratory of Optoelectronic Information Processing Chips and Systems
Sun Yat-sen University, Guangzhou 510006, China
yangnan6@mail.sysu.edu.cn

[3]Department of Electrical and Electronic Engineering
South University of Science and Technology of China, Shenzhen 518055, China
Zhangzhen-yuan@outlook.com

[4]Department of Electrical and Computer Engineering
Concordia University, Montreal, QC H3G 1M8, Canada
kishk@encs.concordia.ca

***Abstract* –** A wideband omnidirectional cup dielectric resonator antenna (CDRA) is designed by utilizing three modes (DR $TM_{01\delta}$, coil, and monopole modes) for the first time. It deploys the modified coil feeding structure comprising four coil segments and two close-by probes. The four coil segments provide an equivalent magnetic-current loop and the two probes act as an electric monopole. Thus, the modified feeding structure can excite the DR $TM_{01\delta}$ mode and two neighbor resonances extending the operating bandwidth. All of these modes have omnidirectional characteristics. To verify the idea, a CDRA is designed, fabricated, and measured. The CDRA is $0.61\,\lambda_0 \times 0.32\,\lambda_0$ (where λ_0 is the free-space wavelength at the center frequency) with a bandwidth of 67.7% (3.28-6.64 GHz). The antenna has stable omnidirectional radiation patterns, high radiation efficiencies, and a low cross-polarized level within the operating bandwidth.

***Index Terms* –** Dielectric resonator antenna (DRA), omnidirectional, wideband.

I. INTRODUCTION

Dielectric resonator antennas (DRAs) have attracted tremendous attention for their compact sizes, various radiation patterns, bandwidths, and high efficiencies. Omnidirectional DRAs can be used for various wireless communications because of their broad coverage [1–4]. However, designing a wideband and compact DRA with a stable omnidirectional pattern is nontrivial.

Many omnidirectional antennas exist in the literature [1–30]. There are various traditional methods to realize omnidirectional antenna, such as a wire in free space [5], exciting the circular patch antenna's higher-order modes [5], and loading the circular patch antenna with an annular ring [6–8]. Antennas, with four bent dipoles [9], based on substrate integrated waveguides (SIWs) [10], and with surface wave [11], all had omnidirectional radiation patterns. However, the antennas' bandwidths are usually narrow (less than 10%). Exciting multiple modes can broaden antennas' bandwidths [12, 13]. An electrically small and omnidirectional antenna with a bandwidth of 32% was presented [12]. Antenna arrays are usually used to extend bandwidth [14]. A circular dual-band monopole antenna array was designed in [14]. Omnidirectional DRAs have been designed in different shapes, including rectangles [15, 16], hemispheres [17], and cylinders [18–26]. A three-dimensional (3-D) printed omnidirectional multi-ring DRA was excited in three DR modes ($TM_{01\delta}$, $TM_{02\delta}$, and $TM_{03\delta}$ modes) with a bandwidth of 60.2% [24]. Combining a monopole antenna and a DRA is an effective way to realize an omnidirectional wideband antenna [27–30] at the expense of raising the profile. A hybrid antenna could

Submitted On: September 13, 2023
Accepted On: August 30, 2024

https://doi.org/10.13052/2024.ACES.J.391009

offer an impedance bandwidth of up to 138% [30]. Most existing works try to extend the bandwidth at the cost of increasing the antenna's dimensions [24] or sacrificing the stability of the radiation pattern [13, 30].

A coil feeding structure was first used in [19] to realize an omnidirectional cup dielectric resonator antenna (CDRA) with a 29.5% bandwidth. By improving the structure and the coil feeding mode, three modes are excited and the bandwidth reaches 67.7% with a stable omnidirectional pattern.

The modified coil feeding structure, with two ends excited equally and in phase, comprises four coil segments and two probes. The four coil segments have an equivalent magnetic-current loop and two probes act as a single monopole. Optimizing the coil and dielectric resonator (DR) parameters, the coil excites the $TM_{01\delta}$ mode of the CDRA and two omnidirectional modes (coil and monopole modes) at neighbor frequencies simultaneously. Thus, a wideband omnidirectional CDRA is achieved. Then, a prototype is fabricated and measured to demonstrate the scheme. The measured and simulated results are in reasonable agreement. The size of the CDRA is $0.61\,\lambda_0 \times 0.32\,\lambda_0$ (λ_0 is the free-space wavelength at the center frequency). The CDRA's bandwidth is 67.7% from 3.28 GHz to 6.64 GHz. Within the operating band, the CDRA has high radiation efficiencies, stable radiation patterns, and low cross polarizations. As listed in Table 1, the proposed antenna has a broader bandwidth and a smaller size.

Table 1: Comparison between proposed omnidirectional CDRA and relevant works first

Ref.	Antenna Types	Dimensions (Diameter × Height)	Bandwidth	Omnidirectional Pattern
[19]	DRA	$0.25\lambda_0 \times 0.23\lambda_0$	29%	Stable
[24]	Multi-ring DRA	$1.54\lambda_0 \times 0.18\lambda_0$	60%	Stable
[25]	DRA	$3.60\lambda_0 \times 0.11\lambda_0$	42%	Unstable
[26]	DRA	$1.00\lambda_0 \times 0.11\lambda_0$	34%	Stable
[30]	DRA + Monopole	$0.62\lambda_0 \times 0.66\lambda_0$	138%	Unstable
This Work	DRA	$0.61\lambda_0 \times 0.32\lambda_0$	68%	Stable

II. ANTENNA STRUCTURE

The CDRA's configuration is shown in Fig. 1. The cup dielectric (D_d, H_d, D_{in}, H_{in}) manufactured of K9-glass (ε_{rk}=6.9) is located on a circular substrate with

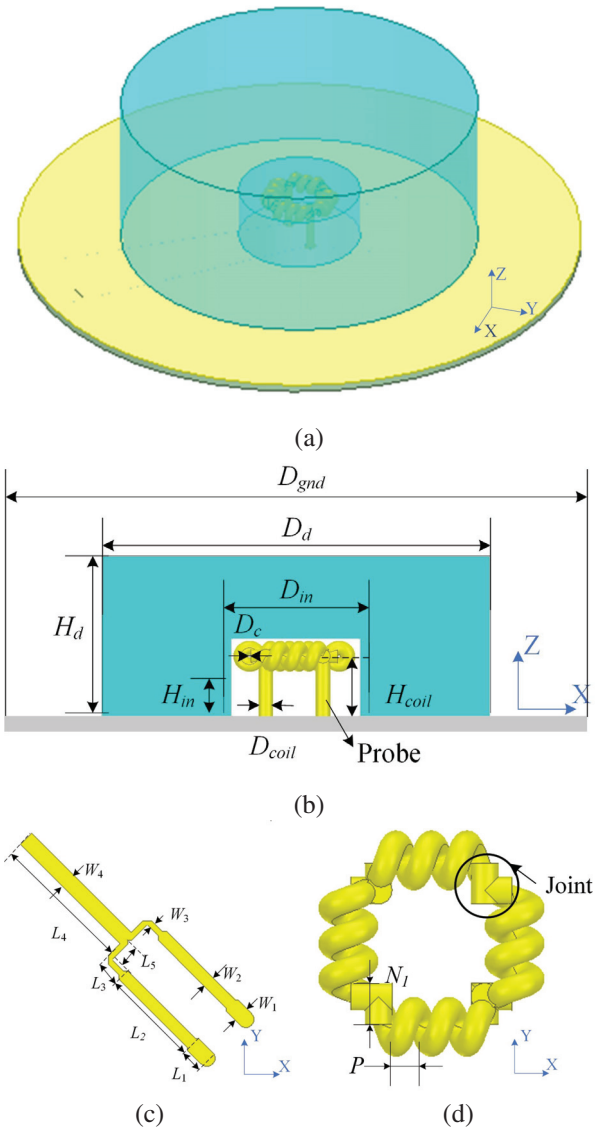

Fig. 1. CDRA: (a) isometric view and (b) front view. Top view of (c) T-junction power divider and (d) feeding structure.

a diameter of D_{gnd}, as can be seen in Fig. 1 (b). FR-4 (ε_{rf}=4.3) is the substrate material with a loss tangent of 0.025 and a thickness of 0.8 mm. The coil feeding structure is made of a copper wire with a diameter of D_{coil}. The coil's pitch, height, turns, and inner diameter are represented by H_{coil}, P, N, and D_c, respectively. As described in Fig. 1 (d), the joint length between the two coils is N_1. The T-junction power divider, as shown in Fig. 1 (c), is loaded on the dielectric surface side of the FR-4 substrate. All dimensions of the CDRA are listed in Table 2.

Table 2: Dimensions of the CDRA (unit: mm)

D_{gnd}	D_{in}	H_d	D_d	H_{in}	H_{coil}
60	14.6	16.5	37	5.6	5
D_{coil}	P	D_c	L_1	L_2	L_3
1	1.2	0.6	3	9.2	2
L_4	L_5	W_1	W_2	W_3	W_4
8	2.7	1.5	1.15	0.55	1.5
N	N_1				
3	1				

III. OPERATING MECHANISM

The basic coil, creating an equivalent magnetic-current loop, excites two modes (DR $TM_{01\delta}$ mode and coil mode) to realize an omnidirectional CDRA with a bandwidth of 29% [19]. Based on that, a modified coil excites an additional resonance (probe mode) to double the bandwidth of the CDRA. The evolution process of the CDRA can be divided into three steps.

Step 1: Introduce probe mode. In [19], the probes only support the coil to control the height of the coil. The probe lengths are short for the coil image to be close to the original coil. Thus, the equivalent magnetic-current loop and its image are very close to each other and constructively contribute to the increase of the antenna gain. The probes are elongated to enhance their influence. The increased diameter of the copper and shortened helical coil pitch are used to maintain the strength of the magnetic field. The probes' current directions change as the probes' length increases. The probes are excited equally and in phase to have their electrics in the same direction. However, the two probes excite the $HEM_{21\delta}$ mode of the DR, which undermines the omnidirectional property.

Step 2: Avoid exciting the $HEM_{21\delta}$ mode. As depicted in Fig. 2, the excited mode ($HEM_{21\delta}$ mode or monopole mode) is determined by the distance between the two probes. When the distance is short enough, the two probes are equivalent to a monopole, which excites an omnidirectional mode. The bending direction of the joint between two coils [as shown in Fig. 1 (d)] is reversed, and the helical coil pitch is decreased to shorten the distance. However, the probe resonance frequency is much higher than those of the coil and DR $TM_{01\delta}$ modes. Thus, a dual-band omnidirectional CDRA is observed.

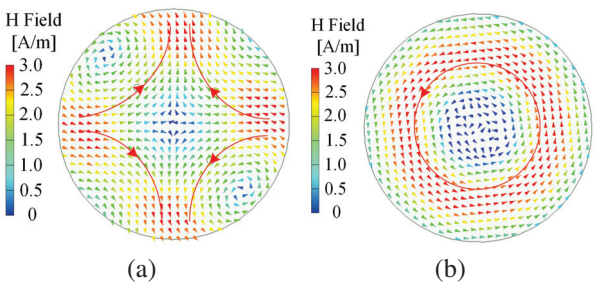

Fig. 2. Magnetic field of (a) $HEM_{21\delta}$ mode (the distance between two probes is 14.3 mm) and (b) monopole mode (the distance between two probes is 7.6 mm).

Step 3: Achieve a wideband omnidirectional CDRA. The resonance frequencies of the coil and probe modes are mainly affected by the coil. The $TM_{01\delta}$ mode's resonance increases with the larger size of the DR. Compared with the coil and probe modes, the $TM_{01\delta}$ mode's frequency is easy to control. The height of the DR rarely affects the frequency of the $TM_{01\delta}$ mode and influences the coupling between the coil and $TM_{01\delta}$ modes. Therefore, the diameter of the DR becomes larger to increase the $TM_{01\delta}$ mode's frequency. Finally, a wideband omnidirectional CDRA is designed.

The modified feeding structure, with two ends excited equally and in phase, is composed of four coil segments and two probes, as shown in Fig. 3. Given the current distribution of the coils, the winding direction of each side is reversed to achieve an equivalent magnetic-current loop. Two probes can be equivalent to a centered electric monopole. Thus, the modified coil can create a vertical monopole and a magnetic-current loop simultaneously. The monopole and the magnetic-current loop excite omnidirectional modes at the adjacent frequencies of the $TM_{01\delta}$ mode. Hence, the structure supports three modes with omnidirectional radiation providing wideband performance by the modified coil.

The simulated reflection coefficient of the CDRA is shown in Fig. 4 using the full-wave simulation software ANSYS HFSS. There are three distinct resonances within the operating bandwidth. Modes 1, 2, and 3 correspond to the coil, DR $TM_{01\delta}$, and probe modes

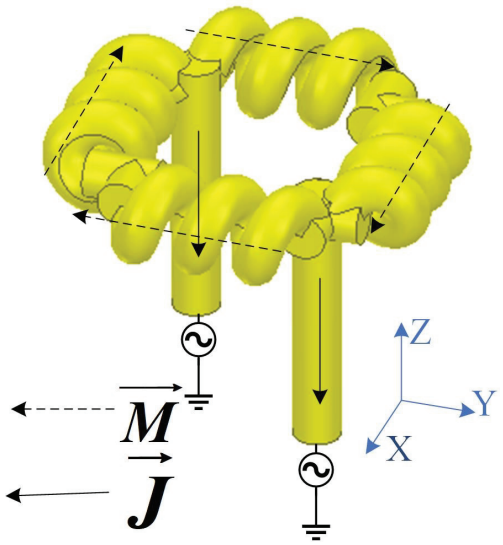

Fig. 3. Equivalent magnetic-current loop and monopole of a coil feeding structure.

at 3.65, 4.40, and 6.05 GHz, respectively. Mode analysis will be explained in Section IV. The simulated magnetic and electric fields at these frequencies are shown in Fig. 5. The magnetic and electric fields of the coil and probe modes are similar to that of $TM_{01\delta}$ mode.

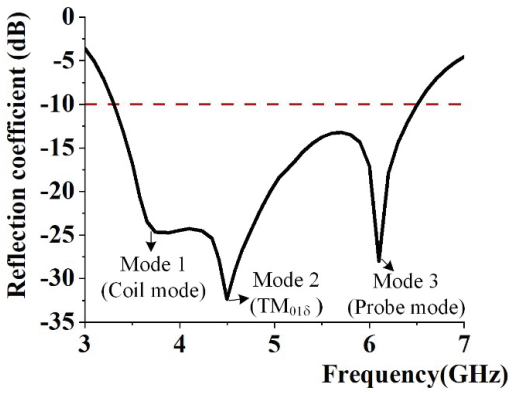

Fig. 4. Simulated reflection coefficient of the CDRA.

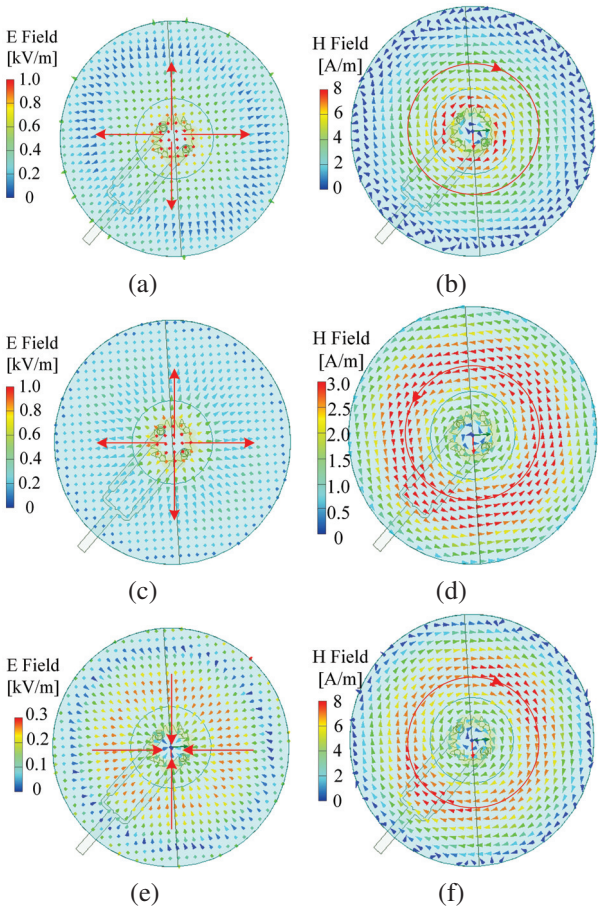

Fig. 5. Simulated electric field (a), (c), and (e) and magnetic field (b), (d), and (f) at 3.65, 4.40, and 6.05 GHz, respectively.

IV. PARAMETER STUDY

In this section, the antenna performances with different parameters are investigated by simulations. Firstly, the corresponding modes of three resonant frequencies are determined. Modes 1, 2, and 3 resonate at 3.65, 4.40, and 6.05 GHz, respectively. By exciting the cup DR with a single probe, the resonant frequency of the DR $TM_{01\delta}$ mode is 4.35 GHz, corresponding to the second resonant frequency. The reflection coefficients with different lengths of joint between two coils are shown in Fig. 6 (a). The length of the joint greatly influences the frequencies of modes 1 and 2, yet hardly affects the frequency of mode 3. Mode 3 corresponds to the monopole mode, and mode 1 corresponds to the coil mode.

Figure 6 (b) shows the reflection coefficients with different probe heights. As the probe gets longer, its corresponding resonant frequency gets lower. The probe height is the coil height from the ground plane, which decides the distance between the coil and the DR. Such height is related to the coupling between the DR and the equivalent magnetic-current loop, which obviously influences the impedance matching of the coil and DR $TM_{01\delta}$ modes. The reflection coefficients with different DR heights are shown in Fig. 6 (c). The probe resonant frequency is affected by the DR height. The resonant frequency of the monopole mode decreases as the DR height increases. The DR height has a negligible impact on the DR $TM_{01\delta}$ mode but a significant effect on the impedance matching of the coil mode. The DR

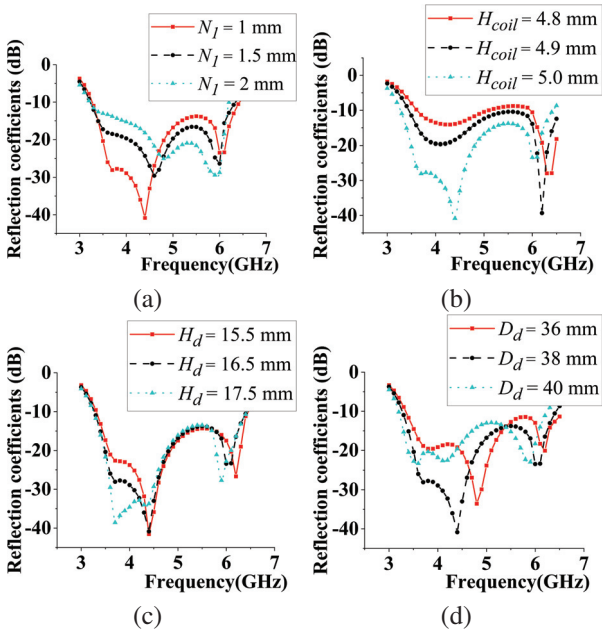

Fig. 6. Reflection coefficients versus antenna parameters: (a) length of joint N_1, (b) coil height H_{coil}, (c) dielectric height H_d, and (d) dielectric diameter D_d.

diameter is related to the frequencies of all the modes. The frequencies of the modes with smaller DR diameters are higher. Their corresponding reflection coefficients are shown in Fig. 6 (d). As a result of the coupling among the CDRA, the magnetic-current loop, and the monopole, the resonant frequencies of the DR $TM_{01\delta}$, coil, and monopole modes are interrelated.

V. RESULTS

A prototype of the CDRA is fabricated and measured as shown in Fig. 7. The CDRA is 37 mm $\times$ 20 mm ($0.61\lambda_0 \times 0.32\lambda_0$), while the cavity is 14.6 mm $\times$ 5.6 mm to house the coil. The ground plane is 900 mm^2. The coil feeding structure is fabricated using the 3D-printing approach.

The simulated and measured reflection coefficients of the CDRA are shown in Fig. 8. There are three distinct resonances within the operating bandwidth. The measured bandwidth of the CDRA (with $S_{11} \leq$ -10 dB) is more than 67.7% (3.28-6.64 GHz), which is sufficient for 5 GHz WLAN bands. The measured reflection coefficient is wider than the simulated one because of extra loss in the prototype. The 3-D printed coil has a fabrication tolerance of 0.1 mm and a rough surface, which mainly influences the coil mode's coupling.

Due to the limitation of the test equipment, the maximum test frequency is 6.5 GHz. The measured gain and efficiency are compared with the simulated in 3-6.5 GHz.

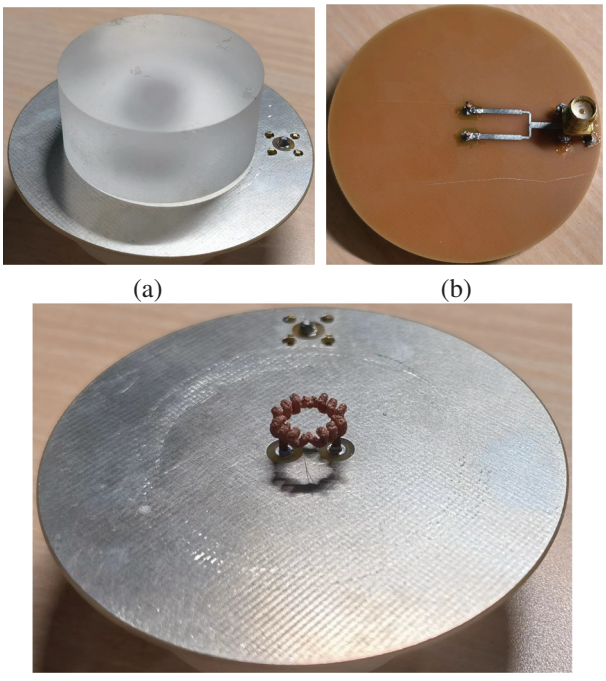

Fig. 7. Prototypes of CDRA: (a) isometric view, (b) bottom view, and (c) coil.

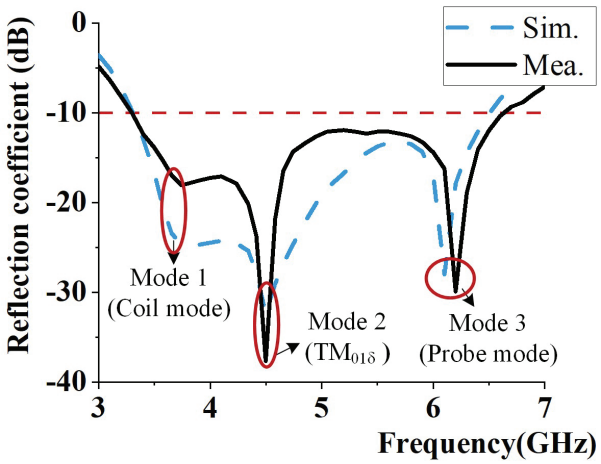

Fig. 8. Simulated and measured reflection coefficients of the CDRA.

As shown in Fig. 9, the simulated and measured efficiencies of the CDRA are better than 90% and 85%, respectively. The curves of gain are shown in Fig. 9. The gain variations of the CDRA are less than 1.5 dB in the operating band, which means the antenna has stable radiation patterns.

Figure 10 shows the simulated and measured radiation patterns in the xz- and xy-plane at 3.65, 4.40, and 6.05 GHz. As can be seen, the CDRA maintains stable omnidirectional radiation patterns and a low cross-polarization level within the operating band. The measured radiation efficiency is better than 80%, and the simulated one is better than 85% across the impedance passband. The measurements and simulations are in reasonable agreement, with the differences caused by measurement perturbation and manufacturing tolerance.

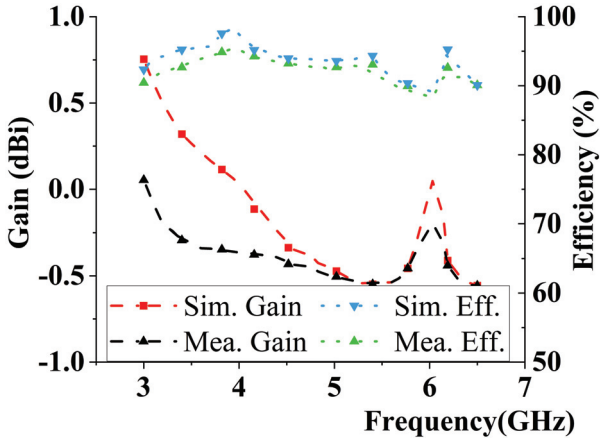

Fig. 9. Simulated and measured gains and efficiencies of the CDRA.

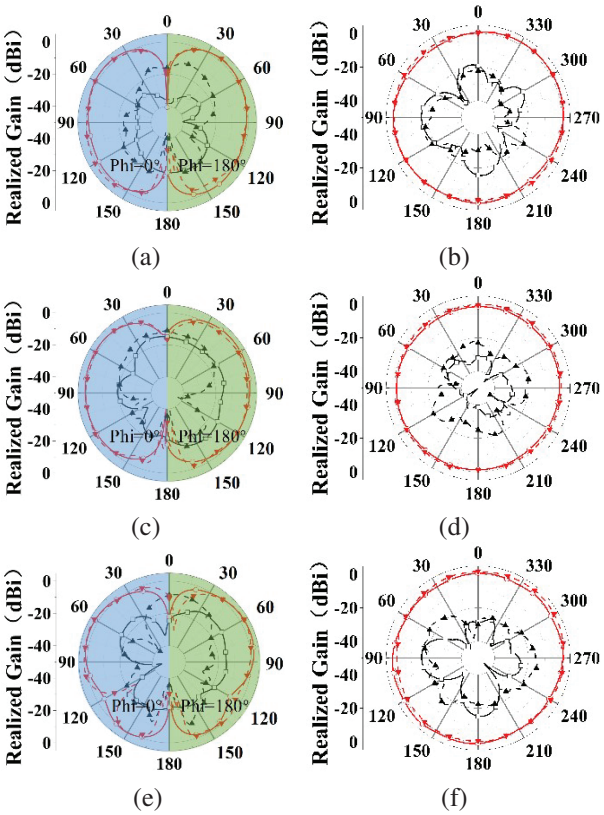

Fig. 10. Simulated and measured radiation patterns in x-z plane (a), (c), and (e) and x-y plane (b), (d), and (f) at 3.65, 4.40, and 6.00 GHz, respectively.

VI. CONCLUSION

A modified coil feeding structure has been used to realize an omnidirectional wideband CDRA with three resonant modes ($TM_{01\delta}$, coil, and monopole modes). The modified coil has been formed by combining four coil segments and two probes, which could create an equivalent magnetic-current loop and a monopole simultaneously. Using the proper DR dimensions and feeding structure has excited the DR $TM_{01\delta}$ mode and two omnidirectional modes (i.e., coil and monopole modes) at neighboring frequencies to realize an omnidirectional antenna with a 67.7% measured bandwidth (3.28-6.64 GHz). The CDRA has a diameter of $0.61\,\lambda_0$ and a height of $0.32\,\lambda_0$. The stable radiation patterns have been observed with high radiation efficiencies within the operating band.

REFERENCES

[1] K. W. Leung, E. H. Lim, and X. S. Fang, "Dielectric resonator antennas: From the basic to the aesthetic," *Proc. IEEE*, vol. 100, no. 7, pp. 2181-2193, July 2012.

[2] K. W. Leung, Y. M. Pan, X. S. Fang, E. H. Lim, K.-M. Luk, and H. P. Chan, "Dual-function radiating glass for antennas and light covers Part I: Omnidirectional glass dielectric resonator antennas," *IEEE Trans. Antennas Propag.,* vol. 61, no. 2, pp. 578-586, Feb. 2013.

[3] N. Yang and K. W. Leung, "Size reduction of omnidirectional cylindrical dielectric resonator antenna using a magnetic aperture source," *IEEE Trans. Antennas Propag.,* vol. 68, no. 4, pp. 3248-3253, Apr. 2020.

[4] M. Zou and J. Pan, "Investigation of resonant modes in wideband hybrid omnidirectional rectangular dielectric resonator antenna," *IEEE Trans. Antennas Propag.,* vol. 63, no. 7, pp. 3272-3275, July 2015.

[5] C. A. Balanis, *Antenna Theory: Analysis and Design*, Hoboken, NJ: Wiley, 2005.

[6] J. Huang, "Circularly polarized conical patterns from circular microstrip antennas," *IEEE Trans. Antennas Propag.,* vol. 32, no. 9, pp. 991-994, Sep. 1984.

[7] D. M. Kokotoff, R. B. Waterhouse, and J. T. Aberle, "An annular ring coupled to a shorted patch," *IEEE Trans. Antennas Propag.,* vol. 45, no. 5, pp. 913-914, May 1997.

[8] H.-T. Chen, H.-D. Chen, and Y.-T. Cheng, "Full-wave analysis of the annular-ring loaded spherical-circular microstrip antenna," *IEEE Trans. Antennas Propag.,* vol. 45, no. 11, pp. 1581-1583, Nov. 1997.

[9] Y. Yu, J. Xiong, and H. Li, "Compact omnidirectional circularly polarized antenna utilising bended dipoles and integrated baluns," *IET Microw. Antennas Propag.,* vol. 11, no. 10, pp. 1409-1414, July 2017.

[10] C. M. Wu, J. H. Choi, H. Lee, and T. Itoh, "Magnetic-current-loop-induced electric dipole antenna based on substrate integrated waveguide cavity," *IEEE Antennas Wireless Propag. Lett.,* vol. 13, pp. 519-522, Mar. 2014.

[11] A. Al-Zoubi, F. Yang, and A. Kishk, "A low-profile dual-band surface wave antenna with a monopole-like pattern," *IEEE Trans. Antennas Propag.,* vol. 55, no. 12, pp. 3404-3412, Dec. 2007.

[12] Y. Duan, M.-C. Tang, Z. Wu, Z. Zhang, D. Yi, and M. Li, "Omnidirectional-radiating, vertically polarized, wideband, electrically small filtenna," *IEEE Trans. Circuits Syst. II Exp. Briefs,* vol. 70, no. 4, pp. 1380-1384, Apr. 2023.

[13] Y. Feng, L.-K. Zhang, J.-Y. Li, Y.-H. Yang, S.-G. Zhou, and X.-J. Yu, "A compact share-aperture antenna with pattern/polarization diversity for 5G sub-6G applications," *IEEE Trans. Circuits Syst. II Exp. Briefs*, vol. 70, no. 3, pp. 954-958, Mar. 2023.

[14] D. D. Patil, K. S. Subramanian, and N. C. Pradhan, "3D-printed dual-band rectenna system for green IoT application," *IEEE Trans. Circuits Syst. II Exp. Briefs*, vol. 70, no. 8, pp. 2864-2868, Aug. 2023.

[15] Y. M. Pan and K. W. Leung, "Wideband omnidirectional circularly polarized dielectric resonator antenna with parasitic strips," *IEEE Trans. Antennas Propag.*, vol. 60, no. 6, pp. 2992-2997, June 2012.

[16] C. Wang, Z. Han, H. Liu, P. Wen, L. Wang, and X. Zhang, "A novel single-feed filtering dielectric resonator antenna using slotline stepped-impedance resonator," *IEEE Trans. Circuits Syst. II Exp. Briefs,* vol. 68, no. 11, pp. 3426-3430, Nov. 2021.

[17] D. Guha, B. Gupta, C. Kumar, and Y. M. M. Antar, "Segmented hemispherical DRA: New geometry characterized and investigated in multi-element composite forms for wideband antenna applications," *IEEE Trans. Antennas Propag.,* vol. 60, no. 3, pp. 1605-1610, Mar. 2012.

[18] S. H. Ong, A. A. Kishk, and A. W. Glisson, "Rod-ring dielectric resonator antenna," *Int. J. Rf. Microw. C. E.*, vol. 14, no. 5, pp. 441-446, Sep. 2004.

[19] S. Zheng, Z.-Y. Zhang, X. Chen, and A. A. Kishk, "Wideband monopole-like cup dielectric resonator antenna with coil feeding structure," *IEEE Trans. Antennas Propag.*, vol. 70, no. 8, pp. 7118-7123, Aug. 2022.

[20] N. Yang, K. W. Leung, K. Lu, and N. Wu, "Omnidirectional circularly polarized dielectric resonator antenna with logarithmic spiral slots in the ground," *IEEE Trans. Antennas Propag.,* vol. 65, no. 2, pp. 839-844, Feb. 2017.

[21] M. H. Seko and F. S. Correra, "Excitation of dielectric resonator antennas by loop coupling," *IEEE Antennas Wireless Propag. Lett.*, vol. 18, no. 4, pp. 656-658, Apr. 2019.

[22] W. Li, K. W. Leung, and N. Yang, "Omnidirectional dielectric resonator antenna with a planar feed for circular polarization diversity design," *IEEE Trans. Antennas Propag.,* vol. 66, no. 3, pp. 1189-1197, Mar. 2018.

[23] W. W. Li and K. W. Leung, "Omnidirectional circularly polarized dielectric resonator antenna with top-loaded Alford loop for pattern diversity design," *IEEE Trans. Antennas Propag.,* vol. 61, no. 8, pp. 4246-4256, Aug. 2013.

[24] Z.-X. Xia, K. W. Leung, and K. Lu, "3-D-printed wideband multi-ring dielectric resonator antenna," *IEEE Antennas Wireless Propag. Lett.*, vol. 18, no. 10, pp. 2110-2114, Oct. 2019.

[25] H. Tang, L. Wu, D. Ma, H. Li, J. Huang, X. Deng, J. Zhou, and J. Shi, "Wideband filtering omnidirectional substrate-integrated dielectric resonator antenna covering Ku band," *IEEE Antennas Wireless Propag. Lett.*, vol. 22, no. 7, pp. 1746-1750, July 2023.

[26] X. S. Fang, L. P. Weng, and Z. Fan, "Design of the wideband and low-height omnidirectional cylindrical dielectric resonator antenna using arced-apertures feeding," *IEEE Access*, vol. 11, pp. 20128-20135, 2023.

[27] M. Lapierre, Y. M. M. Antar, A. Ittipiboon, and A. Petosa, "Ultra-wideband monopole/dielectric resonator antenna," *IEEE Microw. Wireless Compon. Lett.*, vol. 15, no. 1, pp. 7-9, Jan. 2005.

[28] K. S. Ryu and A. A. Kishk, "UWB dielectric resonator antenna having consistent omnidirectional pattern and low cross-polarization characteristics," *IEEE Trans. Antennas Propag.,* vol. 59, no. 4, pp. 1403-1408, Apr. 2011.

[29] D. Guha, B. Gupta, and Y. Antar, "Hybrid monopole-DRAs using hemispherical/conical-shaped dielectric ring resonators: Improved ultrawideband designs," *IEEE Trans. Antennas Propag.,* vol. 60, no. 1, pp. 393-398, Jan. 2012.

[30] C. Ozzaim, F. Ustuner, and N. Tarim, "Stacked conical ring dielectric resonator antenna excited by a monopole for improved ultrawide bandwidth," *IEEE Trans. Antennas Propag.,* vol. 61, no. 3, pp. 1435-1438, Mar. 2013.

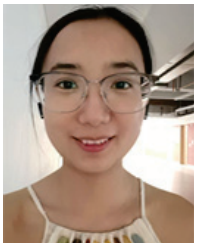

Shuxin Zheng received the B.Sc. degree in electronics and information engineering from Xi'an Jiaotong University, Xi'an, China, in 2021, where she is currently pursuing the Ph.D. degree in electronics science and technology from Xi'an Jiaotong University, Xi'an. Her current research direction is antenna design.

Nan Yang received the B.Sc. and M.Eng. degrees in electronic engineering from Zhejiang University (ZJU), Hangzhou, China, in 2008 and 2012, respectively, and the Ph.D. degree from the City University of Hong Kong, Hong Kong, in 2016. He was a Post-Doctoral Fellow with the City University of Hong Kong from 2016 to 2020. He is currently an Associate Professor with the School of Electronics and Information Technology (School of Microelectronics), Sun Yat-sen University (SYSU), Guangzhou, China. His current research interests include

dielectric resonator antennas, lens antennas, multiple-input-multiple-output (MIMO) antennas, transparent antennas, and microwave and millimeter-wave circuits.

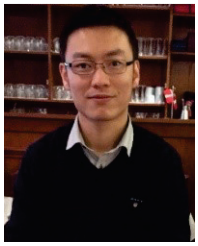

Xiaoming Chen received the B.Sc. degree in electrical engineering from Northwestern Polytechnical University, Xi'an, China, in 2006, and M.Sc. and PhD degrees in electrical engineering from Chalmers University of Technology, Gothenburg, Sweden, in 2007 and 2012, respectively. From 2013 to 2014, he was a postdoctoral researcher at the same University. From 2014 to 2017, he was with Qamcom Research & Technology AB, Gothenburg, Sweden, Since 2017, he has been a professor at Xi'an Jiaotong University, Xi'an, China. His research areas include 5G multi-antenna techniques, over-the-air (OTA) testing, and reverberation chambers.

Zhen-Yuan Zhang received the B.S. degree in electronic science and engineering from the Nanjing University of Posts and Communications, Nanjing, China, in 2011, and the M.S. and Ph.D. degrees from The Chinese University of Hong Kong, Hong Kong, in 2013 and 2019, respectively. Currently, he is a Post-Doctoral Fellow with the Southern University of Science and Technology, Shenzhen, China. His current research interests include circularly polarized antenna design, wideband base station antenna design, and antenna break decoupling techniques.

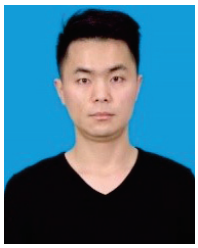

Bingyi Qian received the B.S. degree in electronics and information engineering from Xidian University, Xi'an, China, in 2020, where he is currently pursuing the Ph.D. degree in electronics science and technology from Xi'an Jiaotong University, Xi'an. His current research interests include microstrip antenna design, mutual coupling reduction and 5G mobile antennas.

Ahmed A. Kishk received the Ph.D. degree from the University of Manitoba, Winnipeg, MB, Canada, in 1986. In 1986, he joined the University of Mississippi, Oxford, MS, USA, first as an Assistant Professor and then a Professor. Since 2011, he has been a Professor and a Tier 1 Canada Research Chair in advanced antenna systems with Concordia University, Montreal, QC, Canada. He has published over 340 refereed journal articles and 450 conference papers. He is a co-author of four books and several book chapters, and an editor of three books. His research interest includes millimeter-wave antennas, beamforming networks, dielectric resonator antennas, microstrip antennas, and electromagnetic band gap (EBG).

Wideband Wide-angle SSPP-fed Leaky-wave Antenna with Low Side-lobe Levels

Yanzhen Shi[1], Zhibo Fan[1], Cong Chen[2], and Yongjin Zhou[1, 3]

[1]Key Laboratory of Specialty Fiber Optics and Optical Access Networks
School of Communication and Information Engineering, Shanghai University, Shanghai 200444, China
yanzhen_shi@163.com, fzbyuuna@shu.edu.cn, yjzhou@shu.edu.cn

[2]Electronic Information School
Wuhan University, Wuhan 430072, China
chencong@whu.edu.cn

[3]Shaanxi Key Laboratory of Artificially-Structured Functional Materials and Devices
Air Force Engineering University, Xi'an 710051, China

Abstract – In this paper, a broadband wide-angle leaky-wave antenna (LWA) with low sidelobe levels (SLL) is proposed. The antenna is composed of two parts: a broadband wide-angle scanning spoof surface plasmon polariton (SSPP)-fed circular patch antenna array and electromagnetic bandgap (EBG) structures tiled on both sides of the antenna array. By controlling the coupling distances between the circular radiation patches and SSPP feeding line, the attenuation constant along the radiation aperture is specially designed in a tapered way to achieve low SLL. EBG structures are adopted to reduce the back-lobe levels. Measured results show that the scanning angle of the proposed antenna reaches 82°. The measured realized gains are from 8 to 15.7 dBi in the operating frequency range from 8 to 12 GHz, with a maximum SLL less than -15 dB. The wide-band wide-angle SSPP-fed LWA with low SLL can find applications in radar detection and microwave imaging.

Index Terms – Electromagnetic bandgap (EBG), leaky-wave antenna (LWA), low side-lobe levels (SLL), surface plasmon polaritons (SPP), wide-angle.

I. INTRODUCTION

Leaky-wave antennas (LWAs) typically generate leaky-wave radiation by gradually leaking electromagnetic (EM) energy along the structure, which are often used in radar detection and microwave imaging as a kind of frequency scanning antenna [1, 2]. To detect low altitude, slow speed, and small aircraft targets, LWAs usually require a wide scanning angle. To implement ground clutter suppression, the radar system also requires an antenna with low sidelobe levels (SLL). Spoof surface plasmon polariton (SSPP) refers to surface EM modes formed on the metal surface at microwave and terahertz frequencies [3–6], which can be employed to increase the beam scanning angle of LWAs. Periodically-modulated plasmonic waveguides have been developed to convert SSPPs to radiating waves and achieve frequency scanning antenna radiation from forward to backward directions in [7], which achieved a scanning angle of 18° from 8.5 to 9.8 GHz. An SSPP-fed antenna array enables a larger scanning angle [8, 9]. In [8], an SSPP-fed circular patch array antenna was proposed, achieving a scanning angle of 55° from 5 to 11 GHz. By adopting double-layer coupled SSPP feeding structures, a broader impedance bandwidth and larger scanning angle have been achieved [10, 11]. In [10], a circular patch array antenna fed by SSPP was proposed and implemented a scanning angle of 68° operated in 11-15 GHz. However, the mentioned SSPP LWAs suffer from high SLL (>-10 dB) when the scanning angle is large.

Different kinds of methods have been proposed and applied to LWAs to reduce SLL, including changing the size of radiating elements [12–14], adjusting the density of radiating elements [15], and controlling the distance between the radiating elements and the feeding line [16–18]. In [12, 13], the leakage amount of the LWA is controlled by changing the length and width of slots, achieving a SLL below -20 dB. A SLL below -15 dB is implemented by adjusting the deviation angle of slots in a transverse slot array antenna [14], but its scanning angle is only 2.9°. By changing the density of transverse slots to control the amplitude of the aperture field distribution, a SLL of -20 dB within a scanning range of 31° has been achieved [15]. The most common method is to control the distance between slots or patches and the feeding line to regulate the leakage of EM energy [16–18]. In [17], by controlling the distance between the long slot and via hole arrays, a SLL of -20 dB is achieved within a range

Submitted On: May 17, 2023
Accepted On: October 15, 2024
https://doi.org/10.13052/2024.ACES.J.391010

of 18.6°. Although these works can achieve low SLL, they suffer from a relatively narrow relative bandwidth (<30%) and limited scanning range (<40°).

In this paper, a broadband, wide-angle, and low SLL SSPP-fed LWA is proposed. The SSPP-fed circular patch antenna array's distinct tapered aperture field distribution effectively reduces the SLL, while the electromagnetic bandgap (EBG) structure evenly dispersed along both sides of the antenna minimizes the back-lobe levels of the antenna. In the operating frequency range from 8 to 12 GHz, the measured scanning angle is 82°, with a gain fluctuation from 8 to 15.7 dBi and a maximum SLL less than -15 dB. The frequency beam scanning antenna supports radar detection of low-altitude, slow-speed, and miniaturized targets.

II. ANALYSIS AND DESIGN

A. Design of SSPP antenna

Figure 1 presents the proposed SSPP antenna's configuration. Theta is defined as the angle between the radiation beam and the $+z$ direction and phi is defined as the angle between the radiation beam and the $+x$ direction. The antenna is made up of two F4B ($\varepsilon_r = 2.65$ and $tan\,\delta = 0.001$) substrate layers (Sub1 and Sub2) and three metallic layers. The SSPP feeding line etched on Sub2 ($h_1 = 1.5$ mm) is shown in Fig. 1 (b). The radiating circular patches are etched on the top of Sub2 ($h_2 = 0.5$ mm) illustrated in Fig. 1 (c). The width of Sub1 and Sub2 is l_y. The length of Sub1 is 12 mm shorter than Sub2, leaving gaps for welding ports. There are 24 circular radiation patches arranged in a row. The space between adjacent patches is d. The distance between the circular patch's center and the SSPP line's bottom is set to d_n. The period of SPP unit is p. The groove width is a and the depth of SSPP unit is h. Transition parts are arranged between the SSPP units and the microstrip line to achieve an efficient modes transition where the groove depth varies from 0 to h in gradient. The radius r of the circular patch is 4.5 mm, which corresponds to the radius in TM_{11}-mode, which can be determined by:

$$r = \frac{1.8412c}{2\pi f_0 \sqrt{\varepsilon_r}}, \tag{1}$$

where c is the velocity of light in free space.

The dispersion characteristics of the SSPP units were analyzed using CST software, as shown in Fig. 2 (a). β is the propagation constant of the SSPP line. The results in Fig. 2 (a) demonstrate that the value of the groove depth h affects the curve's cut-off frequency. Because the cut-off frequency decreases as h grows, its constraint ability grows stronger as h increases. A groove depth of $h = 2.2$ mm is selected here. The width of the microstrip line is ws, and the impedance is approximately 50 Ω. The SSPP feeding line is etched on Sub2 with a length of $l_z = 320$ mm, and the transmission performance is analyzed. The scattering (S) parameter performance of the SSPP feeding line obtained through simulation is shown in Fig. 2 (b). In the operating frequency from 8 to

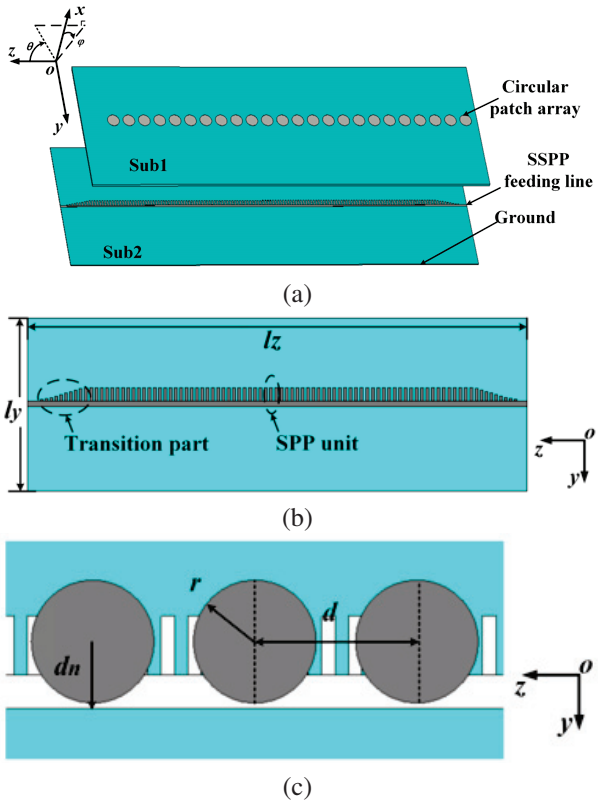

Fig. 1. Geometry of the proposed LWA: (a) perspective view, (b) top view of SSPP feeding line layer, and (c) zoomed top view ($l_z = 320$ mm, $l_y = 100$ mm, $d = 12$ mm, $d_n = 5$ mm, $r = 4.5$ mm).

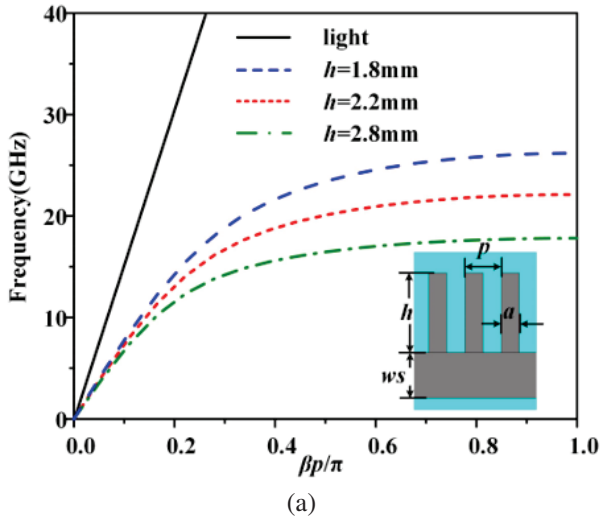

Fig. 2. *Continued.*

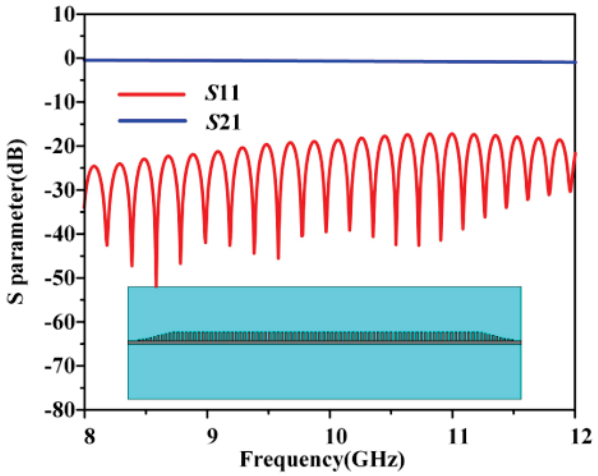

(b)

Fig. 2. Performance of the SSPP unit and the SSPP transmission line: (a) dispersion curves of the SSPP unit (inset is the geometry of the SSPP unit) and (b) simulated S parameters of the SSPP feeding line ($h = 2.2$ mm, $ws = 1.26$, $p = 1$ mm, $a = 0.5$ mm).

12 GHz, the reflection coefficients are less than -20 dB and the transmission coefficients are between 0 and -2 dB, which proves that the SSPP line has good transmission characteristics.

The relative distance between the centerline of the circular patches and the SSPP line determines the coupling strength, which can be adjusted by modifying the parameter d_n. Figure 3 shows the simulated S parameters of the antenna at different coupling distances d_n at 10 GHz. Within the entire operating frequency band,

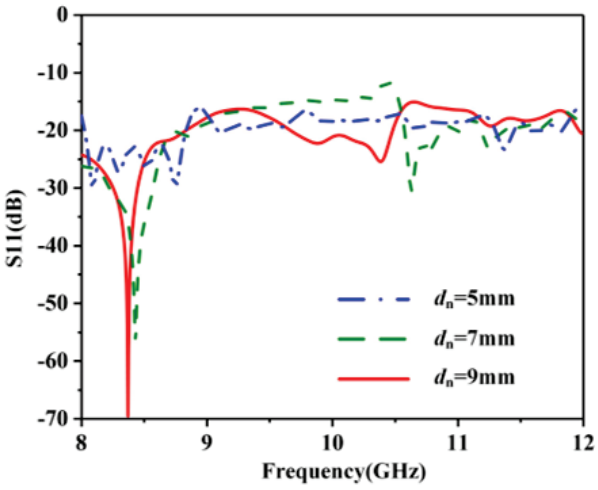

(a)

Fig. 3. *Continued.*

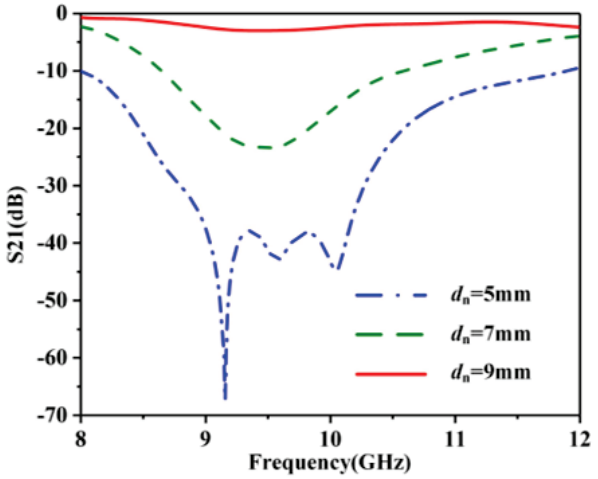

(b)

Fig. 3. Simulated S parameters of the antenna with different d_n values: (a) S_{11} and (b) S_{21}.

the reflection coefficient S_{11} is less than -10 dB, and the transmission coefficient S_{21} of $d_n = 5$ mm is less than -10 dB from 8 to 12 GHz. As d_n increases, the value of S_{21} significantly increases, indicating more energy being transmitted to the end of the antenna due to weaker coupling strength.

The SSPP-fed circular patch array antenna has a wide bandwidth and stable radiation pattern without increasing the antenna area. Figure 4 shows the radiation pattern of the SSPP antenna when the coupling distance d_n is 5 mm. It can be seen that the proposed SSPP antenna achieves a scanning range of 36° to 118° (phi = 0°) in the bandwidth from 8 to 12 GHz. The radia-

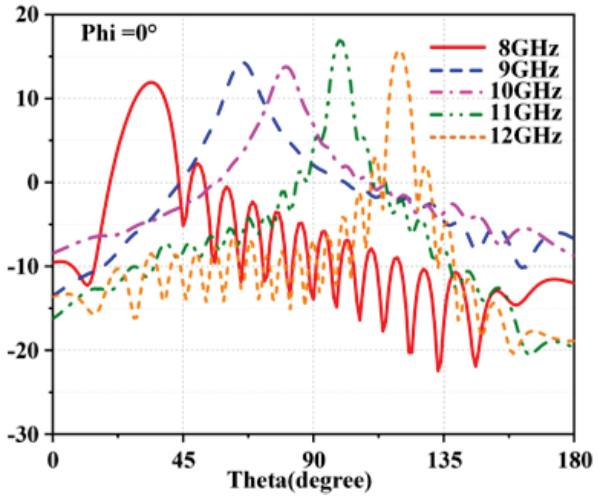

(a)

Fig. 4. *Continued.*

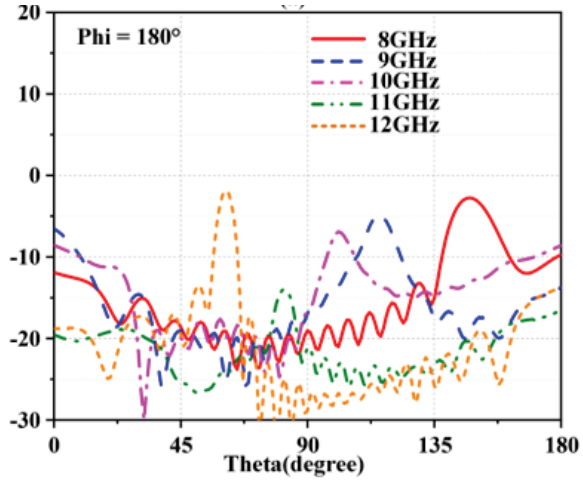

(b)

Fig. 4. Radiation pattern of LWA with $d_n = 5$ mm in (a) phi $= 0°$ and (b) phi $= 180°$.

tion gain is above 12 dBi. From the simulation results, the designed SSPP antenna has a high SLL throughout the operating frequency band, with a maximum SLL of -9 dB. For example, the reason for the decrease in gain at 10 GHz is that a uniform aperture field distribution results in a wider half-power beamwidth (HPBW) and high SLL. Next, we will adjust the coupling distance d_n of different radiation patches to achieve tapered aperture field distribution to implement low SLL.

B. Design of low SLL

For low SLL designs, it is necessary to adjust the aperture field distribution on the antenna surface. The attenuation constant corresponding to the aperture field distribution can be calculated to determine the coupling distance. Aperture field distribution $E(z)$ and the attenuation constant distribution $\alpha(z)$ has the following relationship [19]:

$$\alpha(z) = \frac{(1/2)|E(z)|^2}{(1/(1-R))\int_0^{l_z}|E(\zeta)|^2 d\zeta - \int_0^{l}|E(\zeta)|^2 d\zeta}, \tag{2}$$

where R represents the ratio of power absorbed by the terminal load, while l is the distance from the antenna's origin to the point under concern. R can be calculated by:

$$R = |S_{21}|^2. \tag{3}$$

In equation (2), the value of R varies with the aperture field distribution, which can be set to the average of the values obtained under different coupling distances. For the specific antenna structure, where $l_z = 320$ mm and d_n varies from 5 to 11 mm, R is set to the average value of 0.5.

According to [16, 20], when the aperture field distribution $E(z)$ of a leaky wave antenna follows the cosine distribution along the z-direction, the antenna will have a low SLL. Consequently, the same distribution is applied to the aperture field here, which can be expressed as [16]:

$$E(z) = 1.5\cos\left(\frac{\pi}{l_z}z - \frac{\pi}{2}\right) + 2. \tag{4}$$

Substituting equation (4) into equation (2) can obtain the distribution of the attenuation constant over the antenna length under the cosine aperture field distribution, as shown in Figs. 5 (a) and (b).

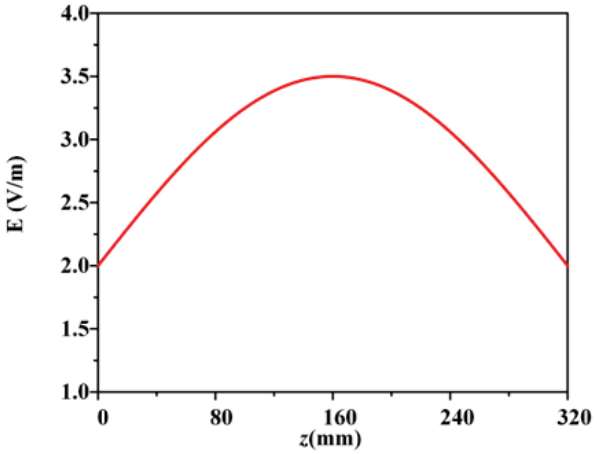

(a)

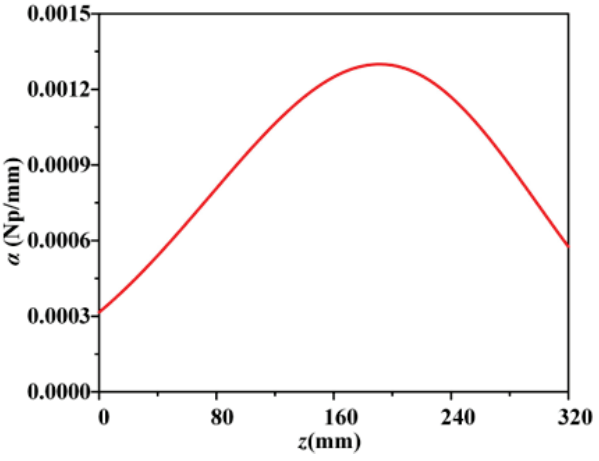

(b)

Fig. 5. Distribution of (a) $E(z)$ and (b) $\alpha(z)$.

For a uniform traveling wave structure, the attenuation constant can be calculated from S parameters of the structure by the formula:

$$\alpha = -\frac{|S_{21}|}{l_z}. \tag{5}$$

The unit α in the equation is dB/mm. To obtain α represented by Np per unit length, the expression 1 Np = 8.686 dB is used. Figure 3 (b) gives the transmission coefficients corresponding to different coupling

distances d_n. By combining equation (5), we can obtain the relationship between coupling distance and attenuation constant, as shown in Fig. 6 (a). Therefore, combining equations (2) and (5) can indirectly obtain the relationship between aperture field $E(z)$ and coupling distance d_n, as shown in Fig. 6 (b). This helps to design the desired aperture field distribution.

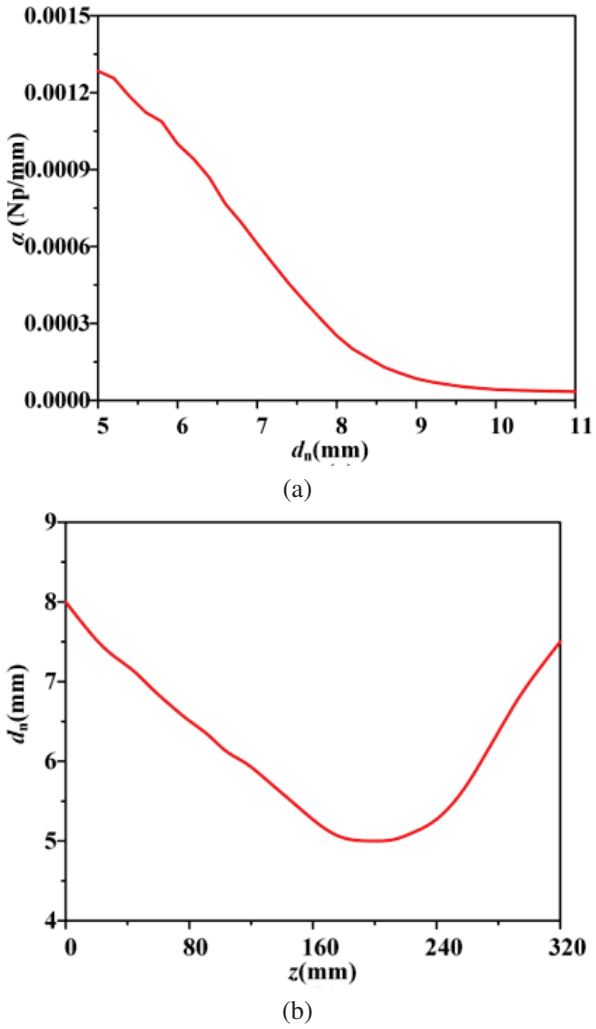

Fig. 6. (a) Variations of attenuation constant as functions of d_n and (b) variation of d_n along z-axis.

According to the generated curve of Fig. 6 (b), the positions of radiation patches have been rearranged. The patches at various positions were optimized in EM simulation software, to implement as low SLL as possible throughout the entire X-band (from 8 to 12 GHz). The coupling distance between the patch array and the SSPP line has been optimized according to appropriate proportional multiples. Table 1 shows the final optimized coupling distance.

Table 1: The optimized values of 24 patches' coupling distance (unit: mm)

Parameter	Value	Parameter	Value
d_1	11.5	d_{13}	5.52
d_2	10.98	d_{14}	5
d_3	10.59	d_{15}	5
d_4	9.94	d_{16}	5
d_5	9.42	d_{17}	5
d_6	8.9	d_{18}	5
d_7	8.51	d_{19}	5.52
d_8	7.86	d_{20}	6.56
d_9	7.6	d_{21}	7.6
d_{10}	7.08	d_{22}	8.12
d_{11}	6.56	d_{23}	8.64
d_{12}	6.04	d_{24}	9.16

Figures 7 (a) and (b) show the top view of the SSPP antenna with uniform $d_n = 5$ mm (Antenna A) and the SSPP antenna with optimized d_n (Antenna B). Figures 7 (c) and (d) illustrate the far-field radiation patterns following the implementation of the low SLL design. It can be seen that compared with Antenna A, the first sidelobe at 10 GHz of Antenna B is decreased from -11.8 to -29.4 dB and the first sidelobe at 12 GHz is decreased from -12.2 to -24.3 dB. The results indicate that this method is feasible. However, we can observe the antenna's back-lobe level remains significantly higher than -15 dB at low frequencies, specifically at 8 GHz. Hence, we need to further implement low back-lobe level.

C. Design of low back-lobe level

From Fig. 7 (c), we can see that the back-lobe level at 8 GHz is still high due to the existence of surface waves, dispersing the energy radiated along the main direction and increasing the SLL of the SSPP antenna. EBG is a stopband structure used to reduce the energy coupling between antennas [21]. Mushroom-shaped EBG is the most commonly used structure [22]. They are often used in antennas to prevent the propagation of surface waves, achieve a gain enhancement, and reduce the SLL of antennas. Therefore, a mushroom-shaped EBG structure is introduced to suppress surface waves, as shown in Figs. 8 (a) and (b). The EBG metasurface is composed of a metal ground, a dielectric substrate (F4B), a square patch, and metal via holes inside the dielectric substrate. The unit of the metal patch is connected to the grounding plate on the other side of the dielectric substrate through the metal via hole.

This structure can exhibit high impedance performance within the operating frequency band, suppressing surface waves on the substrate of the antenna. By using the waveguide transmission method shown in Fig. 8 (c),

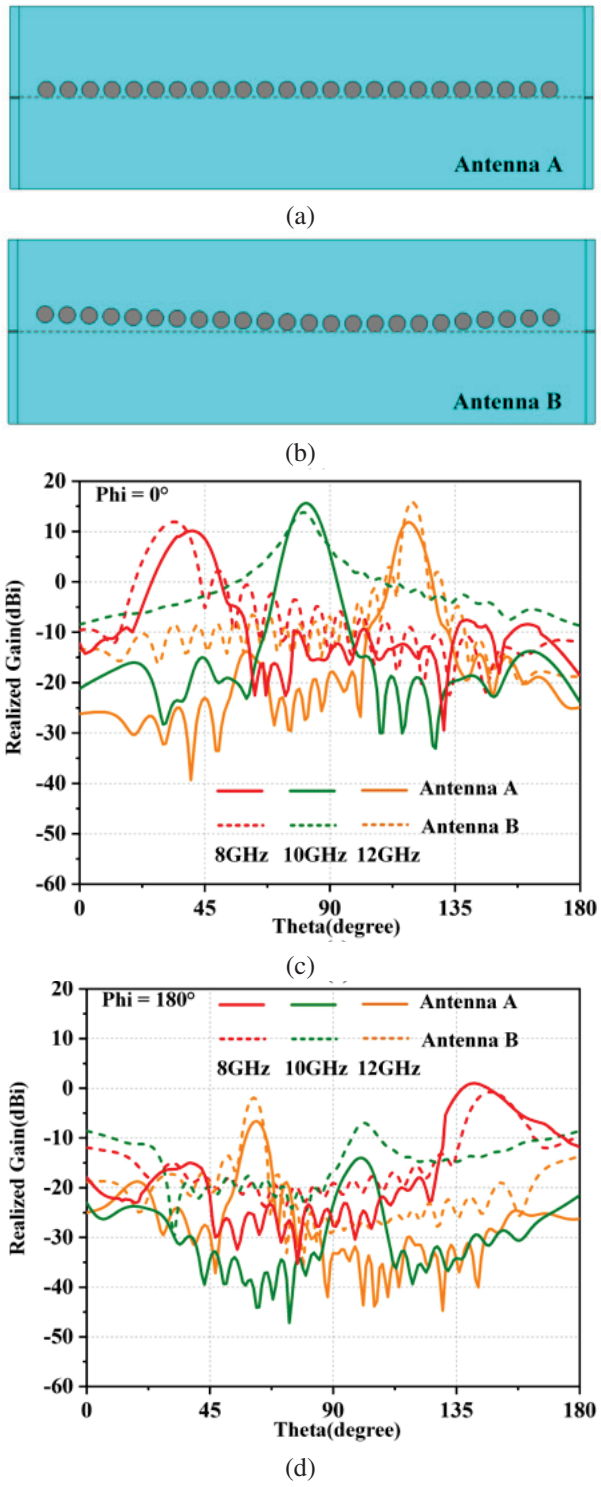

Fig. 7. (a) Antenna A with uniform $d_n = 5$ mm, (b) antenna B with optimized d_n, (c) radiation pattern of the two antennas in phi = 0° at 8, 10, 12 GHz, and (d) radiation pattern of the two antennas in phi = 180° at 8, 10, 12 GHz.

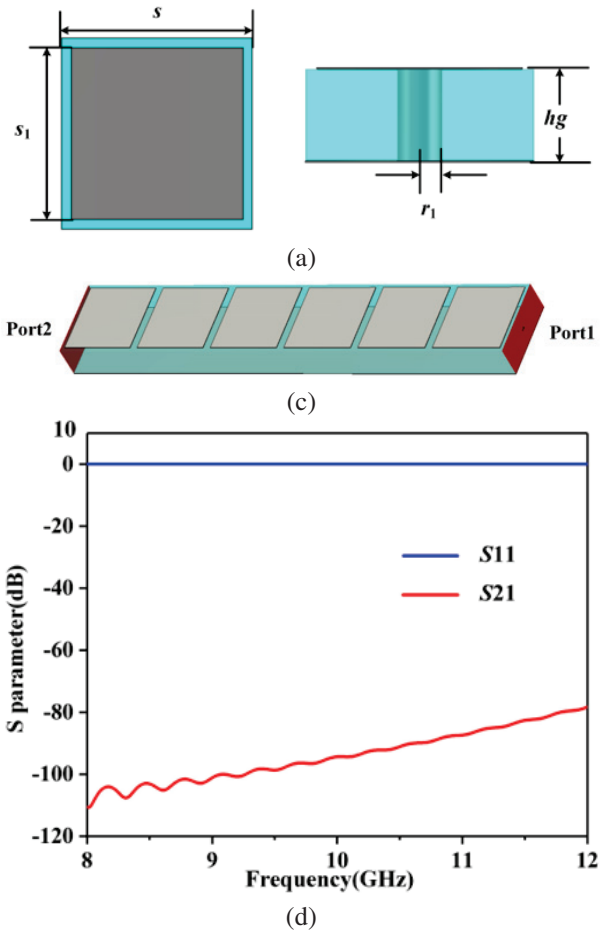

Fig. 8. (a) Top view of the EBG unit, (b) side view of the EBG unit, (c) 3-D view of the proposed EBG structure, and (d) S parameters of the proposed EBG structure ($s_1 = 4.5$ mm, $s = 5$ mm, $r_1 = 0.5$ mm, $hg = 2$ mm).

the simulated results in Fig. 8 (d) show its stopband effect reaches -80 dB in the X-band.

Figures 9 (a) and (b) illustrate the geometry of the designed antenna. The simulated results of the far-field radiation pattern at 8 GHz is shown in Figs. 9 (c) and (d). It can be seen that the back-lobe level of the antenna with EBG has decreased from -10.8 to -16.8 dB, which indicates that the back-lobe level reduction can be achieved by loading EBG structures on both sides of the antenna.

The simulation results of the LWA antenna with low SLL design are shown in Fig. 10. From Fig. 10 (a), it can be seen that the operating frequency band still covers the X-band. The simulated radiation efficiency of LWAs without low SLL design and with low SLL design is shown in Fig. 10 (b). The maximum radiation efficiency

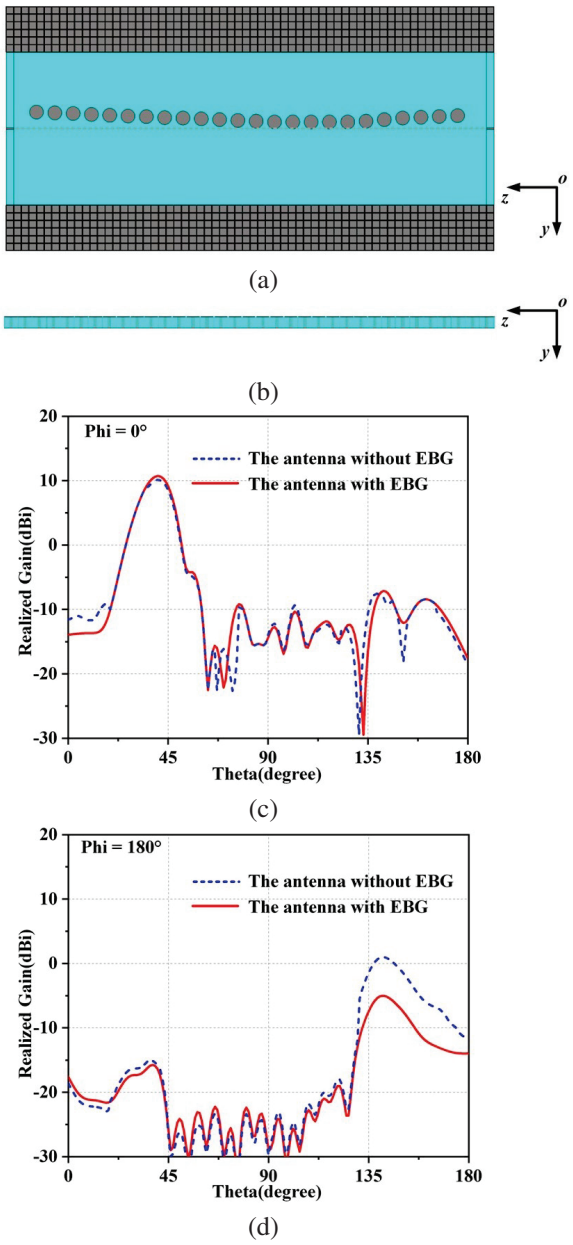

Fig. 9. (a) Top view of the antenna with EBG, (b) side view of the antenna with EBG, (c) radiation pattern of the antenna in phi = 0° at 8 GHz, and (d) radiation pattern of the antenna in phi = 180° at 8 GHz.

of LWAs without low SLL design and with low SLL design is 95.8% and 92.4%, respectively. The proposed LWA with low SLL design has a radiation efficiency of approximately 83.6% in the working band. Simulated radiation patterns are shown in Figs. 10 (c) and (d), which shows that the antenna has a scanning angle range of 32° to 114° (phi = 0°) from 8 to 12 GHz, and the highest SLL in the entire frequency band is less than -15 dB. The optimal SLL can reach approximately -23 dB at 10 GHz.

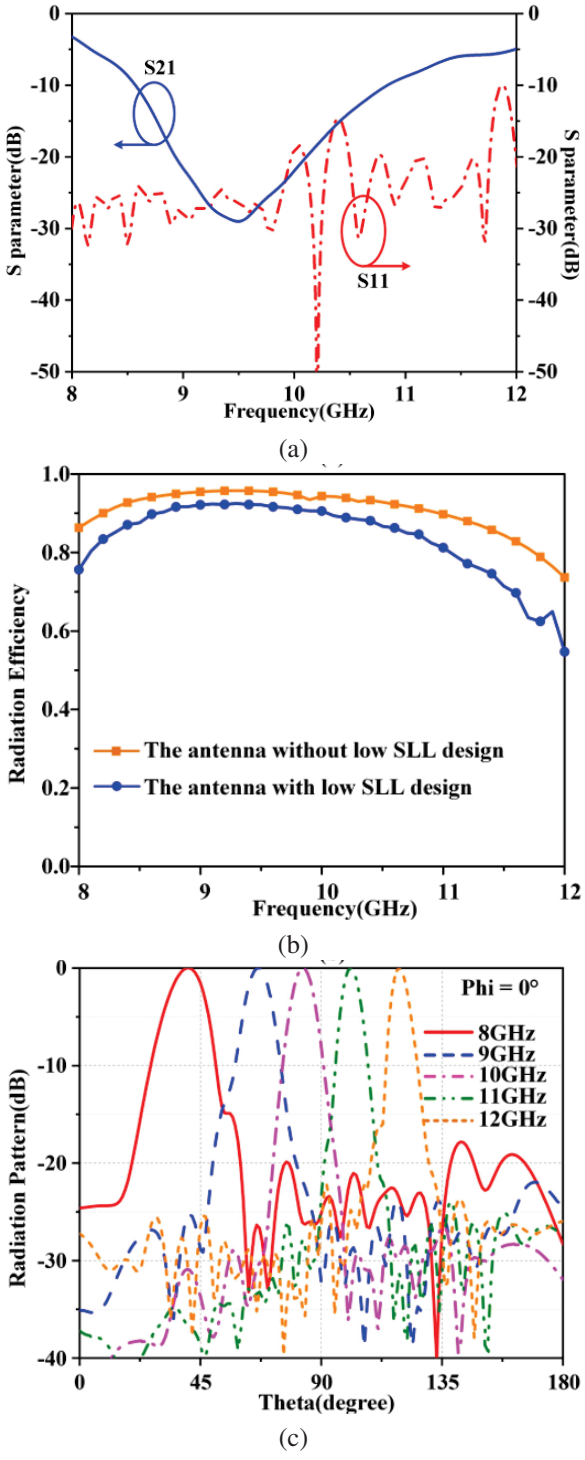

Fig. 10. *Continued.*

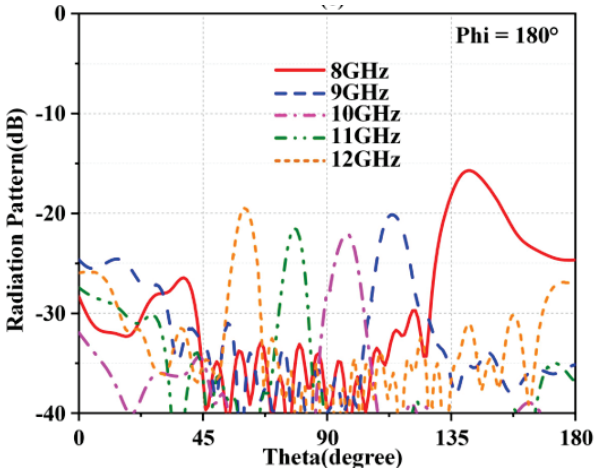

(d)

Fig. 10. (a) Simulated S parameters of the proposed LWA, (b) simulated radiation efficiency of the LWA, (c) simulated radiation patterns of the LWA in phi = 0°, and (d) simulated radiation patterns of the LWA in phi = 180°.

III. MEASURED RESULTS AND DISCUSSION

We manufactured and measured the proposed SSPP-fed circular patch array antenna. The photograph of the SSPP antenna is presented in Fig. 11. The two layers of the antenna are aligned and secured by nylon columns, while the EBG structure and antenna are fastened together with metal sheets and additional nylon columns on the back side of the assembly. The port on the right side of the antenna is connected to a 50 Ω matched load. The simulated and measured reflection and transmission coefficients are shown in Fig. 11. It shows that the measured results agree well with the simulated results. The measured S_{11} is below -10 dB, covering the required operating frequency band of 8 to 12 GHz.

Minor deviations may be mainly caused by SMA soldering and antenna warping. In CST simulation, the SMA soldering is induced by creating slots near the input and output ports and introducing parasitic capacitance (0.4 pF) in these slots. As shown in Fig. 11 (c), the simulated result considering the SMA soldering is closer to the measured result. Since the antenna is large and its ends are a bit warped, a higher air layer is introduced. The antenna warping is simulated by adding a 0.16 mm air layer between the two dielectric substrates in the CST model. As shown in Fig. 11 (d), the resonance frequency of S_{21} considering the antenna warping is shifted to a higher frequency, which agrees better with the measured results.

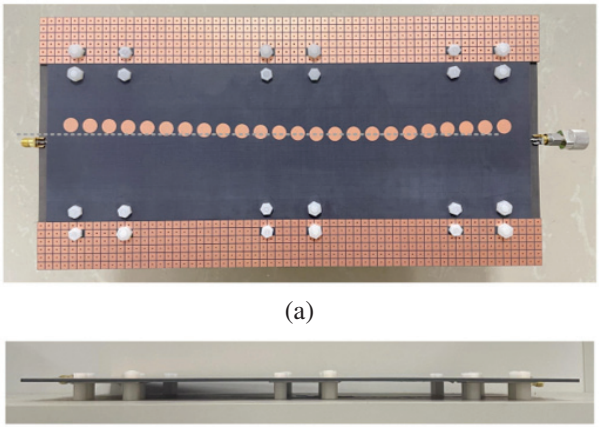

(a)

(b)

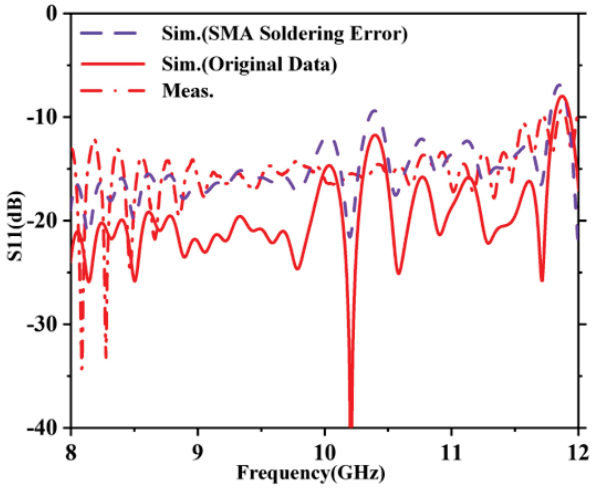

(c)

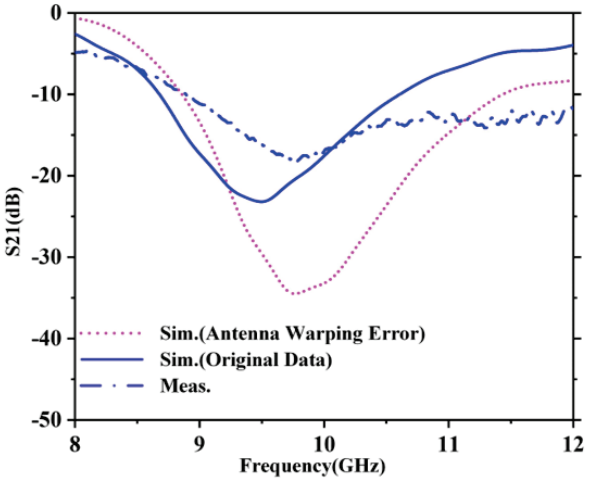

(d)

Fig. 11. Fabricated prototype and the simulated and measured S parameters of the proposed LWA: (a) top view, (b) side view, (c) simulated and measured S_{11}, and (d) simulated and measured S_{21}.

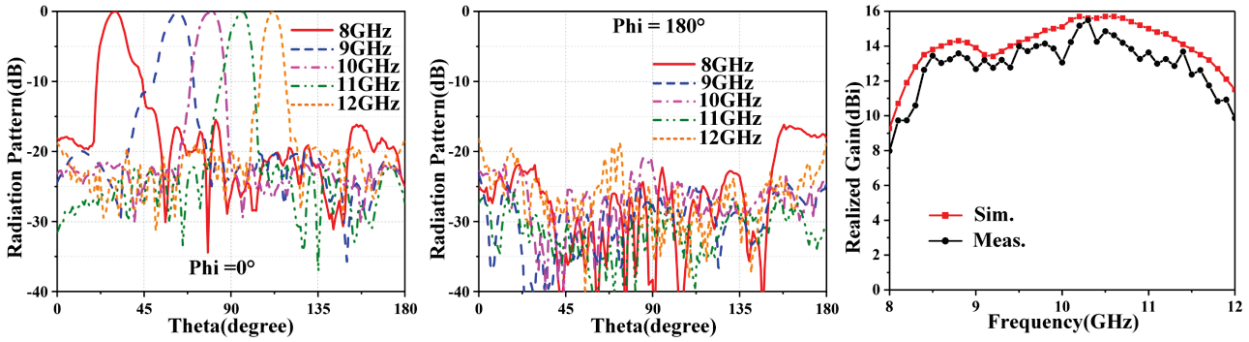

(a) (b) (c)

Fig. 12. (a) Measured radiation patterns of the LWA in phi = 0°, (b) measured radiation patterns of the LWA in phi = 180°, and (c) comparison between the measured and simulated realized gain.

Table 2: Comparison of the proposed SSPP antenna with other referenced prototypes

Ref.	Antenna Type	Bandwidth	Scanning Range	SLL (dB)
[7]	SSPP	8.7∼9.9 GHz (12.9%)	133.7∼153.9° (20.2°)	-7
[8]	SSPP-fed circular patch array	5∼11 GHz (75%)	57∼112° (55°)	-7
[9]	SSPP-fed elliptical patch array	9.8∼12.28 GHz (22.5%)	2∼169° (167°)	-5
[10]	SSPP-fed circular patch array	11∼15 GHz (30.8%)	58∼124° (66°)	-10
[11]	SSPP-fed elliptical patch array	12∼15 GHz (22.2%)	76∼128° (52°)	-20
[13]	Slot array	9.8∼10.2 GHz (0.04%)	118∼122° (4°)	-20
[14]	Slot array	29.1∼29.4 GHz (0.01%)	65.1∼68° (2.9°)	-17
[15]	SIW slot	8.5∼11 GHz (25.6%)	79∼110° (31°)	-20
[17]	SIW slot	33∼37 GHz (11.4%)	44.3∼62.9° (18.6°)	-20
Proposed	SSPP-fed circular patch array	8∼12 GHz (40%)	30∼112° (82°)	-15

The measured radiation pattern of the antenna is shown in Figs. 12 (a) and (b). It indicates that the antenna has a wide scanning range from 30° to 112° (phi = 0°) in the operating band from 8 to 12 GHz, and the maximum SLL in the whole frequency band is lower than -15 dB. The realized gain of the LWA in the beam direction is shown in Fig. 12 (b), which is from 8 to 15.7 dBi. At both ends of the operating band, the lower antenna gain is due to the narrower bandwidth of S_{21}.

Table 2 compares the proposed SSPP-fed circular patch array antenna with other referenced prototypes. In [8–10], the scanning range is efficiently extended using SSPP-fed patch array antennas, but the SLL rises as the scanning angle increases. In [9], despite a scanning range of 167° achieved, the SLL increases to -5 dB. SLL below -15 dB was attained in [13–15, 17], however, the scanning range was constrained and failed to extend beyond 32°. Although it successfully lowers the SLL of the SSPP antenna in [11], the scanning range is only 52°, which is limited for radar applications. In summary, the proposed SSPP-fed circular patch array increases the scanning angle range by adopting a double-layer coupled SSPPs feeding structure to increase the antenna impedance bandwidth, which can cover a wide scanning range from 30° to 112° (phi = 0°) in the X-band and have a maximum SLL below -15 dB, making it suitable for radar detection.

IV. CONCLUSION

This paper proposes a frequency beam scanning antenna with broadband, wide-angle, and low SLL characteristics, adopting an SSPP-fed circular patch array method to achieve broadband and wide-angle scanning range. The tapered attenuation constant distribution is accomplished by changing the coupling strength between the patch elements and the SSPP line, while dielectric surface wave suppression is achieved by adopting EBG structures, resulting in extremely low SLL over the entire frequency band. The experimental results indicate that the antenna has wide-angle scanning ability and low SLL characteristics. In the operating frequency range of 8 to 12 GHz, the scanning angle measured by the antenna is 82° and a maximum SLL less than -15 dB. This antenna has potential application prospects in the field of low-altitude, slow-speed, and miniaturized target detection radar due to its low manufacturing cost, wide-angle scanning range in broadband, and low SLL.

ACKNOWLEDGMENT

This work was supported in part by National Natural Science Foundation of China (61971469), and Fundamental Research Funds of Shaanxi Key Laboratory of Artificially-Structured Functional Materials and Devices (AFMD-KFJJ-21105).

REFERENCES

[1] A. A. Oliner and A. Hessel, "Guided waves on sinusoidally-modulated reactance surfaces," *IRE Trans. Antennas Propag*, vol. 7, no. 5, pp. 201-208, 1959.

[2] J. L. Gomez-Tornero, F. D. Quesada-Pereira, and A. Alvarez-Melcon, "Analysis and design of periodic leaky-wave antennas for the millimeter waveband in hybrid waveguide-planar technology," *IEEE Trans. Antennas Propag*, vol. 53, no. 9, pp. 2834-2842, 2005.

[3] J. B. Pendry, L. Martín-Moreno, and F. J. Garcia-Vidal, "Mimicking surface plasmons with structured surfaces," *Science*, vol. 305, no. 5685, pp. 847-848, 2004.

[4] X. Shen, T. J. Cui, D. Martin-Cano, and F. J. Garcia-Vidal, "Conformal surface plasmons propagating on ultrathin and flexible films," *Proc. Natl. Acad. Sci.*, vol. 110, no. 1, pp. 40-45, 2013.

[5] D. Zhang, X. Liu, Y. Sun, K. Zhang, Q. Wu, Y. Li, and T. Jiang. "Compact transition enabled broadband propagation of spoof surface plasmon polaritons based on the equivalent circuit model," *J. Phys. D: Appl. Phys.*, vol. 55, no. 16, p. 165101, 2022.

[6] D. Zhang, X. Liu, Y. Sun, K. Zhang, Q. Wu, Y. Li, T. Jiang, and S. N. Burokur, "Dispersion engineering of spoof plasmonic metamaterials via interdigital capacitance structures," *Opt. Lett*., vol. 48, pp. 1383-1386, 2023.

[7] G. S. Kong, B. G. Cai, H. F. Ma, and T. J. Cui, "Continuous leaky-wave scanning using periodically modulated spoof plasmonic waveguide," *Sci. Rep.*, vol. 6, no. 29600, pp. 1-9, 2016.

[8] J. Y. Yin, J. Ren, and Q. Zhang, "Frequency-controlled broad-angle beam scanning of patch array fed by spoof surface plasmon polaritons," *IEEE Trans. Antennas Propag.*, vol. 64, no. 12, pp. 5181-5189, 2016.

[9] L. Jidi, X. Cao, J. Gao, T. Li, H. Yang, and S. Li, "Ultrawide-angle and high-scanning-rate leaky wave antenna based on spoof surface plasmon polaritons," *IEEE Trans. Antennas Propag.*, vol. 70, no. 3, pp. 2312-2317, 2022.

[10] D. F. Guan, P. You, Q. Zhang, Z. H. Lu, S. W. Yong, and K. Xiao, "A wide-angle and circularly polarized beam-scanning antenna based on microstrip spoof surface plasmon polariton transmission line," *IEEE Antennas Wirel. Propag. Lett.*, vol. 16, pp. 2538-2541, 2017.

[11] H. W. Yu, Y. C. Jiao, and Z. Weng, "Spoof surface plasmon polariton-fed circularly polarized leaky-wave antenna with suppressed side-lobe levels," *Int. J. RF Microw. Comput. Aided Eng.*, vol. 30, no. 3, pp. 1-9, 2020.

[12] A. Mallahzadeh and S. Mohammad-Ali-Nezhad, "Periodic collinear-slotted leaky wave antenna with open stopband elimination," *IEEE Trans. Antennas Propag.*, vol. 63, no. 12, pp. 5512-5521, 2015.

[13] M. T. Mu and Y. J. Cheng, "Low-sidelobe-level short leaky-wave antenna based on single-layer PCB-based substrate-integrated image guide," *IEEE Antennas Wirel. Propag. Lett.*, vol. 17, no. 8, pp. 1519-1523, 2018.

[14] P. F. Kou and Y. J. Cheng, "Ka-Band low-sidelobe-level slot array leaky-wave antenna based on substrate integrated nonradiative dielectric waveguide," *IEEE Antennas Wirel. Propag. Lett.*, vol. 16, pp. 3075-3078, 2017.

[15] N. Javanbakht, M. S. Majedi, and A. R. Attari, "Thinned array inspired quasi-uniform leaky-wave antenna with low side-lobe level," *IEEE Antennas Wirel. Propag. Lett.*, vol. 16, pp. 2992-2995, 2017.

[16] J. Guo, Z. Li, J. Wang, M. Chen, and Z. Zhang, "Analysis and design of leaky-wave antenna with low SLL based on half-mode SIW structure," *Int. J. Antennas Propag.*, vol. 2015, pp. 1-5, 2015.

[17] Y. J. Cheng, W. Hong, K. Wu, and Y. Fan, "Millimeter-wave substrate integrated waveguide long slot leaky-wave antennas and two-dimensional multibeam applications," *IEEE Trans. Antennas Propag.*, vol. 59, no. 1, pp. 40-47, 2011.

[18] X. Huo, J. Wang, Z. Li, Y. Li, M. Chen, and Z. Zhang, "Periodic leaky-wave antenna with circular polarization and low-SLL properties," *IEEE Antennas Wirel. Propag. Lett.*, vol. 17, no. 7, pp. 1195-1198, 2018.

[19] A. A. Oliner and D. R. Jackson, "Leaky-wave antennas," in *Antenna Engineering Handbook*, 4th ed. J. L. Volakis, Ed. New York, NY: McGraw-Hill, 2007.

[20] F. L. Whetten and C. A. Balanis, "Meandering long slot leaky-wave waveguide-antennas," *IEEE Trans. Antennas Propag.*, vol. 39, no. 11, pp. 1553-1560, 1991.

[21] F. Yang and Y. Rahmat-Samii, "Microstrip antennas integrated with electromagnetic bandgap (EBG) structure: A low, mutual coupling design for array applications," *IEEE Trans. Antennas Propag.*, vol. 51, no. 10, pp. 2936-2946, 2003.

[22] A. H. Panaretos and D. H. Werner, "A note on the isolation performance of nonuniform capacitively

loaded mushroom-type EBG surfaces within a parallel plate waveguide," *IEEE Trans. Antennas Propag.*, vol. 63, no. 11, pp. 5175-5180, 2015.

Yanzhen Shi received the B.S. degree in communication engineering from Shanghai Normal University, Shanghai, China, in 2021. She is currently pursuing the master's degree in communication and information system at Shanghai University. Her research interests include beaming scanning antenna, direction of arrival estimation and radar detection.

Zhibo Fan received the B.S. degree in communication engineering from Shanghai University of Electric Power, Shanghai, China, in 2020. She is currently pursuing the master's degree in communication and information system at Shanghai University. Her research interests include frequency scanning antennas and metamaterials.

Cong Chen received a Ph.D. degree in radio physics from Wuhan University, Wuhan, Hubei, China, in 2009. From 2009 to 2021, he worked in Wuhan Maritime Communication Research Institute, Wuhan, Hubei, China. Currently, he is a Research Fellow with Electronic Information School, Wuhan University, Wuhan, Hubei, China. His research interests include phased array antenna, beaming scanning antenna, and radar scattering.

Yongjin Zhou received the B.S. degree in communication engineering from Shandong University, Jinan, China, in 2006, and Ph.D. degree in electromagnetic field and microwave technology from Southeast University, Nanjing, China, in 2011, respectively. From 2009 to 2010, he was a visiting scholar of University of Houston. From 2011 to 2012, he was a software engineer with EEBU of Marvell Technology (Shanghai) Ltd. From 2012 to 2015, he was an Assistant Professor, and from 2015 to 2020, he was an Associate Professor with School of Communication & Information Engineering, Shanghai University, Shanghai, China. Currently, he is a Professor with School of Communication & Information Engineering, Shanghai University, Shanghai, China. He has authored and coauthored over 90 papers in peer-reviewed journals and conference proceedings. He is IEEE Member, OSA Member, and Senior Member of Chinese Institute of Electronics. He is serving as a Reviewer for over 20 peer-reviewed journals, such as *Nature Electronics, Photonic Research, Optics Letter, Optics Express, Appl. Phys. Express, IEEE Access, IEEE MTT, and IEEE MWCL*. He has served as a Session Chair for several International Symposiums.

His current research interests include microwave and millimeter antenna, plasmonic metamaterials and applications, millimeter wave and THz functional devices and wireless energy transmission.

Channel Measurement and Characterization for 5G Cellular Network with Passive Sounding Method at 2.6 GHz

Hao Sun[1], Lei Li[1], and Wenqiang Tian[2]

China Academy of Information and Communications Technology
Beijing, China
sunhao@caict.ac.cn, lilei1@caict.ac.cn

Department of Standardization, OPPO Research Institute
Beijing, China
tianwenqiang@oppo.com

***Abstract* –** The fifth generation (5G) communication, which is capable of realizing wireless communication with a extremely low latency and high data rate, has been put into commercial use widely. The propagation channel is of great significance for design, performance evaluation, and improvement of 5G system. As to investigate the wireless channel of 5G network, a channel measurement system based on passive sounding method is proposed in this paper. By utilizing the 5G downlink signal, e.g., synchronization signal block (SSB) and channel state information reference signal (CSI-RS), the proposed system is able to extract the multipath parameters of 5G propagation environment. Moreover, a measurement campaign is conducted at an urban macro-cellular (uMa) environment with the passive sounding system. The measured results is briefly analysed and compared with the 3rd generation partnership project (3GPP) results.

***Index Terms* –** 5G cellular network, channel measurement, passive sounding.

I. INTRODUCTION

The fifth generation (5G) communication system has recently become one of the most popular technologies, due to its ability to connect people and share information in a wide range of scenarios with extremely low latency, high data rate and ultra-reliability quality of service (QoS). Compare with the fourth generation (4G) long-term-evolution (LTE) system, 5G is supposed to achieve 1000 times the system capacity, 100 times the data rate, 3-5 times the spectral efficiency, and 10-100 times the energy efficiency [1]. In order to meet the requirements of system performance, many emerging technologies have been adopted to 5G system, e.g., massive multiple-input multiple-output (MIMO), beamforming and millimeter wave, which also brings new challenges for system design and optimization.

As a foundation of any wireless communication system, the research on propagation channels is of great significance for the design, performance evaluation, and improvement of 5G [2], [3]. Channel measurement, also called channel sounding, which is able to acquire the massive first-hand channel data, has been regarded as the crucial method for the propagation environment research. The aim of channel sounding is to obtain the propagation data with the radio equipments, and then characterization the wireless channel environment with post-possessing methods, e.g., search-alternative generalized expectation-maximization (SAGE) algorithm [4]. In recent years, channel measurement and characterization have attracted much attention in both academia and industry, and a great deal of measurement campaigns for 5G scenarios have been widely conducted [5]. In general, there are two main categories of channel measurement framework, i.e., the active sounding and the passive sounding. The active sounding contains two separate sounding devices for signal transmission and reception, respectively. By adjusting frequency band of transmitted signal and scale of antenna array, the 5G propagation characteristic can be effectively studied with the active sounding framework in various scenarios [2]. Although the active sounding has been widely used for many measurement campaigns, it still suffers from many disadvantages, e.g., low mobility of sounders, limited transmission power, restricted radio frequencies, and high system cost.

The passive sounding, which directly regards the base station (BS) as the transmitter and utilizes the communication signal transmitted in the operators' network as the sounding signal, has been proposed to investigate the propagation characteristic for the public in-service wireless communication systems. The advantages of

Submitted On: September 3, 2023
Accepted On: April 5, 2024
https://doi.org/10.13052/2024.ACES.J.391011

passive sounding include that measurement campaigns can be conducted anywhere as long as covered by the cellular network. Moreover, the wireless channel measured with passive sounding is exactly the practical propagation environment of communication systems, which can be directly utilized for performance evaluation and system optimization. Passive sounding has been early adopted in the universal mobile terrestrial system (UMTS) network and LTE network under various scenarios, e.g., high speed train, subway, and urban [6][7][8]. Compared with the UMTS and LTE communication system, 5G provides up to 100 MHz bandwidth for sub-6GHz band and 400 MHz bandwidth for millimeter band, which is favourable for broadband characteristic investigation in passive sounding. Furthermore, benefiting from the wide coverage of 5G commercial cellular network, passive sounding can be regarded as the promising method for 5G channel measurement and modelling. However, the channel measurement and characterization based on passive sounding for 5G network are hardly discussed in the literature [9]. In this paper, we have first developed a channel sounder based on passive sounding framework, which is applicable for channel measurement in 5G networks. Then, the data processing procedures of the proposed system, i.e., 5G downlink signal extraction and multipath parameter estimation, were explained in detail. Moreover, a channel measurement campaign was conducted to investigate the propagation properties of 5G sub-6GHz communication system in a typical urban macro-cellular (uMa) environment. Finally, based on the measured data, the multipath parameters were estimated with the SAGE algorithm, and the propagation characteristics were also discussed and analyzed briefly.

The rest of this paper is organized as follows. Section II describes the passive sounding system and the measurement environment. In Section III, the data processing method, e.g., SAGE algorithm, is discussed. Results and analysis are presented in Section IV. Finally, conclusions are drawn in Section V.

II. PASSIVE SOUNDING SYSTEM

The channel sounder, which aims to record and extract the channel impulse response (CIR) of propagation environments, is the crucial and prerequisite component of channel measurement campaign. The diagram of the proposed 5G passive sounding system is illustrated in Fig. 1, which contains the following components: antenna array, RF switch, RF unit, universal software radio peripheral (USRP), I/Q platform, and 5G user equipment (UE).

The antenna array receives the electromagnetic signal transmitted from 5G base station and transforms it to the RF signal. Due to the high complexity and

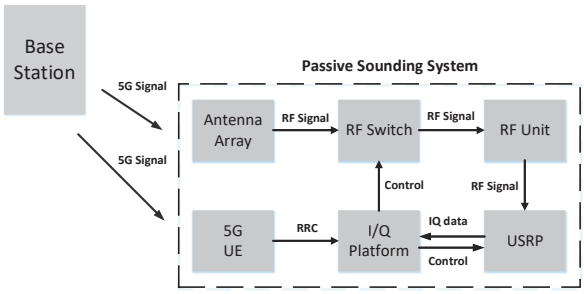

Fig. 1. The diagram of passive sounding system.

cost brought from massive RF channels, we adopt the RF switch to receive the signal alternatively with the time-division multiplexing (TDM) strategy. The switch interval should be no shorter than the 5G signal downlink period, e.g., 20 ms for synchronization signal block (SSB) period, so that each antenna can receive an intact downlink signal. The RF unit, composed of filter and low noise amplifier (LNA), is able to eliminate the interference of out-of-band signals and strengthen the quality of in-band signals. An USRP device is used to convert the RF analogy signal to the I/Q digital signal with frequency conversion and sampling operations. The I/Q platform, namely a high performance workstation, is used to store and process the baseband I/Q signal transmitted from USRP. As to acquire the configuration of 5G cellular network, a 5G UE is used to obtain the radio resource control (RRC) parameters of the serving cell.

Figure 2 illustrates the practical photo of our developed passive sounder. The left-hand side contains antenna array and integrated RF switch, and the right-hand side contains the RF unit, USRP, I/Q platform and 5G UE. In order to receive the multipath impinging from various directions, a cylindrical antenna array with 80 dual-polarized antenna elements is equipped. The radiation pattern of element and beam pattern of array for 2.6

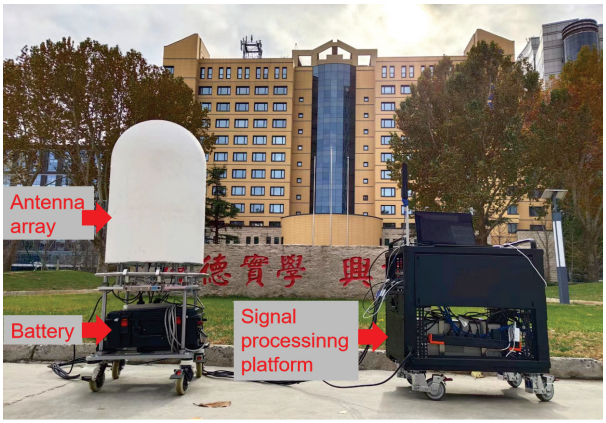

Fig. 2. The photo of passive sounder.

GHz are illustrated in Fig. 3. It is notable that the radiation pattern of antenna array has been calibrated with the over-the-air (OTA) method, e.g., multi-probe anechoic chamber and reverberation chamber [10] [11].

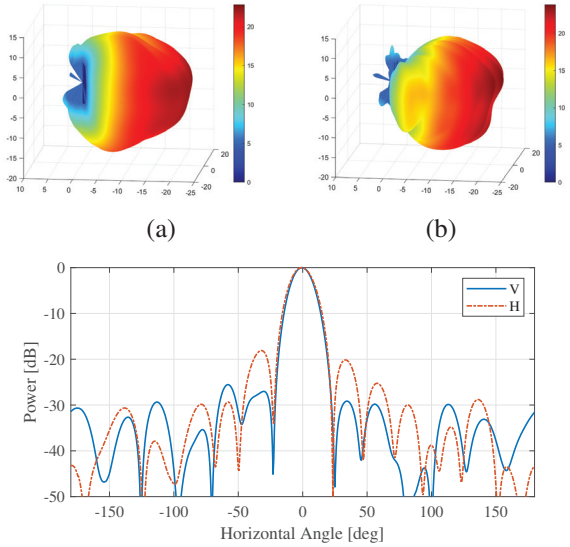

Fig. 3. The radiation pattern of element and beam pattern of array: (a) element pattern of V, (b) element pattern of H, and (c) beam pattern in horizontal range..

III. DATA PROCESSING

A. 5G downlink signal extraction

The key of the passive sounding method is to utilize the 5G downlink signal, which is transmitted from the BS, to analyse the channel environment of 5G commercial cellular network. Thus, how to extract the 5G downlink signal efficiently and accurately is the prerequisite to perform the channel measurement. According to the 3rd generation partnership project (3GPP) physical layer specifications [12], the 5G BS is supposed to transmit several specific signals periodically over the cells, e.g., SSB and channel state information reference signal (CSI-RS).

The SSB signal, composed of the primary synchronization signal (PSS), secondary synchronization signal (SSS) and physical broadcast channel (PBCH), is the significant broadcast signal of 5G network. 5G UE is able to utilize the SSB signal to perform the time-frequency resource synchronization, cell search and master information block (MIB) acquisition. Each SSB consists of four consecutive orthogonal frequency division multiplexing (OFDM) symbols in time domain and twenty consecutive resource blocks (RBs) in frequency domain. The more details of SSB generation and transmission can be found in 3GPP technical specifications [12].

The extraction of SSB can be summarized as a three-step procedure. Firstly, determine the primary cell identify (PCI) and secondary cell identify (SCI) of serving cell by searching the peak of correlation between the received signals and the candidate signals generated by [12], e.g., PSS and SSS. Secondly, determine the SSB pattern and SSB index of the received SSB signal to obtain the location and sequence of demodulated reference signal (DMRS) for PBCH with the correlation-peak searching algorithm. Finally, with the known DMRS of PBCH, we can easily solve the MIB of serving cell by performing the channel estimation and decoding. Figure 4 illustrates the magnitude and phase of channel frequency response (CFR) of the extracted SSB burst, composed of eight TDM distributed SSBs, for 5G current network, respectively. It is indicated that the magnitude and phase of CFR vary over different SSBs, since each SSB is transmitted with different beam weights to cover different serving areas.

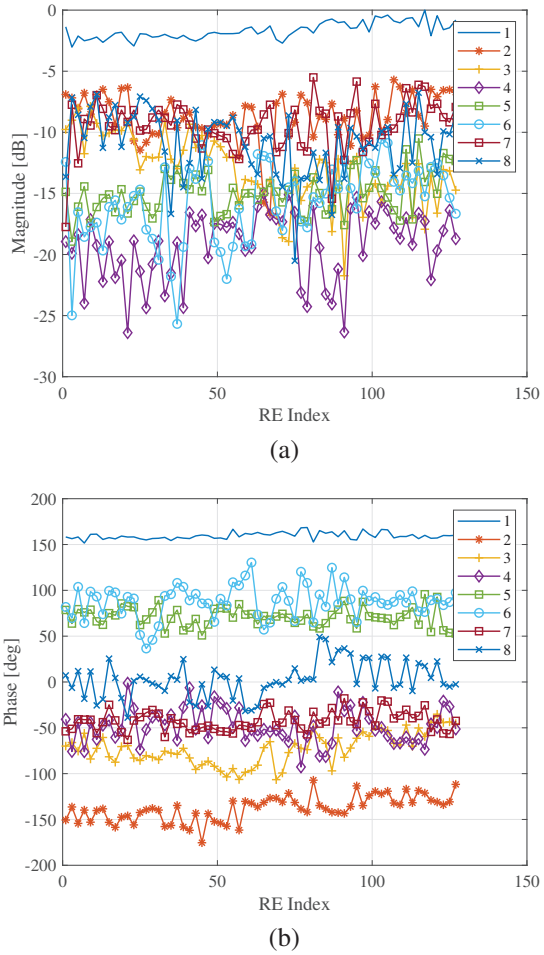

Fig. 4. The (a) magnitude and (b) phase of CFR for different SSBs.

As to acquire the channel state information between BS and UE, 5G serving cell is supposed to transmit channel state information reference signal (CSI-RS) to the connected UE in a periodic or non-periodic manner. The application of CSI-RS can be categorized as these aspects: downlink channel state information acquisition, beam management, fine time-frequency tracking, and mobility management. Different from the SSB, the CSI-RS can be configured as multiple resources and ports in different multiplexing strategies, e.g., code division multiplexing (CDM). The configuration of CSI-RS for the serving cell, such as time-frequency locations and scrambling identity, is determined by the RRC parameters. However, acquiring the real-time RRC parameters of 5G network is technically complicated. Thus, we adopt the 5G commercial UE to establish a RRC connection with the serving cell, and then export the desired RRC parameters into our device. By combining the obtained RRC parameters and MIB, we can readily acquire the CFR of CSI-RS. Figure 5 illustrates the power delay profiler (PDP) comparison between CSI-RS and SSB of the same serving cell with the obtained CFR. It is indicated that the PDP of CSI-RS contains more spikes and burrs compared with that of SSB, since the bandwidth of CSI-RS, i.e., 100 MHz, is much larger than that of SSB, i.e., 7.2 MHz. That is to say, CSI-RS is more suitable for channel measurement, due to its higher resolution of delay domain.

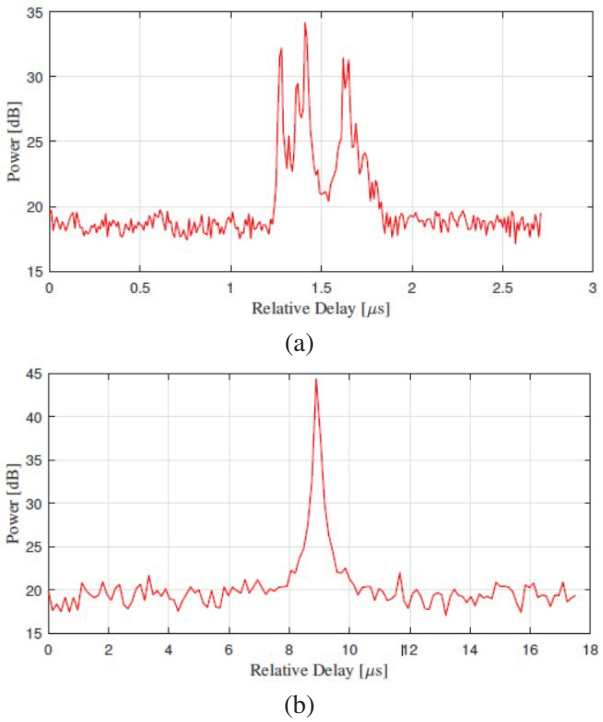

Fig. 5. The PDP comparison between (a) CSI-RS and (b) SSB.

B. Multipath parameter estimation

After obtaining the channel transfer function between the BS and the sounder, it is crucial to analyse the propagation characteristics of channel environment. Many multi-dimensional parameter estimation algorithms have been proposed to solve the multipath component (MPC) parameters, e.g., maximum likelihood (ML) algorithm. The space-alternating generalized expectation-maximization (SAGE) algorithm [4], considered as a good choice for the low calculation complexity and high estimation accuracy, is utilized to extract the parameters of MPC in this paper.

Considering a stationary scenario, where the Doppler frequency is assumed to be 0, the complete observable signal of kth frequency bin can be formulated as:

$$H(k) = \sum_{l=1}^{L} s(k;\theta_l) + N(k), \tag{1}$$

where $N(k)$ denotes the zero-mean complex white Gaussian noise. It is noted that only the MPC parameters of receiver side can be resolved in the passive sounding. Thus, we denote the MPC parameters of lth path as $\theta_l = \left[\tau_l, \Omega_l, \beta_1^l, \beta_2^l\right]$, where each notation denotes delay, arrival angles including azimuth and zenith, and complex coefficients of different polarizations. The contribution of lth path can be formulated as:

$$s(k;\theta_l) = \sum_{p=1}^{2} \beta_p^l \alpha_p(\Omega_l) e^{-j2\pi f_k \tau_l}, \tag{2}$$

where $\alpha_p = [\alpha_p^1, \alpha_p^2, ..., \alpha_p^M]^T$ denotes the radiation pattern of M antennas for different polarization.

By introducing of the expectation-maximization (EM) concept [13], the SAGE algorithm is able to solve the MPC parameters with a low calculation complexity iteratively. The estimation of MPC parameter θ_l' derived by SAGE algorithm can be expressed as:

$$\left(\theta_l'\right)_{ML} = \arg\max_{\theta_l'} \left(f^H D^{-1} f\right), \tag{3}$$

$$\left(\beta_l'\right)_{ML} = \frac{1}{MK}\left(D^{-1} f\right), \tag{4}$$

where:

$$f = \begin{bmatrix} \alpha_1\left(\Omega_l'\right)^H \\ \alpha_2\left(\Omega_l'\right)^H \end{bmatrix} \sum_{k=1}^{K} e^{j2\pi f_k \tau_l'} s(k;\theta_l), \tag{5}$$

$$D = \begin{bmatrix} \alpha_1\left(\Omega_l'\right)^H \alpha_1\left(\Omega_l'\right) & \alpha_1\left(\Omega_l'\right)^H \alpha_2\left(\Omega_l'\right) \\ \alpha_2\left(\Omega_l'\right)^H \alpha_1\left(\Omega_l'\right) & \alpha_2\left(\Omega_l'\right)^H \alpha_2\left(\Omega_l'\right) \end{bmatrix}. \tag{6}$$

Figure 6 illustrates the estimation result with the SAGE algorithm, where the background denotes the estimated power angular spectrum (PAS). The blue dots and arrows denote the estimated paths and its polarization directions. It is noted that the size of blue dot denotes the power of estimated path. Four specular paths have been resolved with the SAGE algorithm, and each of them locates at the peak of estimated PAS. It is indicated that

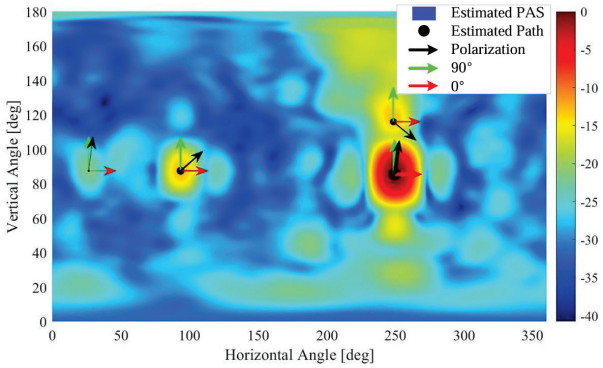

Fig. 6. The illustration of estimated MPC result with SAGE algorithm.

the SAGE algorithm is able to extract the incident paths from different arrival directions efficiently.

IV. RESULTS AND ANALYSIS

A. Measurement environment

The channel measurement campaign is carried out in the office campus of China academy of information and communications technology, located in Beijing, China. Figure 7 illustrates the satellite photo of the measurement environment. As shown in Fig. 7, this office campus is a complicated UMa scenario, surrounded by 5 buildings and 2 parking lots. It is noted that the red lines and letters represent the measurement path. For instance, route *AB* is the road in front of the building 3.

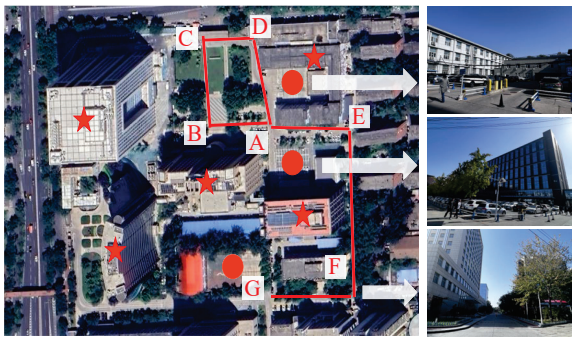

Fig. 7. The satellite photo of measurement environment, where the star denotes the building and the solid dot denotes the parking lot.

The total measurement route is 530 m length, covering the main roads of this office campus. In this measurement, total 53 points are measured with 10 m spacing and 10 channel segments are collected at each point. Finally, a total of 530 channel segments are obtained. Moreover, Table 1 lists the parameters of the measurement campaign. It is noted that the CSI-RS is chosen to analyse the MPC parameters for propagation environment due to its high resolution of delay domain.

Table 1: Measurement parameters

Measurement Length	530m
Measurement Step	10m
Channel Segments	530
Frequency Band	*N*41(2565MHz)
Subcarrier Spacing	30kHz
Bandwidth	100MHz
Signal to Analysis	CSI-RS
CSI-RS Periodicity	20ms

B. Multipath parameters

As to illustrate the multipath extraction process more deeply, two channel sounding results of typical LOS and NLOS scenarios are provided in Fig. 8 and Fig. 9, respectively. As depicted in Fig. 8 (a), the estimated PAS of LOS scenario contains two specular peaks, which contributes to the LOS path and ground reflection path respectively, since these two PAS peaks have similar horizontal angles but symmetrical elevation angles. We can observe that the estimated paths locate in the areas of estimated PAS with high power, implying that

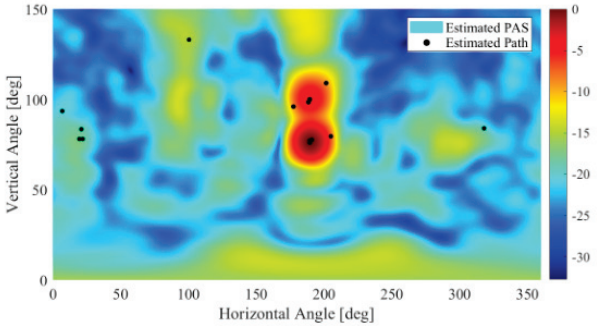

(a)

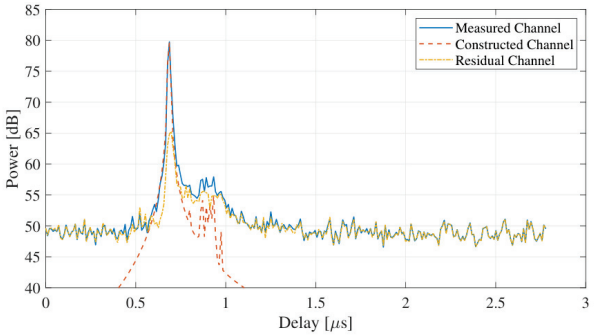

(b)

Fig. 8. The extracted multipath result of LOS scenario: (a) estimated PAS and paths, and (b) channel construction of PDP.

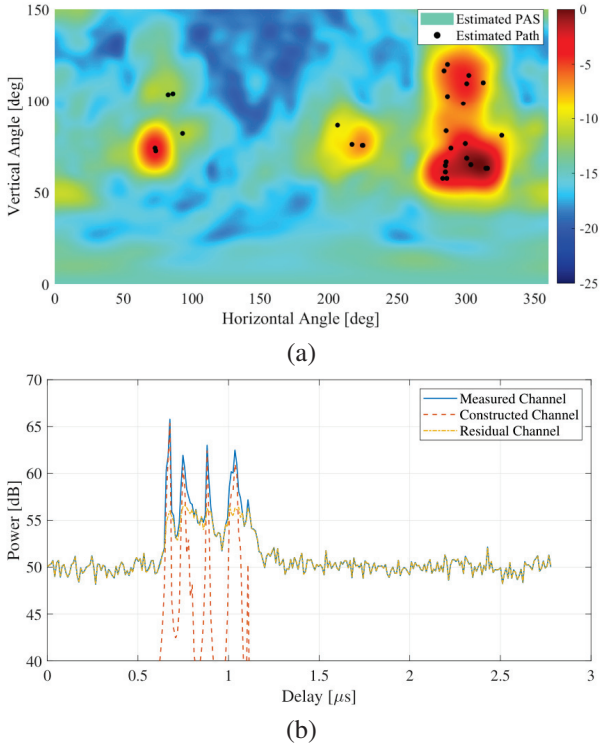

Fig. 9. The extracted multipath result of NLOS scenario: (a) estimated PAS and paths and (b) channel construction of PDP.

the multipath extraction algorithm is quite effective over the spatial domain. Moreover, it is noted that the polarization direction of estimated path is omitted for the sake of simplicity.

Figure 8 (b) indicates the channel construction results in PDP domain, where the constructed channel denotes the CIR generated with the estimated paths and the residual channel denotes the subtraction of measured and constructed channel. We can observe that the PDP shapes of measured and constructed channel are quite similar, indicating that the measured channel is reconstructed well with the estimated multipath. Moreover, the residual channel still exists in Fig. 8 (b), whose PDP peak is 15 dB lower that that of measured channel, probably caused by the dense multipath component (DMC) [14].

Figure 9 provides the extracted multipath result of NLOS scenario. It can be indicated that the channel of NLOS scenario has a more dispersive distribution over spatial and delay domain, since the estimated PAS and PDP spectrums have more peaks than that of LOS scenario. Moreover, the measured channel can still be reconstructed well with the estimated multipath, indicating that we can extract the multipath efficiently both in LOS and NLOS scenarios.

C. Path loss and shadow fading

The path loss (PL) and shadow fading (SF) are of great significance to estimate the link budget and coverage of 5G cellular network. In the passive sounding framework, it is typically assumed that the transmission power of BS is constant. Thus, the receiving power, which is the superposition of transmission power and propagation loss, can be used to reflect the PL and SF of wireless channel. In this paper, as to eliminate the interference of neighbour cell, we adopted the power of constructed power for CSI-RS, illustrated in Fig. 8 (b) and Fig. 9 (b), as the receiving power of serving cell. According to the close-in (CI) free space reference distance model, the PL and SF can be written as:

$$PL(d) = PL(d_0) + 10n\log_{10}\left(\frac{d}{d_0}\right) + X(0,\sigma), \quad (7)$$

where $PL(d_0)$ denotes the PL of reference distance in dB, and n denotes the path loss exponent (PLE). Moreover, X, i.e., shadow fading factor, is a zero-mean Gaussian random variable with a standard deviation σ, representing the large-scale signal fluctuations resulting from shadowing by large obstructions of propagation environments.

Figure 10 illustrates the comparison between our measured model, 3GPP model and free space model. $\Delta P = PL(d) - PL(d_0)$, denoting the power difference between the measured site with distance d and the reference site with distance d_0, is adopted to model the PL and SF of propagation environment, due to the lack of absolute transmission power of BS [9]. In this campaign, we chose measurement data located in the route EF to analysis the PL and SF, composed of a total 60 measurement segments. From the fitted model, we can solve the PLE $n = 2.602$ and the standard deviation $\sigma = 2.671$.

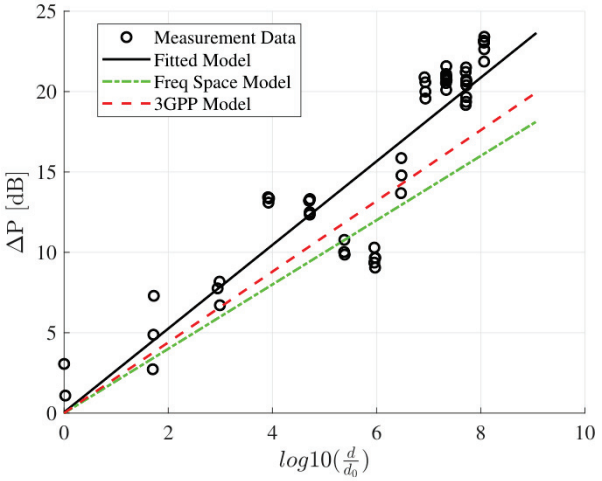

Fig. 10. The comparison between the measured model, 3GPP model and free space model.

Compared with the 3GPP model, i.e., $n = 2.2$, and free space model, i.e., $n = 2$, the obtained PLE is a little larger, since we adopt the planar distance between the BS and measurement location. Moreover, the standard deviation σ is smaller than that of 3GPP model due to the few obstacles existed in the measurement environment.

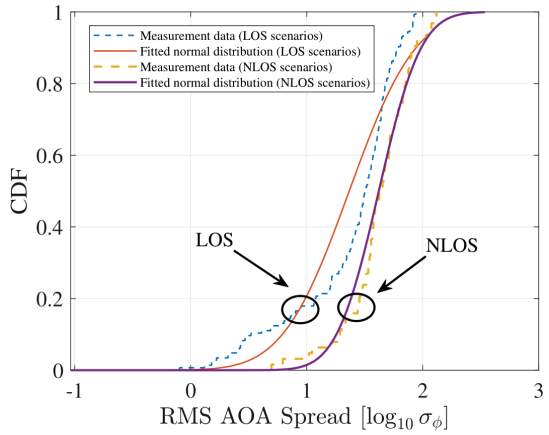

(a)

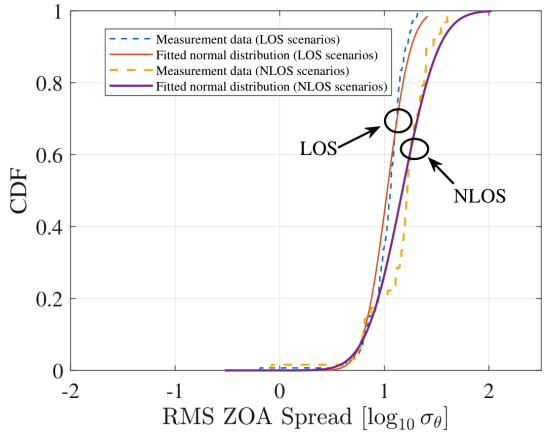

(b)

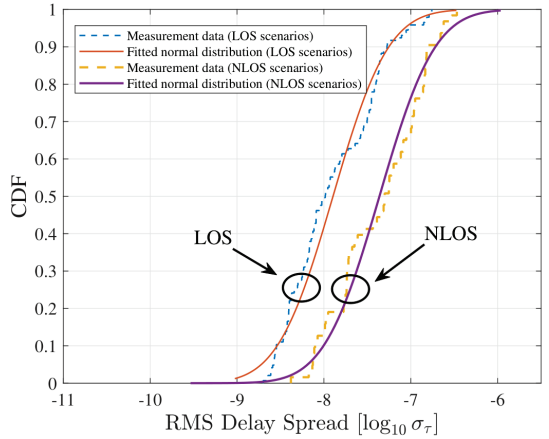

(c)

Fig. 11. The statistical characteristics of MPC parameters: (a) RMS AOA spread, (b) RMS ZOA spread, and (c) RMS delay spread.

D. RMS spreads

The root mean square (RMS) spread of extracted MPC parameters is further discussed with the obtained SAGE results to analyse the statistical characteristics of channel environment for measured scenario. The RMS spread of MPC parameter can be calculated as:

$$x_{rms} = \sqrt{\frac{\sum_{l=1}^{L}(x_l - x_{mean})^2 P_l}{\sum_{l=1}^{L} P_l}}, \tag{8}$$

$$x_{mean} = \frac{\sum_{l=1}^{L} P_l x_l}{\sum_{l=1}^{L} P_l}, \tag{9}$$

where P_l denotes the power of each path [15]. It is noted that x can be be substituted for other MPC parameters, i.e., azimuth of arrival (AOA) angle, zenith of arrival (ZOA) angle, and delay.

As depicted in Fig. 11, the calculated RMS spread of MPC parameters in logarithmic form for LOS and NLOS scenarios can be well fitted with the normal distribution. It can be observed that the RMS spread of NLOS scenario is larger than that of LOS scenario, due to more scatters and reflectors of propagation environment. That also can be illustrated in Fig. 8 and Fig. 9 that the MPC parameters of NLOS scenario have a more dispersive distribution over spatial and delay domains.

Table 2 lists the comparison between the calculated mean value μ and standard deviation δ and those presented in 3GPP 38.901 [16]. It shows that our results are commonly smaller than those of 3GPP, probably due to the effect of beamforming from 5G BS. According to 3GPP specifications, 5G BS is supposed to focus the transmit power on one or several directions, i.e., beamforming, to compensate the propagation path loss. That is to say, the recorded channel is actually the integration of beamforming effect from 5G BS and physical propagation environment, resulting in smaller spreads of spatial and delay domains.

Table 2: The comparison of RMS spread between measurement and 3GPP[16] results

RMS Spread		Measured		3GPP	
		LOS	NLOS	LOS	NLOS
ASA	$\mu(log10(\circ))$	1.366	1.621	1.81	1.96
	$\delta(log10(\circ))$	0.450	0.285	0.20	0.11
ESA	$\mu(log10(\circ))$	1.028	1.173	0.95	1.38
	$\delta(log10(\circ))$	0.179	0.275	0.16	0.16
Delay	$\mu(log10(s))$	-7.90	-7.36	-7.03	-6.44
	$\delta(log10(s))$	0.502	0.502	0.66	0.39

V. CONCLUSION

In this paper, a channel sounding system available for 5G cellular network based on passive sounding

method is proposed to analyse the channel characteristics of realistic commercial network. This system, which regards the 5G BS as the transmitter, is able to receive and decode the 5G downlink signal with the TDM scheme. Based on the decoded 5G downlink signal, e.g., SSB and CSI-RS, the proposed system can extract the MPC parameters between the 5G BS and the sounder with the SAGE algorithm. Moreover, a measurement campaign is carried out at a typical office campus. The measured results indicate that the proposed system is able to capture the channel characteristic of 5G network.

REFERENCES

[1] M. Agiwal, A. Roy, and N. Saxena, "Next generation 5G wireless networks: A comprehensive survey," *IEEE Communications Surveys and Tutorials*, vol. 18, no. 3, pp. 1617-1655, Thirdquarter 2016.

[2] C.-X. Wang, J. Bian, J. Sun, W. Zhang, and M. Zhang, "A survey of 5G channel measurements and models," *IEEE Communications Surveys and Tutorials*, vol. 20, no. 4, pp. 3142-3168, Fourthquarter 2018.

[3] C. U. Bas, R. Wang, S. Sangodoyin, S. Hur, K. Whang, J. Park, J. Zhang, and A. F. Molisch, "28 GHz propagation channel measurements for 5G microcellular environments," *The Applied Computational Electromagnetics Society Journal (ACES)*, vol. 34, no. 02, pp. 363-364, July 2021.

[4] B. Fleury, M. Tschudin, R. Heddergott, D. Dahlhaus, and K. Ingeman Pedersen, "Channel parameter estimation in mobile radio environments using the SAGE algorithm," *IEEE Journal on Selected Areas in Communications*, vol. 17, no. 3, pp. 434-450, Mar. 1999.

[5] J. Huang, Y. Liu, C.-X. Wang, J. Sun, and H. Xiao, "5G millimeter wave channel sounders, measurements, and models: Recent developments and future challenges," *IEEE Communications Magazine*, vol. 57, no. 1, pp. 138-145, Jan. 2019.

[6] X. Cai, X. Yin, X. Cheng, and A. Pérez Yuste, "An empirical random-cluster model for subway channels based on passive measurements in UMTS," *IEEE Transactions on Communications*, vol. 64, no. 8, pp. 3563-3575, Aug. 2016.

[7] T. Zhou, C. Tao, S. Salous, L. Liu, and Z. Tan, "Implementation of an LTE-based channel measurement method for high-speed railway scenarios," *IEEE Transactions on Instrumentation and Measurement*, vol. 65, no. 1, pp. 25-36, Jan. 2016.

[8] X. Cai, J. Rodríguez-Piñeiro, X. Yin, N. Wang, B. Ai, G. F. Pedersen, and A. P. Yuste, "An empirical air-to-ground channel model based on passive measurements in LTE," *IEEE Transactions on Vehicular Technology*, vol. 68, no. 2, pp. 1140-1154, Feb. 2019.

[9] T. Wu, X. Yin, L. Zhang, and J. Ning, "Measurement-based channel characterization for 5G downlink based on passive sounding in sub-6 GHz 5G commercial networks," *IEEE Transactions on Wireless Communications*, vol. 20, no. 5, pp. 3225-3239, 2021.

[10] H. Pei, X. Chen, X. Huang, X. Liu, X. Zhang, and Y. Huang, "Key issues and algorithms of multiple-input-multiple-output over-the-air testing in the multi-probe anechoic chamber setup," *Science China Information Sciences*, vol. 65, no. 131302, Feb. 2022.

[11] J. Yi, C. Dong, W. Xue, and X. Chen, "A switchable metamaterial absorber for fine- tuning of the coherence bandwidth in a reverberation chamber," *IEEE Transactions on Antennas and Propagation*, vol. 70, no. 6, pp. 4908-4913, 2022.

[12] *NR; Physical Channels and Modulation*, vol. 16.3.0, 3rd Generation Partnership Project (3GPP), Technical Speciation (TS) 38.211, Sep. 2020.

[13] M. Feder and E. Weinstein, "Parameter estimation of superimposed signals using the EM algorithm," *IEEE Transactions on Acoustics, Speech, and Signal Processing*, vol. 36, no. 4, pp. 477-489, Apr. 1988.

[14] S. Jiang, W. Wang, Y. Miao, W. Fan, and A. F. Molisch, "A survey of dense multipath and Its impact on wireless systems," *IEEE Open Journal of Antennas and Propagation*, vol. 3, pp. 435-460, 2022.

[15] J. Zhang, D. Dong, Y. Liang, X. Nie, X. Gao, Y. Zhang, C. Huang, and G. Liu, "Propagation characteristics of wideband MIMO channel in urban micro- and macrocells," pp. 1-6, 2008.

[16] *Study on channel model for frequencies from 0.5 to 100 GHz*, vol. 14.2.0, 3rd Generation Partnership Project (3GPP), Technical Report (TR) 38.901, Sep. 2017.

Hao Sun received the master's degree from the Beijing University of Posts and Telecommunications, Beijing, China, in 2021.

He is currently an engineer with the China Academy of Information and Communications Technology, Beijing. His current research interests include over-the-air testing, channel measurement and channel modeling.

Lei Li received the master's degree from the Beijing University of Posts and Telecommunications, Beijing, China, in 2016.

He is currently a senior engineer with the China Academy of Information and Communications Technology, Beijing. His current research interests include over-the-air testing for 5G devices and C-V2X, channel measurement and channel modeling.

Wenqiang Tian received his Ph.D. degree from University of Chinese Academy of Sciences in 2015.

Now, he is a senior Standardization Engineer of Guangdong OPPO Mobile Telecommunications Corp., Ltd. He has participated in the 5G standardization work and focused on physical layer design in 3GPP R15 and R16. Since 2018, he has started the research of B5G/6G and led the study on AI empowered PHY.